Acoustic Forces in Cytometry and Biomedical Applications: Multidimensional Acoustophoresis

Grenvall, Carl

2014

Acoustic Forces in Cytometry and Biomedical Applications

Multidimensional Acoustophoresis

Carl Grenvall

LUND
UNIVERSITY

DOCTORAL DISSERTATION

Cover Illustration
Two-dimensional positioning of red blood cells and subsequent analysis on an integrated chip Coulter counter (Paper IV).

Public Defense
December 5th 2014 at 10:15 in lecture hall E:1406, Ole Römers väg 3, Lund, Sweden.

Faculty Opponent
Dr, Assoc. Prof. Steven Graves
University of New Mexico, Center for Biomedical Engineering, Albuquerque, N.M., USA

Board of Examination
Professor Peter Rådström
Lund University, Div. of Applied Microbiology, Lund, Sweden

Dr, Assoc. Prof. Aldo Jesorka
Chalmers University of Technology, Biophysical Technology Lab., Gothenburg, Sweden

Dr Jason Beech
Lund University, Div. of Solid State Physics, Lund, Sweden

Deputy member: Dr Sarah Fredriksson
CEO/founder at Genovis AB, Lund, Sweden

Advisors
Professor Thomas Laurell and Dr Johan Nilsson
Lund University, Dept. Biomedical Engineering, Lund, Sweden

Lund University, Dept. Biomedical Engineering, Lund, Sweden
ISBN Printed format: 978-91-7623-194-4
ISBN PDF-format: 978-91-7623-195-1
ISRN: LUTEDX/TEEM – 1096 – SE
Report: 3/14

Printed in Sweden by PH & Johan - Masters of Printing, E-House, Lund University

Lund 2014

List of publications

Paper I: Harmonic microchip acoustophoresis: a route to online raw milk sample precondition in protein and lipid content quality control

Grenvall, C., Augustsson, P., Folkenberg, J. R. & Laurell, T.

Anal. Chem. 81**,** 6195–6200 (2009)

Paper II: Label-free somatic cell cytometry in raw milk using acoustophoresis

Grenvall, C., Folkenberg, J. R., Augustsson, P. & Laurell, T.

Cytom. Part A J. Int. Soc. Anal. Cytol. 81, 1076–83 (2012)

Paper III: Acoustic actuated fluorescence activated sorting of microparticles

Jakobsson, O., Grenvall, C., Nordin, M., Evander, M. & Laurell, T.

Lab Chip 14, 1943–50 (2014)

Paper IV: Two-dimensional acoustic particle focusing enables sheathless chip Coulter counter with planar electrode configuration

Grenvall, C., Antfolk, C., Zoffmann Bisgaard, C. & Laurell, T.

Accepted advance article, *Lab Chip* (2014). doi:10.1039/C4LC00982G

Paper V: Concurrent isolation of lymphocytes and granulocytes using improved free flow acoustophoresis with cell prefocusing and multiple target outlets

Grenvall, C., Magnusson, C., Lilja, H. & Laurell, T.

Manuscript under language review. Expected submission in November 2014.

Author's contribution to the publications

Paper I: Harmonic microchip acoustophoresis: a route to online raw milk sample precondition in protein and lipid content quality control

Major contribution to modelling, chip manufacturing, experimental design, experimental work, data collection, results analysis and writing.

Paper II: Label-free somatic cell cytometry in raw milk using acoustophoresis

Major contribution to modelling, chip manufacturing, experimental design, experimental work, data collection, results analysis and writing.

Paper III: Acoustic actuated fluorescence activated sorting of microparticles

Major contribution to modelling and proof-of-concept work. Minor contribution to experiments and writing.

Paper IV: Two-dimensional acoustic particle focusing enables sheathless chip Coulter counter with planar electrode configuration

Major contribution to acoustic modelling, chip design, device engineering, experimental design, experimental work, data collection, results analysis and writing. Minor contribution to impedance data analysis and modelling.

Paper V: Concurrent isolation of lymphocytes and granulocytes using improved free flow acoustophoresis with cell prefocusing and multiple target outlets

Major contribution to modelling, chip design, chip manufacturing, experimental design, experimental work, results analysis and writing. Minor contribution to FACS-data collection and analysis.

Who needs fiction when there is magic in the real world; you just need a microscope to see it

Spoiler: The answer is 42

List of abbreviations

AC: Alternating Current

ACF: Acoustic Contrast Factor

BAW: Bulk Acoustic Wave

CFD: Computational Fluid Dynamics

DC: Direct Current

DEP: Dielectrophoresis

DLD: Deterministic Lateral Displacement

DRIE: Deep Reactive Ion Etching, used to form structures in e.g., glass and silicon

FACS: Fluorescence Activated Cell Sorting

FFA: Free Flow Acoustohoresis

FITC: Fluorescein isothiocyanate, fluorochrome used for particle labelling

IC: Integrated Circuit

KOH: Potassium hydroxide, chemical used to etch microchannels in silicon

LOC: Lab on a Chip

MEMS: Micro Electro Mechanical System

NS: Navier-Stokes equations, describes viscous fluid dynamics

PDMS: Poly(dimethylsiloxane), polymer material often used to create microfluidic channels

PFF: Pinched Flow Fractionation

PIV: Particle Image Velocimetry

POC: Point of Care

PRF: Primary Acoustic Radiation Force

(S)SAW: (Standing) Surface Acoustic Wave

SRF: Secondary Acoustic Radiation Force

μ-TAS: Micro Total Analysis System

Preface

It's not easy to grow up being told that you can do whatever you want (even though I know you meant well mom) if you don't know what is out there, what you want or what doing all those things will lead to. In my case it led here. After living (studying, working, researching, partying, playing, loving, laughing, crying and above all having fun) in Lund for 16 years it is now time to present some of my tangible findings on the subjects of life, the universe and everything in this dissertation.

It would be impossible to be where and who I am today without the following persons:
Professor Thomas Laurell, my supervisor, scientific mentor and partner in crime when it comes to late night writing sessions, always delivering in the end and at the end. His influence and contribution to this dissertation cannot be overstated. Associate professor Johan Nilsson, my co-supervisor and the nicest head of department one could wish for. Never too demanding, yet still in control. Mickael Holmquist, who managed to finally get me on the right track during studies, which in the end led us to writing our Master's thesis together concerning some strange acoustic forces in small channels. Everyone at the department of Biomedical Engineering. Per, for teaching me the ropes and living with me during conferences, without complaining about our crazy adventures. Andreas, Simon, Björn and Ola for being great fun to work with and beating me in quizzes, epic WoT ranting, C(K)ass beer drinking and lab-chaos respectively. Maria A for sharing my sense of humor and meeting Christian who always made me enjoy the late night parties, even when Josefin ran out of wine. Micke for being a fun and helpful guy with monkey tendencies. Klara for happy conference hangouts. Pelle for always being thorough, something I needed to learn. Hong, Kevin and Kishore for international discussions and happiness. Jeewoong and Sujin for always being friendly and making me smile. Cecilia for saving me from 12h straight computer sessions. Fredrik for the best nerdy-computer guidance. Belinda for being so positive. Axel for being a better master student than I deserved. Martin for his all-round knowledge. Walle for great help during clean-room work. Filip for tutoring and jokes in the early days. Eva, Anke, Asilah and Kerstin for making work more pleasant. Magnus C and Tomas J for nice floorball games and diving/train-discussions. Hans and Monica for my ultrasound education. Ákos for nice talks during my BMC days. Maria T, Anna and Anette for bringing some much needed girl-power. Désirée, Malgorzata, Ulrika, Eva, Elly and Tord for taking care of paperwork, not my strongest ability. PH & Johan for being awesome. The KTH acoustics group for enjoyable conferences. Professor Hideaki Matsuoka for accommodating me during my research in Tokyo. FOSS (Jacob, Christer, Steen, Nils-Gunnar) for a good collaboration.

All friends, thanks for being part of my life <3

My family who helped along the way - Mom, Magnus, Karin and Dad, you're in my heart.

Katarina you are the love of my life and without your kindness, support, understanding and helpful words during our time together, I would and could not be me. Thanks for journeying through life with me and soon taking the next step with me away from Lund and into the vast macroscale world.

Contents

Introduction

This dissertation explores the possibilities that emerge when we enter the microscale kingdom of cells. Specifically, it presents novel ways in which acoustic forces can be used to further improve cytometers and biomedical methods and instruments. Mankind has always been fascinated by extremes, especially the physical extremes of the very big or very small. However, it was not until the 17th century that the recently invented microscope allowed us to examine the smallest dimensions of life, including the 1665 discovery of dead cells in plant tissue by Robert Hooke[1], and the 1676 discovery of living cells (bacteria from a human mouth) by Antonie van Leeuwenhoek[2] (Fig. 1). Thus the field of microbiology was born, and scientists have relentlessly tried to further understand and manipulate these tiny living organisms ever since.

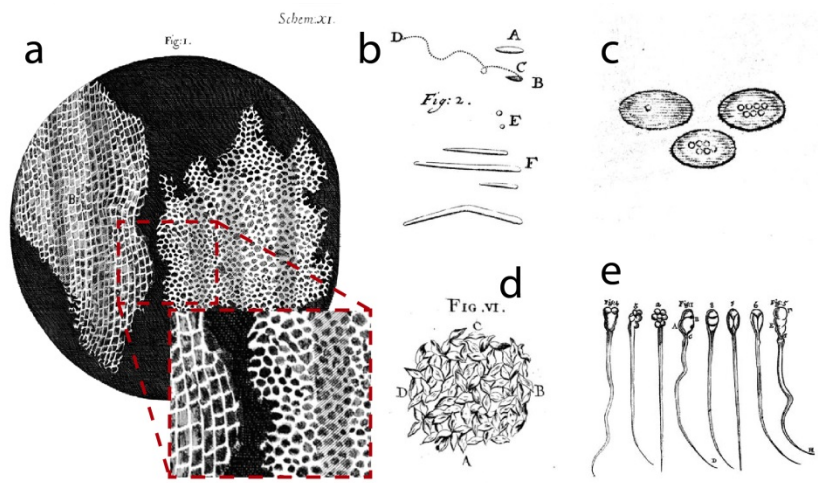

Figure 1, Mankind's first ventures into the microscale world of cells. Robert Hooke drew the first illustrations of cells and their irregular geometry in his 1665 book Micrographia, after observing dead cork tree cells through one of the first microscopes (a). The first investigations of live cells were carried out by Antonie van Leeuwenhoek in 1676 when he used his improved microscope to discover motile cells in the form of mouth bacteria, later described in letters to the Royal Society (b). Leeuwenhoek then carried on to illustrate various other types of cells including red blood cells from fish with stained nuclei (c), epithelial cells from his foot callus (d) and rabbit (four leftmost) and dog (four rightmost) spermatozoa (e).

In 1959 Robert Feynman held his "There's plenty of room at the bottom"-lecture[3] which included the following passage, that probably summarizes the thoughts of many researchers ever since the days of Hooke and van Leeuwenhoek:

"A biological system can be exceedingly small. Many of the cells are very tiny, but they are very active; they manufacture various substances; they walk around; they wiggle; and they do all kinds of marvellous things – all on a very small scale. Also, they store information. Consider the possibility that we too can make a thing very small which does what we want – that we can manufacture an object that manoeuvres at that level!"

Dr Feynman did not have to wait long for this possibility to come true. Driven by the development of the integrated circuit and micro electro mechanical systems (MEMS) the microfabrication techniques in the 1970s reached a stage where they allowed the creation of microfluidic applications and micromachined chemical analysis systems on silicon substrates[4,5] (Fig. 2a). The first examples of integrated microfluidic systems for use in biomedical applications were presented in the early 1990s when Manz et al. introduced the Micro Total Analysis System (μ-TAS) for use in capillary electrophoresis[6–8] (Fig 2b). During the 1990s and early 2000s the fluidic control was improved and new materials, including poly(dimethylsiloxane) (PDMS)[9], were introduced as the concept of μ-TAS went from being seen as a means to make better use of the lacklustre chemical sensors of the time, to provide a Lab-on-a-Chip (LOC) platform in which samples could be pretreated, separated and analysed in a miniaturized system that required less sample, reagent and carrier-medium (Fig 2c)[10–14].

The benefits of microscale analysis systems include well defined laminar flows where small sample volumes or reagents can be precisely controlled spatially with rapid cooling or heating of samples, allowing temporal control of chemical reactions depending on the application[15,16]. It is also possible to integrate the systems into larger platforms where different unit-operations are carried out in sequence. The small size also allows multiple assays to be carried out simultaneously[17–20].

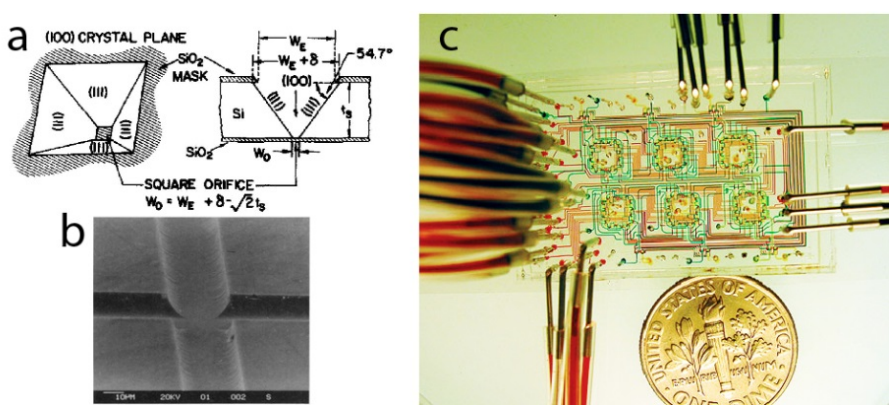

Figure 2, Development of the Lab-on-a-Chip. An inkjet nozzle etched from a silicon wafer was one of the first examples of microfabricated microfluidic applications (a). In the early 1990s Manz et al. presented an etched glass chip channel to be used for capillary electrophoresis and laid the foundation for Micro Total Analysis Systems (μ-TAS) (b). Developments over the next decade, including improved fluidic network stability and more precise microfabrication processes, combined with the introduction of new materials like PDMS, allowed the creation of Lab-on-a-Chip devices with higher complexity and added functionality compared to earlier systems (c). *Reprinted with permission: Bassous[4](a), Harisson[8](b) and Balagaddé[14](c).*

Although the early μ-TAS and LOC systems were able to handle and analyse liquid samples in small volumes they still had one important shortcoming, namely the inability to introduce and manipulate cells and other particles in the microfluidic system, which Dr Feynman mentioned in his lecture series.

A number of passive and active methods for particle manipulation on the microscale were thus introduced in order to further expand the range of unit operations and applications. These include: active (external force) and passive (hydrodynamic) flow positioning and immobilization; separation methods based on size, density, electric charge and magnetic or optic properties; buffer media switching and contact-less trapping and enrichment (Fig. 3)[21–29]. The particle manipulation techniques made it possible to circumvent the drawback of having to rely solely on diffusion to mix labelling reagents with cells or particles[30].

In this dissertation some of the most frequently used passive and active microscale methods for particle manipulation are compared and their benefits and drawbacks are discussed. These include hydrodynamic manipulation with sheath flow lamination[31], inertial forces[32] and dean flows[33] as well as clever use of channel geometries to achieve hydrodynamic size manipulation through pinched flow fractionation (PFF)[34], deterministic lateral displacement (DLD)[35] and hydrophoresis[36]. The active force methods include dielectrophoresis (DEP)[37], magnetophoresis[38], optical tweezers[39] and acoustophoresis[40]. These microscale methods are also compared to commercial macroscale methods for particle and cell handling including centrifugation, density fractionation and large volume sheath flow lamination.

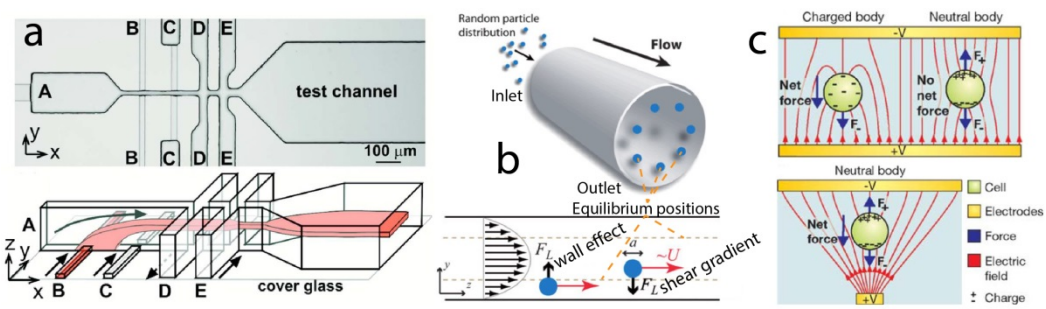

Figure 3, Passive and active particle manipulation techniques. Sheath flow lamination using multiple flows has frequently been used to position a suspension with particles, often in spatially sensitive applications like Coulter counters or flow cytometers (a). Opposite inertial forces can be used to position particles in equilibrium positions in a microfluidic channel (b). Electric fields can also be used to move charged (electrophoresis) as well as neutral (DEP) particles (c). *Adapted with permission: Simonnet[41](a),Di Carlo[23](b) and Voldman[42](c).*

While all of the active force methods offer the ability to manipulate particles in a sheathless system, most of them suffer from drawbacks that include restrictions on which flow media that can be used (DEP), a need to label/pretreat samples (magnetophoresis) and force limitations intrinsic to the method or due to heating issues (DEP and optical tweezers). In relation, the acoustic force method (acoustophoresis) can be used with a wide range of flow media, offers label free manipulation and allows relatively large sample throughput in various chip materials. Compared to most of the other manipulation methods that are

heavily dependent on particle size, acoustophoresis also offers separation and positioning based on particle density and compressibility[40,43–49]. Other acoustophoretic unit operations include trapping[50–55], particle switching[56,57], acoustic medium flipping[58], buffer exchange[59–62], parallelization of sample streams[46,63,64], fluorescence activated sorting[56] and sample mixing[65]. Some of these unit operations e.g., density based binary separation, are unique to the acoustophoretic method (Fig. 4). The method is also able to perform sorting according to particle surface chemistry by treating samples in a similar way to magnetophoresis but does not run the risk of clogging due to formation of magnetic bead-cell complexes.

With the benefits of acoustophoresis it seems natural to apply acoustic forces to improve microscale systems used to handle or analyse cells and other particles. This dissertation presents some of the recent developments where acoustophoresis is used in the field of cytometry and biomedical applications, specifically by utilizing multiple acoustic wavelength geometries or two-dimensional particle manipulation. Paper I presents a novel way to pretreat a raw milk sample in order to facilitate rapid quality control[48]. Paper II extends this method by presenting a way to allow label free cytometry in raw milk[66]. Paper III showcases the ability to sort particles with fluorescence activated acoustic forces[56]. Paper IV presents a low complexity high precision proof-of-concept sheathless impedance cytometer that performs red blood cell (RBC) sizing and may be integrated in other chip based systems[67]. Paper V presents an improved method for concurrent blood component fractionation that requires less manual handling compared to established methods[68].

The theory section explains the underlying physical laws that govern the microscale fluid systems presented here. Acoustic force theory is explained in detail for better understanding of the acoustic radiation forces that act on the suspended particles and also cause media streaming. The particle manipulation section compares the different methods that are available to researchers in the biomedical microfluidic field. The microfabrication section deals with the design aspects of using various materials. Unit operations and applications specific for acoustophoresis are presented. Biofluids and cell types including blood and raw milk are discussed to underline the challenges that researchers are faced with during system design, handling and analysis. The aim of this dissertation is to provide a foundation for future development of acoustic force applications in cytometry and biomedicine.

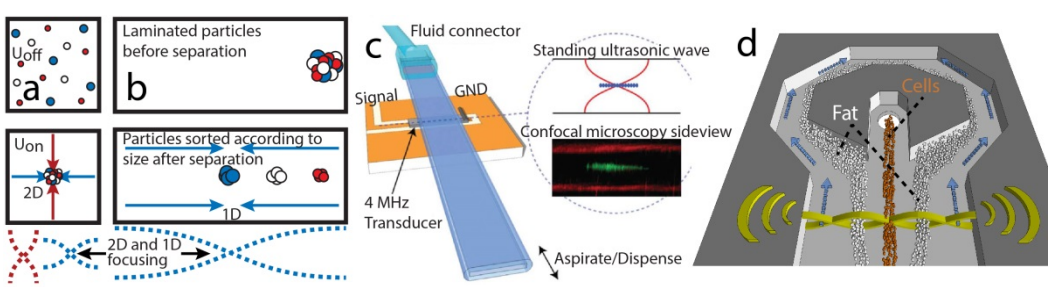

Figure 4, Acoustic force manipulation of particles. Simultaneous acoustic actuation in two dimensions facilitates very well defined particle positions (a). Free flow acoustophoresis can separate particles according to size, density or compressibility (b). Acoustic trapping allows buffer changes, culturing and continuous cell analysis to be carried out (c). Multinode systems can perform binary separation of e.g., fat and cells in raw milk or RBCs and adipose tissue cells in post-surgery shed blood (d). *Adapted with permission: Hammarström[69](c).*

Theory

Microfluidics

This section explains the experimental and theoretical breakthroughs that lay the foundation for our current understanding of fluid dynamics. These theories and models are of vital importance to the design of the acoustofluidic systems described in this dissertation.

History

When introducing the research field of fluidic systems it is important to mention and appreciate the pivotal works presented by the giants of the fields of fluid mechanics in general and Newtonian fluids in particular. Archimedes described the behaviour of objects in fluids in the 3rd century B.C., establishing the field of hydrostatics, i.e. dealing with fluids at rest. Leonardo Da Vinci then predated the later giants of the field by sketching and commenting on turbulent flows at around 1500 A.D., 400 years before Reynolds presented his turbulence decomposition (Fig. 5).

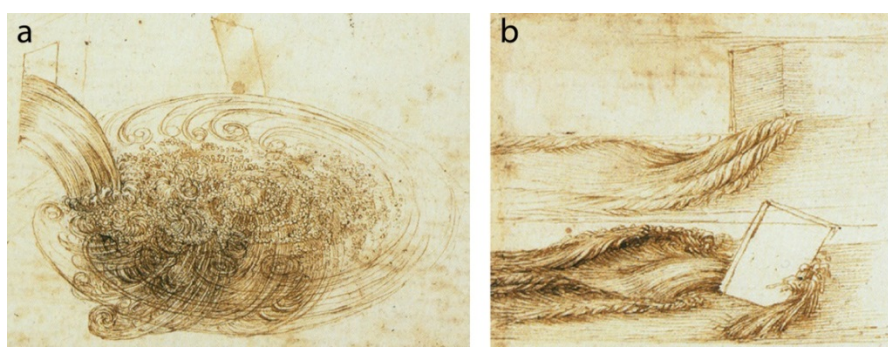

Figure 5, Sketches by Leonardo Da Vinci depicting turbulent flow. In a comment on the aspects of the turbulent flow Da Vinci wrote: "Observe the motion of the surface of the water, which resembles that of hair, which has two motions, of which one is caused by the weight of the hair, the other by the direction of the curls; thus the water has eddying motions, one part of which is due to the principal current, the other to the random and reverse motion."; predating later theory on fluid parcels and multiscalar flow by 400 years (a). On the same page of his sketchbook Da Vinci also illustrated the turbulent flows caused by static objects (b).

Thus Da Vinci made one of the first recorded comments on the field of fluid dynamics. Newton later laid the groundwork for fluid dynamics in Principia (1687) where the

following lines explain the phenomenon of viscosity: "*Resistentian, quae oritur ex defectu lubricitatis partuim fluidi, caeteris paribus, proportionalem esse velocitati, qua partes fluidi separantur ab invicem*", roughly translated as "The resistance that arises from want of slipperiness of the parts of the fluid is, with other things held constant, proportional to the velocity with which the parts of the fluid are separated from one another.". Newton thus established the relationship between flow and shear in a Newtonian fluid, relying on his 2nd law regarding conservation of energy, which was further explained mathematically by Bernoulli in Hydrodynamica (1738), regarding ideal or "inviscid" fluids. Newton's law was valid for a one-dimensional field and remained that way until the 19th century, when it was reformulated to be valid for multidimensional flows, governed by the Navier-Stokes equations which are the foundation upon which the modelling and designs in this dissertation are based.

Navier-Stokes equations

The Navier-Stokes equations (NS) describe the viscous flow of a fluid. They originate in Newton's 2nd law of conservation of energy and describe how flow is a result of interactions between inertia and stress. By utilizing NS, researchers may investigate and model how a fluid behaves in a certain geometric volume under a given pressure. This is very useful when designing functional microfluidic channels. Theoretical solutions to the equations exist, but for practical use they are most often solved by approximation e.g., by using finite elements, in a computational fluid dynamics (CFD) software like COMSOL™. For the applications described here the general NS can be simplified to explain incompressible flow of Newtonian fluids, as compared to the general equation which is valid for all viscous flows. The simplified NS can be found below, written in a form that paraphrases Newton's original law by separating inertial and force related terms (Eq. 1). Inertial terms are coupled to density, unsteady acceleration and convective acceleration and constitute the left hand side of the equation. The force terms include pressure, viscosity and other body forces like gravity and are on the right hand side. The convective acceleration term, $v \cdot \nabla v$, is the only nonlinear term in the simplified NS and can be described as the changes in flow that are caused by channel geometry e.g., a channel that narrows into an aperture used for Coulter counting which increase the flow speed in that section. The systems presented in papers I-V are all designed to have non-turbulent constant flow, by which follows that the unsteady acceleration term, flow change over time, will be zero.

$$\rho\left[\frac{\partial \boldsymbol{v}}{\partial t} + \boldsymbol{v}\cdot\nabla\boldsymbol{v}\right] = -\nabla p + \eta\nabla^2\boldsymbol{v} + \boldsymbol{f} \qquad \textbf{\textit{Eq. 1 The Navier} - \textit{Stokes equations}} \ (\textbf{\textit{incompr. flow}})$$

$\boldsymbol{\rho = density\ of\ the\ fluid}$

$\boldsymbol{v = velocity\ vector\ field, descibing\ the\ fluid\ velocity\ in\ each\ point}$

$\boldsymbol{\eta = dynamic\ viscosity\ of\ the\ fluid}$

$\boldsymbol{p = pressure\ in\ the\ fluid}$

$$\boldsymbol{f = other\ body\ forces, i.e.\ gravitational, electrical, acoustic\ etc.}$$

Laminar flow

If the inertial forces are miniscule compared to the viscous forces in the fluid, a phenomenon called laminar flow may occur. In such a flow system there will be no turbulence and each fluid layer will flow parallel to the next. This allows for precise alignment of sheath flows in a laminar system with multiple inlets and outlets. As a result of this, the time dependant positions of suspended particles in the system will be well defined if external forces (gravitational, acoustic, electrical etc.) are disregarded. Laminar flow is easily produced in microfluidic systems but it is also possible to observe the same parallel streamlines more intuitively by looking at glaciers which demonstrate laminar properties because of the slow flow and high viscosity of glacial ice[70,71] (Fig. 6).

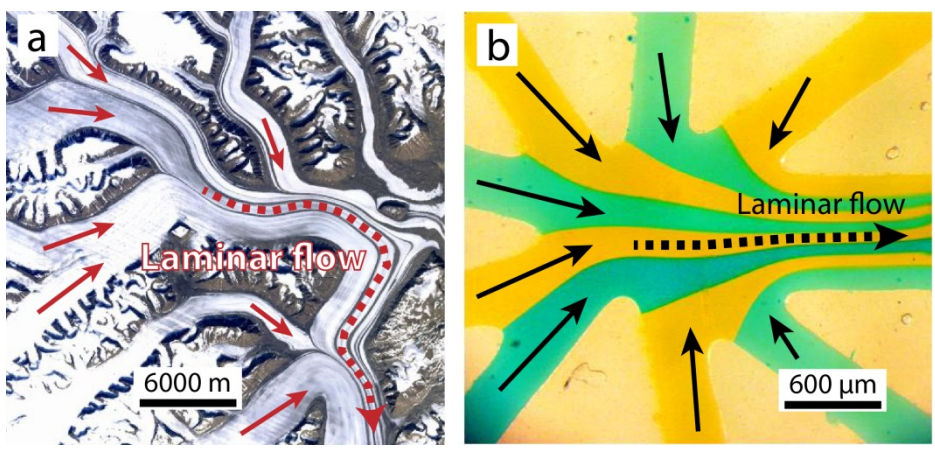

Figure 6, Macro and microscale laminar flow. A 5 km wide Greenlandic glacier (latitude 69.461952, longitude -25.158733 in Google Maps satellite images) exhibits laminar flow with dirty patches that can be seen to flow parallel to each other due to the low flow rate and high viscosity of the ice (a). A microfluidic channel with sufficiently slow flow and small dimensions also exhibit laminar flow properties which allow multiple sheath flows to flow in parallel without mixing (b).

By determining the Reynolds number (**Re**), it is possible to predict whether or not a flow system will have laminar properties. The **Re** is named after Osborne Reynolds who investigated water flow in pipes and suggested that "the birth of eddies depend on some definite value" of the relationship between inertial and viscous forces (Eq. 2)[72]. Reynolds performed his studies in round pipes which meant that the diameter of the pipe was readily available; however for noncircular tubes and channels, like most microfluidic chips, it is common to use the hydraulic diameter (D_H) instead (Eq. 3). Flow with **Re** < 2300 is considered laminar (e.g., the FFA channel in paper V has **Re** ~10 at a flow of 100 µl min^{-1}).

$$Re = \frac{\rho D_H v}{\eta} = \frac{Q D_H}{\nu A} \qquad \textit{Eq. 2 Reynolds number}$$

$$D_H = \frac{4A}{P_{wet}} \qquad Eq.3\ Hydraulic\ diameter$$

$\rho = density\ of\ the\ fluid$

$\eta = dynamic\ viscosity\ of\ the\ fluid$ ($\nu = kinematic\ viscosity\ of\ the\ fluid$)

$v = mean\ velocity\ of\ the\ fluid$ ($Q = volumetric\ flow\ velocity\ of\ the\ fluid$)

$A = cross - sectional\ area\ of\ the\ channel$

$P_{wet} = wetted\ perimeter\ for\ the\ cross - section$

Parabolic flow

The volumetric laminar flow of a Newtonian fluid along a pressure gradient in a translational invariant (infinite) circular tube can be calculated using Poiseuille's Law (Eq. 4). The flow profile will be parabolic due to the friction between each fluid layer, caused by viscosity, which counteracts the pressure force applied to the fluid. The non-moving walls of the channel slow the fluid layer closest to the wall to a standstill, but the next fluid layer will be able to move a bit since the friction is finite. The gradual increase in fluid layer velocity continues as layers get further away from the wall and in the cross sectional centre, where the fluid layer is least affected by the walls, maximum flow can be found. There is no analytical solution for the flow profile in rectangular channels but in low aspect ratio (<0.1) channels, it can be approximated by the analytical solution for flow between two parallel plates (Eq. 5). Most of the channels described in papers I-V have moderate aspect ratios (0.1-0.4) and the flow in them are better described using a series solution of NS equations with a no-slip condition (Eq. 6)[73]. Luckily the series converges fast and after 5 iterations the theoretical flow discrepancy is less than 5%. These equations help to predict particle velocities in microfluidic channels given a certain position.

$$Q = \frac{\Delta P \pi r^4}{8\eta l} \qquad Eq.4\ Poiseuille's\ law\ for\ a\ circular\ tube$$

$$v_x(z) = \frac{\Delta P}{2\eta l}(h - z)z \qquad Eq.5\ Flow\ velocity\ between\ two\ parallel\ plates$$

$$v_x(y,z) = \frac{4h^2\Delta P}{\pi^3 \eta l} \sum_{n=1,3,5\ldots}^{\infty} \frac{1}{n^3}\left[1 - \frac{\cosh\left(n\pi\frac{y}{h}\right)}{\cosh\left(n\pi\frac{w}{2h}\right)}\right]\sin\left(n\pi\frac{z}{h}\right) \qquad Eq.6\ Series\ solution\ of\ NS$$

$Q = volumetric\ flow\ velocity$

$\Delta P = pressure\ drop\ along\ length\ l\ of\ investigated\ geometry$

$r = radius\ of\ the\ tube$

$\eta = dynamic\ viscosity\ of\ the\ fluid$

$v_x = Flow\ velocity\ due\ to\ pressure\ gradient\ \nabla P\ along\ x - channel\ flow\ direction$

$l = length\ of\ investigated\ geometry\ section\ (x - direction)$

$h = height\ (smallest\ dimension)\ of\ investigated\ geometry\ (z - direction)$

$w = width\ (largest\ dimension)\ of\ investigated\ geometry\ (y - direction)$

Stokes drag

The governing forces that determine flow in a channel has been presented and it is time to look at how particles suspended in these flows will behave when exposed to the forces that are used to manipulate particles in fluids. Given laminar flow, a small particle moving in a fluid will experience a frictional force analogous to the viscous effects that slow down the fluid layers close to a wall. This impeding viscous drag force (F_d) can be calculated using Stokes' law (Eq. 7). The Stokes' law equation assumes the presence of laminar flow, smooth surfaces and homogeneous spherical particles that does not interact with each other.

$F_d = 6\pi\eta r v$ $\qquad$ $Eq.7\ Stokes'\ law\ for\ drag\ force\ on\ a\ particle$

$\eta = dynamic\ viscosity\ of\ the\ fluid$

$r = radius\ of\ the\ particle$

$v = velocity\ of\ the\ particle$

It should be noted that Stokes drag works in opposition to most external force particle manipulation techniques, including acoustic forces. Furthermore the drag force depends on the radius, as compared to acoustic forces which scales with particle volume, making acoustic manipulation of sub-micron particles difficult while larger particles (>1-2 μm) can be handled using relatively low acoustic power at a frequency range of 1-2 MHz (Fig. 7).

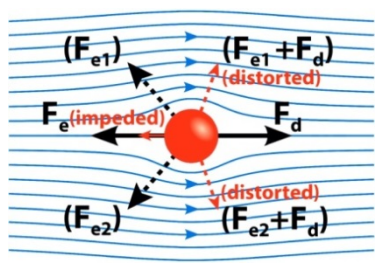

Figure 7, The Stokes drag force which counteracts external force particle manipulation. Due to the nature of the Stokes drag (F_d), the external force (F_e) manipulation of particles will be less efficient ($F_e + F_d$ results in an impeding effect on particle movement, red arrow). Stokes drag might also cause erroneous separation or positioning ($F_e + F_d$ results in distorted particle paths, red dashed arrows) when fluid streamlines deflect particles from moving along the external force axis and instead move them along the resultant force direction.

Particle manipulation methods

This section introduces several particle manipulation methods, divided into passive and active force manipulation on the macro and microscale. The main advantage of passive manipulation is the absence of external force generation which might facilitate simplified system integration in comparison to active methods that often involve additional instrumentation. The drawbacks for macroscale passive systems include e.g., particle shear stress and high sheath flow requirements which entail the use of large fluid volumes. The corresponding microscale aspects include the need for flow stability, small channel dimensions (to induce steep flow field gradients) that inherently impacts throughput and may cause clogging, and the fact that separation is mainly based on particle diameter or hydrodynamic size. The main advantage of active manipulation is the ability to separate or position particles based on multiple properties in addition to size e.g., density, magnetic susceptibility, charge, compressibility, di-polarity, optic refractive index or surface chemistry, with less need for small channel geometries which may facilitate higher throughput compared to passive micro systems. For easy comparison the main characteristics of each manipulation method are presented in a table format at the end of this section (Table 1).

Passive manipulation on the macroscale

Sheath flow lamination

The method of using sheath flows to laminate suspended particles into a narrow, spatially well confined stream was one of the first examples of particle manipulation using laminar systems[74,75]. It is currently the standard method for particle positioning in flow cytometers due to its robust nature and the fact that it is fairly simple to implement while permitting high throughput[76]. The core sample suspension is introduced into the sheath liquid through a capillary in a flow cell, which narrows into an aperture to achieve high fluid velocities, thus allowing higher detection rates and improved optical detection conditions due to uniform particle positions (Fig. 8a). The drawback of the sheath flow method in macroscale systems is the large consumption of sheath fluids (~0.1-1 L per hour) which prohibits miniaturization and leads to increased operating costs.

Centrifugation

A centrifuge may be used to concentrate or separate suspended particles or macro molecules according to weight or size by artificially increasing the "gravity", thus simulating an increased sedimentation rate of the particles. At relatively low RPMs (~1000) the centrifuge can be used as a clinical preparative instrument to concentrate larger particles and cells into pellets, while higher RPMs (~10 000) is needed to concentrate DNA or denatured proteins[77,78]. At extremely high RPMs (>50 000) an "ultracentrifuge", often reaching relative centrifugal forces of more than 500 000 times that of earth's gravity given a certain rotor radius, can be used to analyse particle and macro molecule properties including molecular weight or sedimentation coefficients[79,80]. As in the case of macroscale sheath flow

instruments, the centrifuges are also lab workhorses with fairly simple working principles but suffer the drawbacks of being quite bulky and only handling batch samples which prohibits easy integration into online systems. Furthermore, centrifuge operation is often time consuming and require multi-step protocols and extensive manual sample preparation.

Density gradient separation

By suspending particles into a sample tube filled with varying density media, Bøyum showed that it is possible to use a centrifuge to speed up the separation of particles according to density[81–83]. The procedure can isolate cell subpopulations with fairly high purity and is the standard method for blood fractionation[84]. As in the case of other centrifuges the instrumentation is bulky and the labour intense sample handling involves lengthy protocols and delicate pipetting when layering the different density media in the sample tube (Fig. 8b).

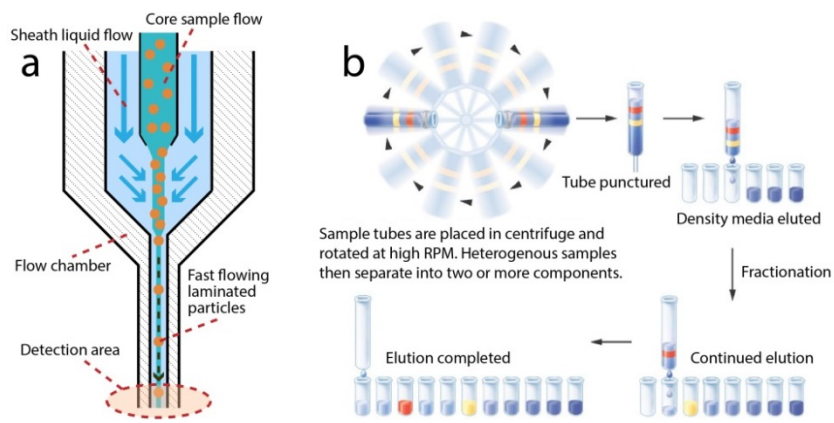

Figure 8, Macroscale particle manipulation methods. Particle positioning using a flow chamber in which a core sample stream is laminated by sheath fluids, and then forced through an aperture prior to detection, is the standard method for increasing performance in flow cytometers (a). By centrifugation of a particle sample suspended in media layers with different density it is possible to fractionate cell populations (b). By using only one media density it is also possible to concentrate particles into pellets. However, both centrifugation methods often require extensive sample handling protocols for density media layering as well as sample elution.

Passive manipulation on the microscale

Sheath flow lamination

Through the improvements in microfabrication techniques during the last decades it has now become possible to manipulate particles using microfluidic networks with sheath and sample flows[19,28]. By clever design including layered channels made from silicon, PDMS and resin compounds and "chimney"-like structures it is possible to achieve similar sheath flow lamination effects as on the macroscale (Fig. 9)[31,41,85–88]. The benefits of microfluidic sheath flow positioning of particles include increased spatial and temporal control of particle positions and the possibility to integrate the positioning zone with other functions on a microchip, thus increasing performance of several Lab-on-a-Chip applications[89–91]. The

drawbacks include decreased sample throughput inherent with miniaturization and less reliable operation due to gas bubble formation caused by steep fluid pressure gradients in the microscale channels, clogging in narrow apertures or other problems with flow control, which commonly are not an issue during macroscale sheath-flow positioning. These issues have been a driving force for the development of sheathless active force manipulation techniques (presented in the active manipulation section below).

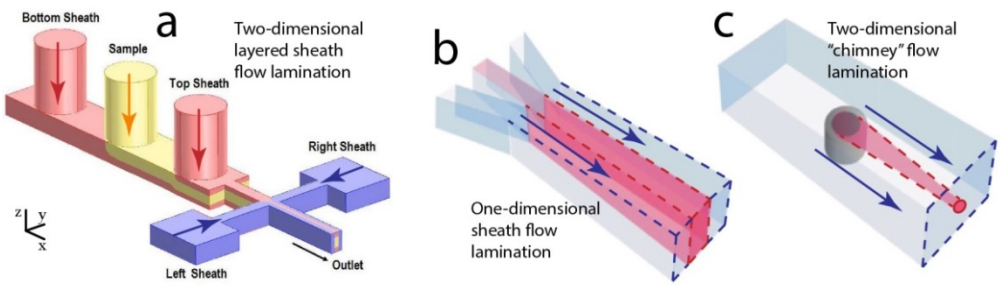

Figure 9, Sheath flow lamination using multiple flows or intricate chimney structures. Two-dimensional (2D) lamination of a sample suspension can be accomplished with multiple layered sheath flows (a). Instead of using normal one-dimensional lamination (b), 2D-lamination can also be performed by adding integrated flow outlets e.g., a chimney through which a sample fluid can be introduced into a sheath flow (c). *Adapted with permission: Rhee[88] (a) and Wolff[89] (b and c).*

Inertial forces

Suspended particles in a confined straight microfluidic channel with high flow velocity will be subject to two inertial "lift" forces acting in opposite directions as first observed by Segré and Silberberg [32,92–94]. The first force, called the Saffman force[95], is the induced lift force caused by the steep shear gradient in the confined channel which pushes the particle away from the centre towards the wall[92,96]. Acting in opposition to the shear gradient lift is a "wall effect" lift force caused by the asymmetric wake of a particle travelling close to a wall which pushes it away from the wall[97–99]. Given stable flows, the particles will then be positioned in the equilibrium between these two forces (Fig. 10a)[23,32]. By using inertial forces it is possible to achieve precise positioning and separation of particles according to size, shape or deformability with high throughput without the need of sheath flows[100,101]. The drawbacks include high shear stress on particles which might damage cells and the constraint on channel geometry which so far dictates that the channels can only be ~5-7 times wider than the diameter of the suspended particles in order to achieve satisfying inertial positioning[102].

Dean flow

Recently the inertial focusing method has been improved by utilizing Dean flows in curved channels[103]. In a curved channel the Saffman force and the wall effect are complemented by Dean flow vortices that move the particles more rapidly towards their equilibrium points[33,104]. A curved or spiral channel also introduces centrifugal forces which helps push particles away from the inner curve wall and Magnus forces (due to the rotation of the particle in a curve) which acts in the opposite direction (Fig. 10b)[105]. These additional forces allow Dean flow channels to not only position particles ~5 times faster than straight

inertial focusing channels, but also allow higher flow rates and create new equilibrium points into which particles may be positioned[102]. The method does however suffer from the same drawbacks as traditional inertial methods, namely shear stress on cells and the need for narrow channel geometries in at least one dimension.

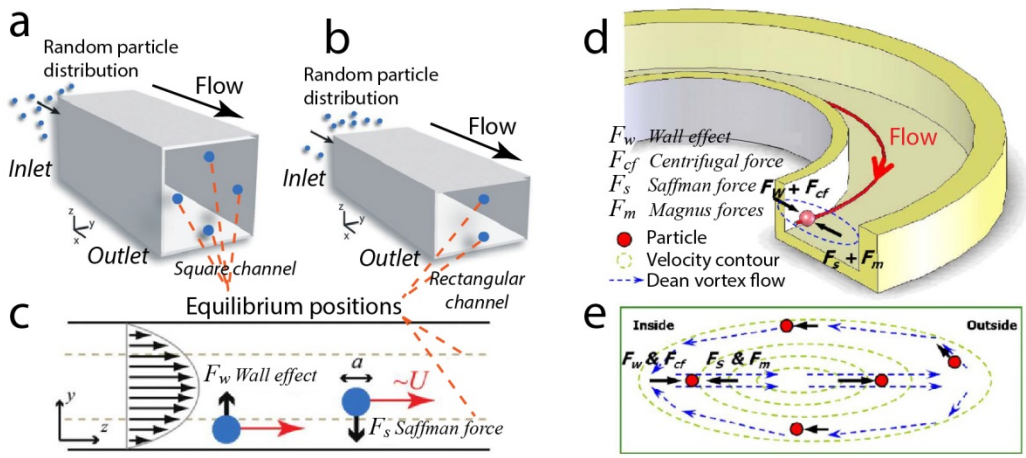

Figure 10, Inertial forces and Dean flow manipulation of particles. Narrow channels with high flow rates can be used to position particles in the equilibrium points between the wall lift effect and the opposite direction Saffman lift force (a-c). By designing curved channels it is possible to achieve faster focusing of the particles with the help of Dean flow vortices that induce centrifugal and Magnus forces in addition to the lift forces (d-e). *Adapted with permission: Amini[102] (a-c) and Seo[105] (d and e).*

Pinched flow fractionation

Pinched flow fractionation (PFF), first presented by Yamada et al.[34], utilizes the parabolic flow profile to sort particles according to size. The method uses a sheath flow to align particles close to a wall in a "pinched" segment of a channel, often less than ten particle diameters wide. The method does not rely on any inertial forces but rather the size of each particle which allows the centre of small particles to be positioned closer to the wall in the pinched section parabolic flow profile while larger particles do not fit close to the wall and have their centre positioned further out from the wall. The pinched section then widens abruptly which causes particles to be deflected in the laminar flow expansion according to their lateral position (defined by size) (Fig. 11a)[106–110]. The method can achieve reasonably high separation sensitivity but suffers from low throughput and issues with erroneous separation due to clogging or unstable flow, which alters the deflection angle of particles in a critical way.

Deterministic lateral displacement (Bumper array separation)

Deterministic lateral displacement (DLD) particle handling, first described by Huang et al.[35], is a method related to PFF but it uses particle positions in laminar flow rather than a parabolic flow to continuously separate particles with different size, shape or deformability. In DLD, particles flow through an obstacle (pillar) matrix. By slightly shifting the horizontal position of downstream obstacle rows in relation to previous rows, the particles

are forced to flow to either side of the downstream obstacles according to their hydrodynamic size[111–113]. A small or highly deformable particle might then move in a fairly straight path through the obstacle matrix, sometimes deflected to the left and sometimes to the right, while a larger particle would continuously be deflected along one direction, further and further away from its original position in the laminar flow profile (Fig. 11b)[114]. DLD systems can achieve very good size discrimination (~10 nm) and are thus able to sort sub-micron particles in highly concentrated samples, with the possibility of tuning the separation size cut off [26,35]. Drawbacks of DLD include an inclination for clogging, due to the narrow channel spaces inherent to the working principle. Virtual or functionalized DLD have also been presented, using methods (e.g., DEP) that are described in the active force section below[115,116].

Hydrophoresis

Other types of microstructure obstacles, e.g., grooves, herringbone patterns and chevrons, have also been used to perform passive separation of particles. In these systems the separation is caused by particle interactions with pressure gradient induced stream vortices caused by the microstructures (Fig. 11c)[36]. The concept is referred to as hydrophoresis and has been shown to separate or trap micro and nanoscale particles[117,118]. Method advantages include the ability for sheathless and continuous separation of concentrated samples, with less risk of clogging compared to DLD. The drawbacks include low size discrimination, a need for stable flows and fairly low throughput even though recently some applications of the method (particle positioning) has shown to be flow rate insensitive[119].

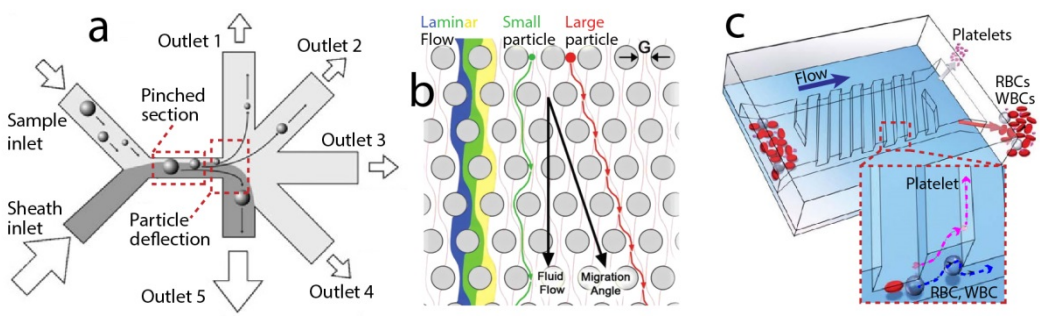

Figure 11, Passive micro separation techniques that utilize channel geometries and flow profiles. Pinched flow fractionation deflects different size particles in a parabolic flow profile into different outlets (a). Deterministic lateral displacement uses an obstacle matrix for high precision size or deformability sorting of particles in laminar flow (b). Hydrophoresis uses flow obstacles to generate stream vortices that sort particles according to their hydrodynamic profile (c). *Adapted with permission: Takagi[110](a), Inglis[114](b) and Choi[118](c).*

Active manipulation

Dielectrophoresis

Dielectrophoresis (DEP) is a method that allows manipulation of particles based on the interaction between the dipole of the particles and the field gradient of an inhomogeneous

electric field[22,42,120,121]. DEP-forces are proportional to the permittivity and conductivity of the suspension medium and the particles as well as the particle volume and the frequency of the electric field. The di-polarity is either inherent to the particle material (atom orientation) or induced (on the surface of non-conducting particles) by the electric field. The inhomogeneous electric field gradient is either created by alternating currents from electrodes placed inside the microfluidic channel (AC-DEP) (Fig. 12a) or by applying a direct current field across a channel with isolating obstacles (DC-DEP, iDEP) (Fig. 12b)[122,123]. Depending on their electrical properties particles can either be attracted (p-DEP) or repelled (n-DEP) from the electric field maxima. By clever design of the isolating obstacles, electrode configuration, field strengths and frequency it is possible to position[124], separate, orientate or trap[125] particles (n- and p-DEP), cells (n-DEP)[37] and sub-micron biological material like DNA-strands using DEP-forces. The varying application areas and the ability to manipulate particles based on electric properties are the advantages of using DEP compared to most passive methods. It is also possible to complement passive methods e.g., DLD with DEP[115] (Fig. 12c). The drawback of DEP include low force strength, which impacts flow rates and throughput, as well as erroneous operation due to dirty electrodes during biofluid handling[126,127] and heating of the media by the often strong electric fields used in DC-DEP which might cause gas bubble formation or cell damage[128].

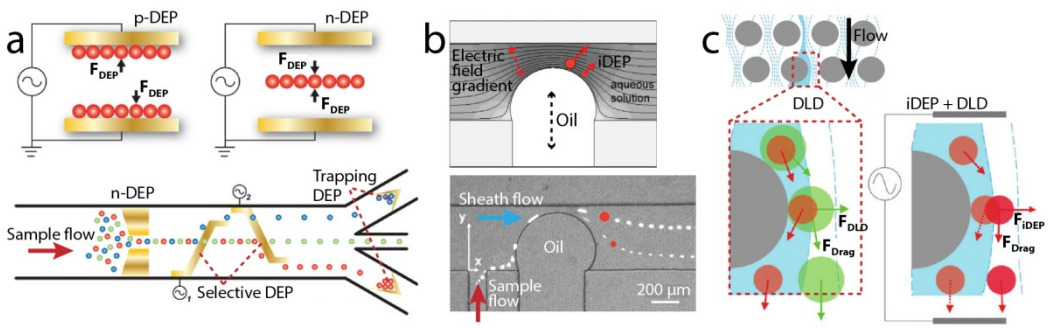

Figure 12, Dielectrophoretic sorting of particles. By generating an inhomogeneous electric field over a particle suspension it is possible to manipulate particles by using electrodes to apply alternating currents within a chip (AC-DEP) (a). By introducing isolating obstacles (in this case an oil drop) in a direct current field it is also possible to create an inhomogeneous field gradient (DC-DEP, iDEP) (b). It is also possible to combine DEP with passive methods e.g., DLD to perform separation based on multiple particle properties (c). *Adapted with permission: Gossett[24](a), Barbulovic[123](b) and Beech[115](c).*

Magnetophoresis

Analogous to DEP, it is also possible to use magnetic fields in order to manipulate particles[38,129,130]. Traditionally, magnetic separation was done in batches[131] but recent advances in the microfluidic field have allowed continuous flow magnetic sorting, referred to as magnetophoresis (Fig. 13)[132]. The magnetic field is either produced by permanent magnets, actively induced with electromagnets (coils) or microfabricated micromagnets. With the exception of red blood cells[133], most cells and particles are nonmagnetic and must be functionalized with magnetic beads in order to be manipulated[134]. While this procedure requires extensive sample preparation compared to some of the other manipulation

techniques, it allows cells to be sorted according to their surface chemistry, which most other sorting methods do not. By fluorescent labelling of the magnetic beads the sorted samples may also be analysed in a flow cytometer[135]. Size sorting is facilitated by the varying amounts of magnetic beads that bind to sample particles according to their surface area. Targeted magnetic bead labelling allows isolation of subpopulations in complex biofluids. Whilst facilitating continuous separation, positioning or trapping of particles according to size or surface chemistry, the method suffers from issues with clogging of the magnetic beads as well as inconsistent binding of the functionalized beads due to insufficient mixing.

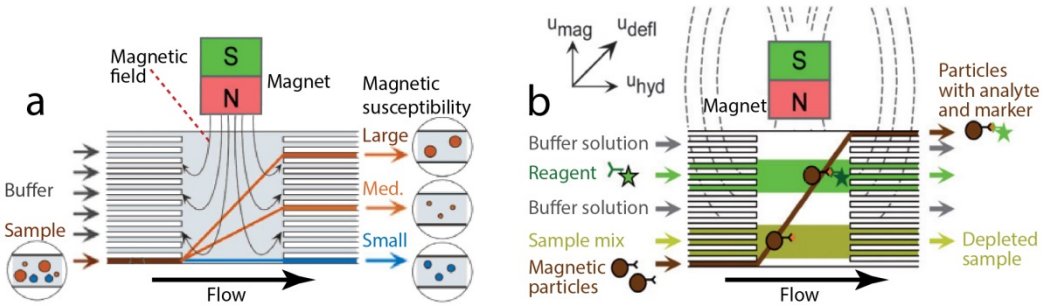

Figure 13, Magnetophoretic sorting of particles by size or surface chemistry. It is possible to attach small magnetic beads in order to functionalize cells or other particles and then sort them according to magnetic susceptibility (a) or surface chemistry which allows multistep bioassays to be performed (b). The magnetic beads can also be labelled fluorescently to allow subsequent flow cytometry. *Adapted with permission: Pamme*[129] *(a) and Peyman*[136] *(b).*

Optic manipulation (Optical tweezers)

With the invention of the laser it became possible to manipulate particles by focused beams of light, as first presented by Ashkin[137–139]. Particles inside the laser beam are subject to radiation pressure (directed away from the light source) and axial gradient forces (acting towards the beam focal point) (Fig. 14a). The radiation pressure normally dominates and in order to capture and manipulate the particles it is vital to design systems with focal points where the axial gradient force is strong enough to dominate. This requires beams that are highly divergent outside the focal point, normally found in microscope lenses with high numerical apertures and minimal aberration. Particles that are much smaller than the wavelength of the light are drawn towards higher beam intensity by dipole interaction with the electric field of the light. A large particle scatters the photons away from the itself and is then forced towards the higher light intensity due to the recoil from the redirected photons. Microstructure lattices have recently facilitated additional functionality by allowing multi-well trapping and continuous sorting of particles (Fig. 14b)[140,141]. Optic switching using fluorescently actuated optical tweezers has also been presented[39]. Compared to other active force methods, optics allow particles to be trapped in three dimensions and sorted by size as well as optical properties like refractive index and polarizability[25,142]. The drawbacks include the relatively low forces exerted on the particles, heating issues and the need for transparent materials or waveguides which limit design options[21].

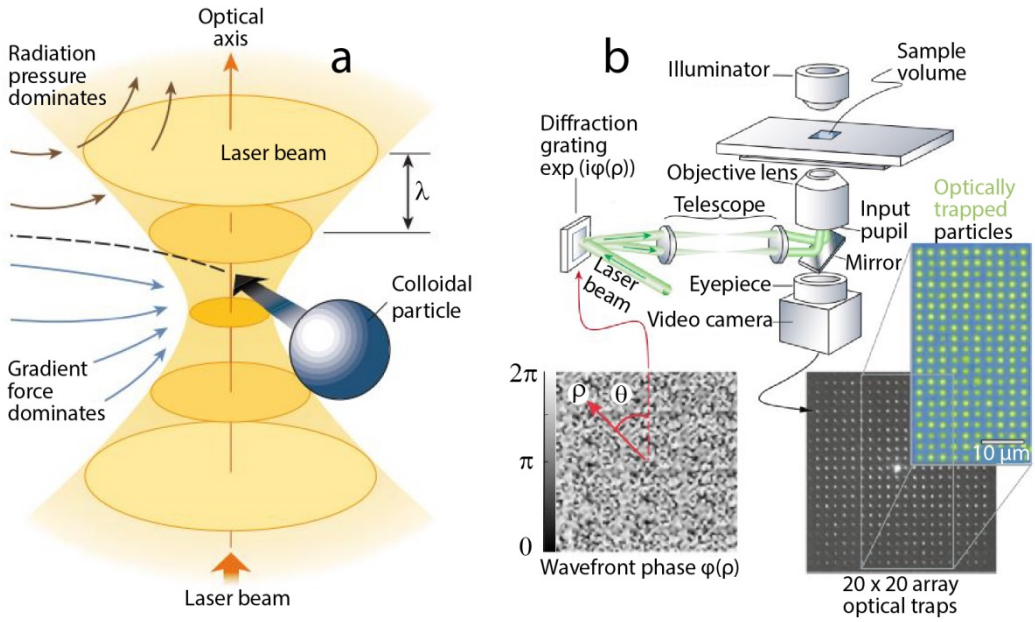

Figure 14, **Optic manipulation of particles.** Particles impacted by an intense beam of light will be subject to light radiation pressure forces directed away from the light source along the optical axis which can be counteracted by axial gradient forces in the beam focus in order to trap and manipulate particles (a). The development of microstructure lattices has enabled concurrent manipulation of multiple particles (b). *Adapted with permission: Grier*[25] *(a) and Curtis*[141] *(b).*

Acoustophoresis

The method of using acoustic forces to manipulate particles, frequently referred to as acoustophoresis, is thoroughly described in other sections but a short description is included here for easy comparison with the other methods. Acoustofluidic systems manipulate particles according to size as well as density and compressibility differences between the particles and the suspending medium. Acoustofluidic applications are based on either surface acoustic waves (SAW) or bulk acoustic waves (BAW). BAW-systems form the basis for this dissertation and were first presented during the 1990s[40,43,51,52,143–148]. By adjusting the acoustofluidic channel geometry to allow standing waves in the fluid at ~1-5 MHz, the BAW-systems efficiently manipulate suspended particles (Fig. 15a)[45–48,56,62,65,66,69,149–154]. BAW-systems are most frequently actuated with piezoceramic transducers that are attached to an acoustofluidic chip. SAW-systems have been developed over the last 5-10 years[155–157]. They are often actuated by interdigital transducers (IDTs) that are patterned on piezoelectric materials and operated at 10-1000 MHz to induce the SAWs. A fluidic chamber or channel can then be placed on top of the piezoelectric material to allow particle manipulation. Depending on the application one or more IDTs can be used to either move particles in a channel or position them in arrays (Fig. 15b)[158–160]. By forming standing SAWs (SSAWs) it is possible to reproduce the nodal patterns of BAWs in a SAW-system, although with less effective manipulation of particles due to a higher acoustic attenuation (Fig. 15c) [161,162]. Acoustofluidic systems have been shown to focus, separate, align, pattern and trap particles and cells in a gentle way[163–165]. BAW-systems are more efficient than

SAWs when dealing with cell sized particles and can handle larger suspension volumes. The drawbacks of BAW include the need for highly resonant designs and low attenuation materials. Active cooling or frequency calibrations are sometimes needed in order to achieve stable acoustic fields in systems where transducer actuation leads to heating[67]. In addition to sub-micron particle manipulation SAW-systems can drive flows and also be used to manipulate and mix droplets and allow rapid fluid switching by induced streaming[166,167]. Compared to BAW, which is inefficient in soft materials[168], SAW manipulation can also be performed in acoustically attenuating materials like PDMS but the need for complex IDTs and the nature of SAW propagation and attenuation impacts throughput and integration versatility.

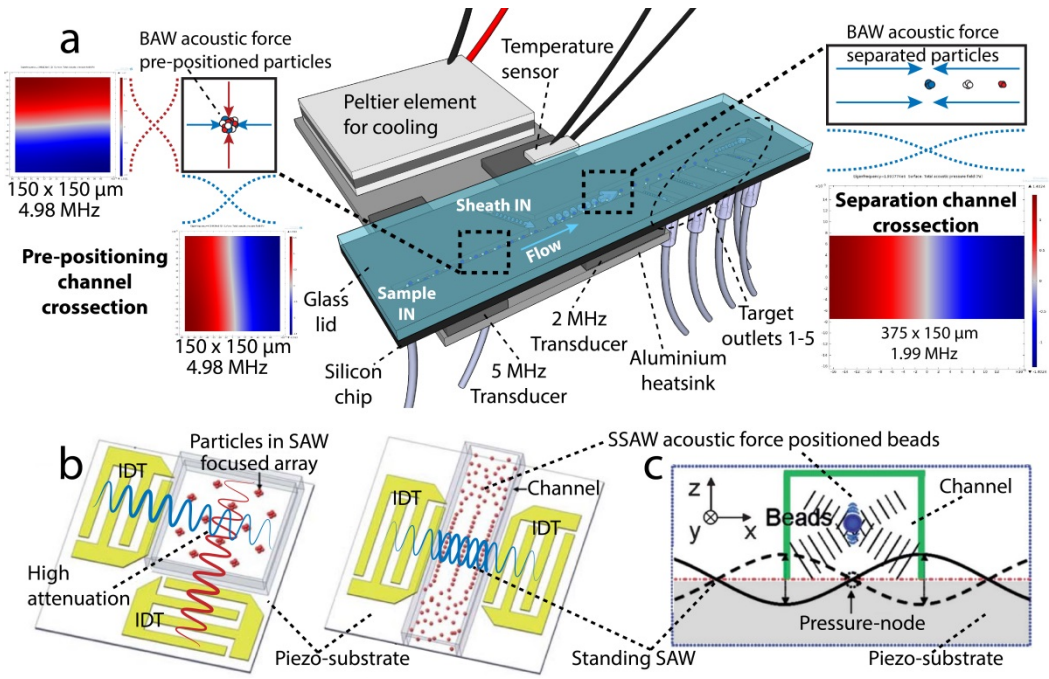

Figure 15, Bulk and surface acoustic wave force particle manipulation. Standing bulk acoustic waves (BAW) can be used to manipulate suspended particles in a medium in order to position them precisely or sort them according to size, compressibility or density e.g., like in paper V where improved size sorting of particles and cells are performed with the aid of a pre-positioning channel (a). The BAWs are induced with piezoceramic transducers that vibrate the bulk of the acoustofluidic chip which causes standing waves to form in the suspension medium. Surface acoustic waves (SAWs) are often induced with interdigital transducers (IDTs) which are patterned on piezoelectric materials which then have channels or chambers placed on top. Depending on the application the IDTs can be positioned to focus or trap particles in arrays (b) or to perform two-dimensional positioning of particles in a channel by inducing standing SAWs (c). *Adapted with permission: Shi*[160]*(b) and Shi*[158]*(c).*

Table 1: **Comparison between micro particle manipulation techniques.**

Method	Manipulation induced by	Manipulation based on	Sample prep.	Throughput / Force amp.	Comment / known issues
Macro sheath flow lamin.	Laminar flow regime	Flow trajectory	-	High	Only offers positioning
Centrifugation	Centrifugal force	Density, (Size)	Pipetting	Batches	Manual workload
Density grad. separation	Centrifugal force	Density, (Size)	Extensive pipetting	Batches	High manual workload
Micro sheath flow lamin.	Laminar flow regime	Flow trajectory	-	High	Only offers positioning
Inertial force focusing	Wall and shear induced lift	Size, Shape, Deformability	Dilution if conc. ~blood	High	High shear, small channel
Dean flow focusing	Dean vortices, Inertial forces	Size, Shape, Deformability	Dilution if conc. ~blood	High	~5 x faster vs. inertial only
Pinched flow fractionation	Parabolic flow profile	Hydrodynamic size	Dilution	Low	Sensitive to flow flux
Deterministic lateral displac.	Obstacles in laminar flow	Size, Shape, Deformability	Filtration	Low-Medium	Good size discr., clogs
Hydrophoresis	Pressure gradient vortices	Size, (Shape)	Dilution if conc. ~blood	Medium	Sensitive to flow flux
Dielectrophoresis	Inhomogeneous electric field	Size, Polarizability	Conductive medium	Low	Heating may be an issue
Magnetophoresis	Magnectic field	Size, Magnetization	Label with mag. beads	Medium	Requires labelling
Optical tweezers	Optical radiation pressure field	Size, Refr.Ind., Polarizability	Dilution, pipetting	Low	Very precise, low force
Acoustophoresis	Acoustic pressure field	Size, Density, Compressibility	Dilution if conc. ~blood	High	Versatile, good for >1 μm dia.

Acoustics

This section introduces the field of acoustics and provides thorough understanding of the forces and mechanisms that govern the particle manipulation methods used in papers I-V.

History

As in the case with fluid mechanics we need to go back more than 2000 years in order to find the first writings on acoustic mechanics. During the 6th century B.C. Pythagoras made observations concerning how certain tones seem to fit well together. In China the "Chinese Spouting Bowl" was invented more than 2000 years ago. The bowl allows the user to create nodal patterns by filling the bowl with water and then rub it with a hand or object to actuate the resonant mode of the bowl with frictional energy. This was an early foray into the world of fundamental tones and harmonics, and how they depend on the geometry of

the vibrating medium, which is important to the designs in this dissertation. Robert Hooke (17th century) and Ernst Chladni (18th century)[169] later visualized the resonant patterns using particles instead of fluids, both of which are an example of "cymatics", or sound visualization (Fig. 16). Meanwhile, in 1863 Hermann Helmholtz explained many of the physical and physiological aspects of acoustics, music and the nature of vibrating (resonant) chambers filled with air, analogous to the liquid filled resonant chambers presented here[170]. The mathematical laws for these vibrations were described by Galileo Galilei in the 16th century when he investigated oscillating strings.

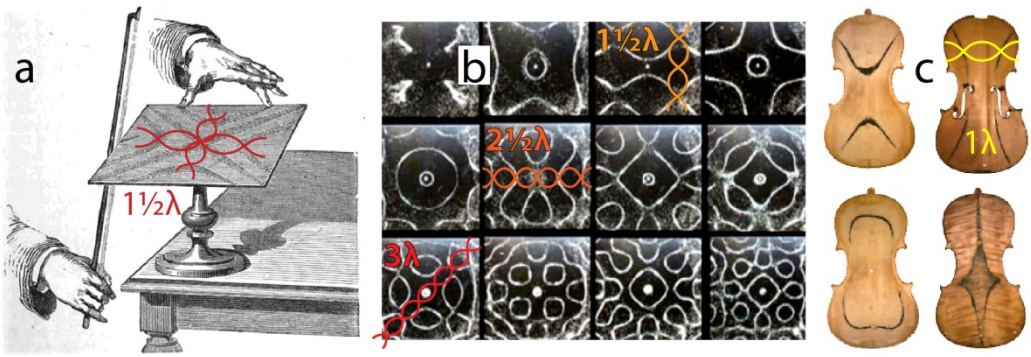

Figure 16, Cymatics – Visualized resonant acoustic patterns. Hooke and Chladni observed how a violin bow could be used to form patterns by the aggregation of small particles (flour and sand) along nodal lines on a resonating plate (a). Such a "Chladni plate" can be used to form a multitude of different resonance patterns depending on the varying wavelength resonant modes along different axes (b). The musical quality of a violin is also a result of resonance modes at various frequencies (an unmatched resonance might sound better) (c). *Adapted from "Elementary Lessons on Sound" 1879 (a) and University of New South Wales - Music Acoustics web (newt.phys.unsw.edu.au/jw/violindex.html) (c).*

The actual sound propagation was also a subject of study for the early philosophers and in the 4th century B.C. Aristotle wrote a treatise on sound and hearing in which he stated:

"Sound takes place when bodies strike the air, . . . by its being moved in a corresponding manner; the air being contracted and expanded and overtaken, and again struck by the impulses of the breath and the strings, for when air falls upon and strikes the air which is next to it, the air is carried forward with an impetus, and that which is contiguous to the first is carried onward; so that the same voice spreads every way as far as the motion of the air takes place."

The passage is still a good description of sound generation and propagation by means of contraction and expansion. Newton described the speed of the sound propagation as dependant on pressure and density in 1687 (Principia vol. 2) but his equation was only valid for an isothermal process and it was not until 1816 that Laplace introduced an equation for adiabatic processes (unknown at the time of Newton's Principia). The notion of acoustic radiation forces as a result of these compression waves hitting objects was then introduced by Lord Rayleigh[171,172] during the late 19th and early 20th century, and laid the foundation for acoustic particle manipulation. During the 20th century Louis V. King[173],

Yosioka and Kawasima[174] and Lev P. Gorkov[175] explained how this radiation force acts on particles.

Wave propagation

Sound waves can be seen as pressure differences propagating through a medium. The pressure changes move by contracting and expanding the medium. On a molecular scale the wave actually forms from the average movement of countless molecules, some of which travel faster than the wave, some slower and some in another direction, but the aggregate directional movement is what constitutes the wave. The velocity of the contraction/expansion (wave velocity) or the pressure change in the medium can be described by the wave equation (Eq. 8), which stems from the conservation of momentum and mass.

$$\frac{\partial^2 v}{\partial^2 t} = c^2 \nabla v \qquad \textit{Eq. 8 Wave equation expressed for velocity}$$

$v = \textit{displacement velocity}$

$c = \textit{speed of sound}$

The speed of sound depends on the compressibility and the density of the medium rather than the pressure (Eq. 9). This can be explained intuitively by imagining how the bustling masses of molecules that form the wave are affected by pressure, temperature, compressibility and density. An increase in pressure only translates to more random collisions between the molecules but they will still move at the same speed (and not communicate pressure change faster). However, when the temperature increases, so will the speed at which the molecules travel and communicate the pressure change. Reversely, heavier molecules will move sluggishly, thus slowing down the compression wave, while an increased compressibility means that compression waves move slower since the material will "cushion" them. By this follow that the often high sound velocity in dense materials is a result of the decrease in compressibility, which dominates the effect of increased molecule weight in these materials.

$$c = \frac{1}{\sqrt{\kappa \rho}} = \sqrt{\frac{B}{\rho}} \qquad \textit{Eq. 9 Speed of sound}$$

$\kappa = \textit{compressibility}$

$\rho = \textit{density}$

$B = \textit{bulk modulus of the material}$ ($\textit{sometimes more readily available than } \kappa$)

Standing waves

In solids the sound propagates with both longitudinal (compression) and transverse (shear displacement) waves but in a fluid such as water the wave only travels through compression (Fig. 17a). The longitudinal wave can be described using a sinusoidal function (Eq. 10).

$$y(x,t) = A\sin(\omega t \pm kx) \qquad Eq.\,10\ Travelling\ wave\ function$$

$$A = displacement\ amplitude$$

$$\omega = angular\ frequency\ \frac{2\pi}{T}, T = period$$

$$k = wave\ number\ \frac{2\pi}{\lambda}(spatial\ frequency)$$

Unless the displacement amplitude of the wave is extremely high, which would require a powerful transducer; it would not be feasible to manipulate cell sized particles. In order to increase the displacement amplitude while keeping the transducer effect at moderate levels researchers use standing waves. A standing wave is an interaction between an incident wave and a reflected wave which results in combined higher wave amplitude and occurs at material interfaces with unevenly matched acoustic impedances (Eq. 11). The acoustic impedance is a material property that describes how well particle movement translates into pressure waves; for a longitudinal wave with a certain frequency it can be expressed as a product of the density and speed of sound in the material (Eq. 12). Interfaces with large differences in acoustic impedance reflect more of the incident wave compared to acoustic impedance-matched materials. Examples of such interfaces are the air-rock boundary in an "echo" mountain valley or the water-silicon boundary found at the walls in most of the microfluidic channels in this dissertation. By adjusting the width of an acoustically actuated channel with reflecting walls at both sides to a multiple of half wavelengths, sound waves may be reflected and interact more than once, which makes it possible to achieve high (~2 MPa)[176] pressure amplitudes at certain points along the channel cross section. Owing to the sinusoidal nature of the wave function, these points are positioned half a wavelength away from each other, with the first point positioned a quarter wavelength away from the reflecting wall (Fig. 17b). The reflected amplitude coefficient ($\boldsymbol{R}$), which is the ratio between the acoustic impedances of the materials at the interface, can be used to predict how much of the acoustic energy ($\boldsymbol{R^2}$) that will be reflected (Eq. 13). These calculations are important when deciding what materials to use in an acoustofluidic chip. For instance, a water (Z_{wa}=1.5 MPasm^{-1}) - silicon (Z_{si}=20 MPasm^{-1}) boundary reflects ~74% of the incident wave energy while a water (Z_{wa}=1.5 MPasm^{-1}) - borosilicate glass (Z_{si}=13 MPasm^{-1}) boundary only reflects ~63% of the energy, making silicon preferable in order to achieve maximum standing wave pressure. Meanwhile, a PDMS structure (~1.1 MPasm^{-1}) will reflect less than 5% of the incident wave acoustic energy which makes standing wave formation very hard to achieve.

$$y(x,t) = A_{SW}\sin(kx)\cdot\cos(\omega t) \qquad Eq.\,11\ Standing\ wave\ function$$

$$A_{SW} = displacement\ amplitude\ for\ the\ standing\ wave$$

$\omega = angular\ frequency\ \frac{2\pi}{T}, T = period$

$k = wave\ number \frac{2\pi}{\lambda} (spatial\ frequency)$

$Z = \rho c$ $\qquad$ $Eq.\ 12\ Specific\ acoustic\ impedance$

$\rho = density$

$c = speed\ of\ sound$

$R = \frac{Z_1 - Z_2}{Z_2 + Z_1}$ $\qquad$ $Eq.\ 13\ Reflected\ amplitude\ coefficient$

$Z_{1,2} = Acoustic\ impedance\ for\ the\ materials$

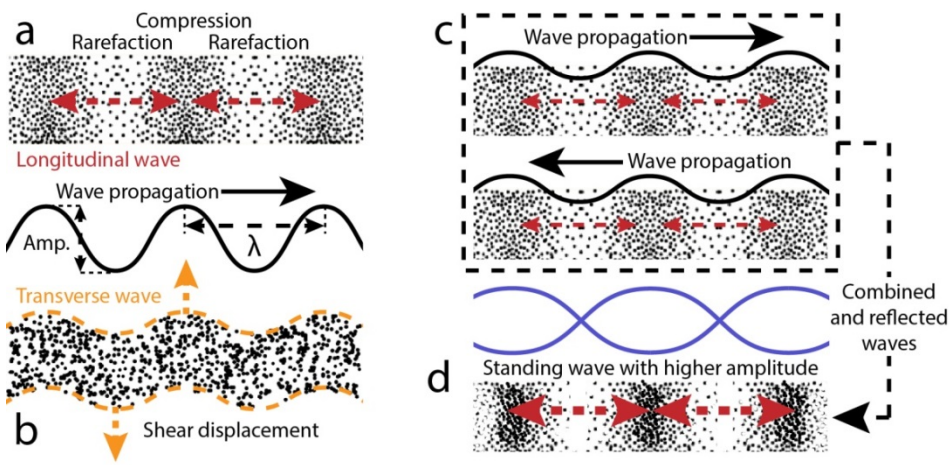

Figure 17, Longitudinal, transverse and standing waves. Solid materials allow the propagation of both longitudinal (compression - rarefaction) waves (a) and transverse (shear displacement) waves (b) while fluids only allow longitudinal propagation. By combining the acoustic forces in two propagating waves travelling in opposite directions (c), and allowing them to reflect in a carefully adjusted resonant chamber, it is possible to generate a standing wave with increased acoustic amplitude compared to the two original waves (d).

Acoustic radiation forces

As explained earlier it is possible to visualize the resonance modes of a material by actuating it at its fundamental or harmonic frequencies. Hooke used particles on a glass plate to visualize the transversal wave resonance patterns, further explored by Ernst Chladni, and in 1866 August Kundt invented the Kundt tube which allows visualization of the longitudinal compression wave in fluids[177]. By putting small and light particles like talcum powder in an air filled tube, and then using a transducer to generate sound at one end of the tube and reflecting the sound at the other end of the tube, it was possible for Kundt to tune the frequency to find the half wavelength resonant modes of the system at which standing

waves form and particles aggregate into the pressure nodal points along the tube (Fig. 18a-b). The force acting on the particles is called the acoustic radiation force and is the single most important force involved in acoustofluidic particle manipulation.

Lord Rayleigh described the general acoustic radiation force[172] in 1902 but it was not until 1934 that Louis V. King presented a theory regarding acoustic radiation forces acting on spheres[173], thus explaining the forces acting on particles in a Kundt tube. King's theory was valid for incompressible spheres in an inviscid fluid and would not be suited for modern experiments on cells. It was not until after K. Yosioka and Y. Kawasima accounted for finite compressibility of the sphere[174] in 1955, and Lev P. Gorkov 1962 revisited the original theory and accounted for viscosity as well as compressibility[175], that researchers were given the analytical tools needed to design acoustic systems for the manipulation of cell sized particles.

The most recent efforts to improve the theory were made by Doinikov in 1997 when he accounted for particle surface boundary conditions in a viscous fluid[178] and Settnes and Bruus who derived an analytical expression for the acoustic radiation force that include these conditions[179]. It should be noted that included in King's paper was a note about the several magnitudes higher forces acting on spheres in resonant standing wave fields in comparison to travelling wave fields. 60 years later that effect allowed researchers including Benes and Gröschl,[145,147] Mandralis and Feke[40] as well as Hawkes and Coakley[43,146] to develop half wavelength miniaturized systems with laminar flow in which particles were manipulated (Fig. 18c).

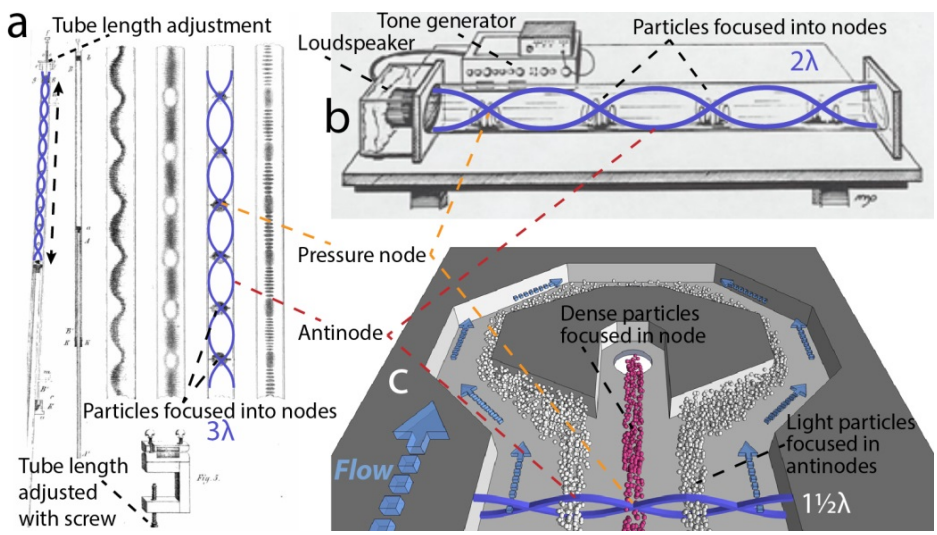

Figure 18, Kundt tubes and microchannel with standing wave acoustic radiation forces. In his original paper Kundt illustrated the patterns which we now know to be formed by the acoustic field pressure nodes (a). Kundt adjusted the length of the tube with a screw to form different patterns but it is also possible to achieve different patterns by using a tone generator to adjust the acoustic frequency in a constant length tube (b). The same node and antinode patterns can be used to manipulate particles in microfluidic channels (c). *Adapted from: UCLA Physics web (demoweb.physics.ucla.edu/content/100-kundts-tube) (b).*

Primary acoustic radiation force

The dominant force acting on a particle in an acoustic resonant field is the primary acoustic radiation force (PRF) which can be calculated for a system with known particle radius, density and compressibility; suspending medium density and compressibility, and field gradients for pressure and velocity (Eq. 14). The PRF acts in the direction of the pressure field gradient e.g. the direction of a standing wave (Fig. 19a). A suspended particle will scatter an incident wave which causes interference in the local pressure field surrounding the particle. Meanwhile, the pressure wave deformation of the compressible particle induces oscillations that interfere with the local velocity field.

The acoustic contrast factors f_1 and f_2 (Eqs. 15 and 16), which are coupled to the pressure and velocity fields respectively, is of special interest since they help us predict if a suspended particle will migrate to either the closest pressure or velocity node (pressure antinode) along the pressure wave direction. For convenience, f_1 and $f_2$can be combined into a single expression (ϕ) which is valid for 1D-simulations (Eq. 17). Positive ϕ-value particles will migrate to pressure nodes while particles with a negative ϕ-value migrate to pressure antinodes (Fig. 19b). The absolute value of ϕ relates to the PRF amplitude.

By comparing the absolute value and sign of the combined acoustic contrast factor ϕ (ACF) for different particles suspended in the same medium it is possible to evaluate whether or not a certain experiment or system design is feasible. An example would be the separation of white blood cells (WBCs) and fat (triglyceride globules) in water in which the cells have an ACF value of 0.17 which indicates that they will migrate to pressure nodes while the fat particles has an ACF of -0.23 and will migrate to pressure antinodes, indicating efficient separation of the two suspended populations. Acoustic properties and ACF in water for some frequently used materials can be found in table 2. It should be noted that even though RBCs seemingly moves faster to the nodes than the WBCs, they are also smaller in size on average which results in a similar translation velocity for both types of cells, making separation difficult.

$$F_{pri} = -\frac{4\pi a^3}{3}\left[f_1\frac{\kappa_m}{2}\nabla\langle p^2\rangle - f_2\frac{3\rho_m}{4}\nabla\langle v^2\rangle\right] \qquad \textit{Eq. 14 Primary acoustic radiation force}$$

$$f_1 = 1 - \frac{\kappa_p}{\kappa_m} \qquad \textit{Eq. 15 Acoustic contrast factor coupled to pressure field gradient}$$

$$f_2 = 1 - \frac{2\left(\frac{\rho_p}{\rho_m} - 1\right)}{2\frac{\rho_p}{\rho_m} + 1} \qquad \textit{Eq. 16 Acoustic contrast factor coupled to velocity field gradient}$$

$$\phi = \frac{5\rho_p - 2\rho_m}{2\rho_p + \rho_m} - \frac{\kappa_p}{\kappa_m} \qquad \textit{Eq. 17 Acoustic contrast factor}$$

$a = \textit{particle radius}$

$\kappa_m, \rho_m = \textit{medium compressibility and density}$

$\kappa_p, \rho_p = particle\ compressibility\ and\ density$

$p, v = pressure\ and\ velocity\ fields$

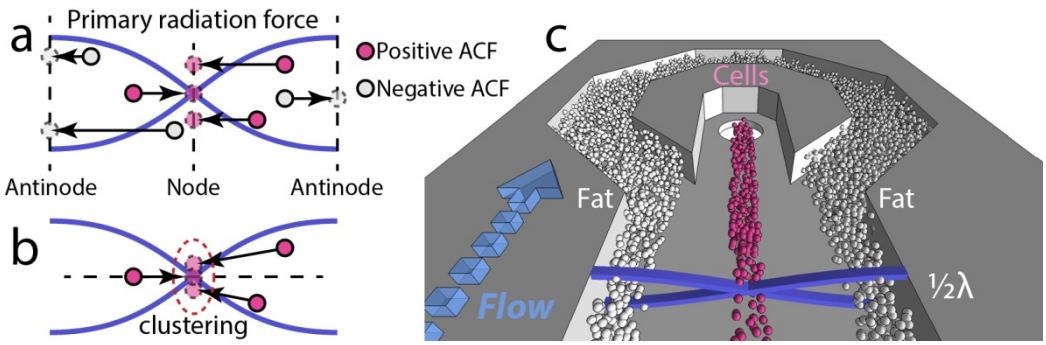

Figure 19, The primary acoustic radiation force and the acoustic contrast factor. Particles that are subject to the primary acoustic radiation force (PRF) will move towards either pressure or velocity nodes (pressure antinodes) depending of their acoustic contrast factor (ACF). The PRF acts in the direction of the pressure field gradient in the standing wave (a). In some system designs the acoustic field is localized in the resonant chamber which makes the particles cluster together because of the acoustic field gradient which might even be strong enough to trap particles against the flow of the suspending medium (b). The fact that positive ACF particles focus in the pressure nodes while negative particles focus into pressure antinodes allows binary separation e.g., in complex biofluids like raw milk where cells and fat can be separated (c).

Table 2, Acoustic properties for some frequently used materials

Material	Density kg/m3	Compressibility 10^{-10} Pa^{-1}	Acoustic contrast factor, ϕ, in water	Migration speed for given material volume
Polystyrene	**1050**	**2.16**	**0.59**	**Fast to node**
Triglyceride (fat)	**913**	**5.34**	**-0.23**	**To antinode**
RBC	**1099**	**3.31**	**0.39**	**To node**
WBC	**1019**	**4.00**	**0.17**	**Slow to node**
Water	**997**	**4.7**	**-**	**-**
Phys. Saline (0.9%)	**1005**	**4.5**	**0.05**	**Fluid interaction**
Skim milk	**1030**	**~4.2**	**0.14**	**Fluid interaction**
Whole blood	**1060**	**~3.7**	**0.27**	**Fluid interaction**
Blood plasma	**1025**	**~4.0**	**0.18**	**Fluid interaction**

Secondary acoustic radiation force

As mentioned earlier the acoustic wave scatters when it hits a particle. The scattered wave will then hit and interact with any other particle in close proximity. The resulting phenomenon of either particle attraction or repulsion is called the secondary acoustic radiation force (SRF, Eq. 18)[180] or Bjerknes force, named after Vilhelm Bjerknes who described it in a 1909 publication[181]. The first term in the SRF equation is angle dependent and describes the influence of the velocity field. Meanwhile, the second term is always attractive and describes force contribution of the pressure field. Thus the SRF works in the direction of the pressure field gradient and will cause particles to attract or repulse each other depending on the angle between the steepest pressure gradient direction and the particle-particle centre-line.

If a stream of particles is aligned along the gradient direction of the pressure field ($\theta = 0°$), those particles will be repulsed from each other (Fig. 20a). In the field of cytometry this repulsive interaction might in theory facilitate particle/cell-stream spacing to avoid counting double events. Conversely, a pressure field gradient that is perpendicular to the stream ($\theta = 90°$) will then cause those particles to attract each other (Fig. 20b). This attracting force is employed in acoustic trapping to capture particles that are too small to trap with the PRF by making clever use of the SRF from larger "seeding particles" that themselves has been captured using the PRF[69]. The fact that SRF forces scales heavily with increased particle size contributes to the success of this type of "seed" trapping.

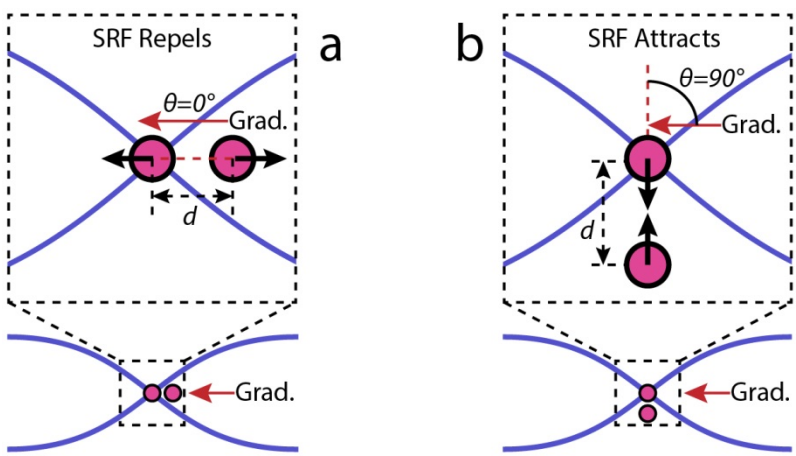

Figure 20, The secondary acoustic radiation force. Depending on the direction of the standing wave pressure field gradient, particles in close proximity (d small) to each other will either be repulsed ($\theta = 0°$, wave pressure field gradient parallel to the particle-particle centre line) (a) or attracted ($\theta = 90°$, gradient perpendicular to the particle-particle centre line) (b) when hit by the wave, which can be used to form tight clusters in standing wave trapping applications.

The SRF diminishes rapidly as particle-particle distance increases and thus it is not of great concern to most of the applications in this dissertation, where particle concentrations are relatively low, except in Paper 2 where it might have contributed to the chip clogging if

secondary forces between lipid particles helped to form the aggregates at the channel walls. It is also important to note that the SRF plays a role in acoustic manipulation of whole blood where the high haematocrit levels cause the blood cells to clump together and act as a "large particle" through hydrodynamic interactions which then disrupts normal separation[182]. The "large particle" phenomenon makes the WBC separation in Paper V harder to perform at high cell concentrations.

$$F_{sec} = 4\pi a^6 \left[\frac{(\rho_p - \rho_m)^2 (3\cos^2\theta - 1)}{6\rho_m d^4} v^2(x) - \frac{\omega^2 \rho_m (\kappa_p - \kappa_m)^2}{9d^2} p^2(x) \right]$$

Eq.* 18 *Secondary acoustic radiation force

$a = particle\ radius$

$\theta = angle\ between\ part. - part.\ centre\ line\ and\ direction\ of\ pres.\ field\ grad., fig.\ 20$

$d = particle - particle\ distance, fig.\ 20$

$\omega = angular\ frequency\ \frac{2\pi}{T}, T = period$

$v = velocity\ field\ (at\ position\ x, close\ to\ particle, v(x) \cong v(x+d))$

$p = pressure\ field\ (at\ position\ x, close\ to\ particle, p(x) \cong p(x+d)$

Streaming

In the historical notes on acoustics presented earlier it was explained that the field of cymatics allows for visualization of sound. The physical phenomenon that makes this visualization possible is actually acoustic streaming, which can be of great use as well as a hindrance in acoustofluidic systems. In 1831 Michael Faraday made some comments about the acoustic patterns that Hooke and Chladni had created experimentally in which he noted that the vibrating plate seemed to induce air circulation close to its surface, which could be visualized with sand or powder particles[183]. Dvorak made similar comments in 1876 on the Kundt-tube in which particles also seemed to circulate in air flow according to the acoustic pressure node patterns in the tube[184]. Lord Rayleigh explained both phenomena theoretically for the first time in 1884, hence the name "Rayleigh streaming" is used when dealing with these acoustically induced fluid circulations[171] (Fig. 21a). In 1932 Hermann Schlichting showed mathematical proof that the Rayleigh streams were in fact caused by fluid circulation within the boundary layer at the rigid wall[185]. These vortices circulate in a counter-wise direction to the Rayleigh-streams which they induce and are a result of shear stresses in the steep gradient of viscous dissipation of acoustic energy into the boundary layer which is caused by the fluid no-slip condition at channel top and bottom (Fig. 21b).

Schlichting-streaming is often called inner streaming while Rayleigh-streaming is called outer streaming or "bulk streaming" since they govern streams in the bulk of the fluid. On a Chladni-plate which can be seen as an open container the Schlichting-streaming do not create any steady Rayleigh-streaming because the fluid (air) outside the boundary layer flows freely. However, in a closed container like a microfluidic channel which typically has two parallel rigid walls located a half to a couple of wavelengths from each other, and an even smaller top-bottom dimension; the Schlichting-streams will induce Rayleigh-streaming. Suspended particles within these streams will then be subject to Stokes drag forces acting in the direction of the fluid circulation. In the case of a suspension where micron sized particles are acoustically translated into nodes, the Rayleigh-streams might then cause some of those particles to migrate toward the channel top and bottom and cause particle aggregation (Fig. 21a, streaming particle). Since the drag force scales with radius while PRF scales with volume, the bulk-circulation (Rayleigh-streaming) will actually govern particle movement in the channel for sufficiently small particles, making acoustic focusing impossible. In a half wavelength water filled channel actuated at 2 MHz the critical particle radius, at which bulk streaming negates acoustic focusing, is ~1.5 μm[186,187].

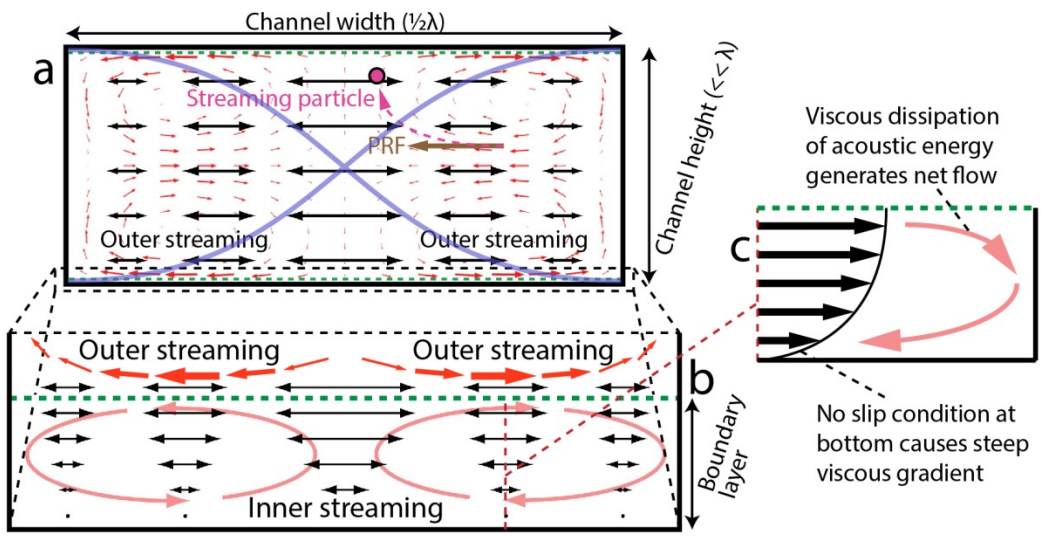

Figure 21, Inner (Schlichting) and outer (Rayleigh) boundary acoustic streaming. The large vortices in the bulk volume of a flow medium in an acoustofluidic system are caused by Rayleigh streams (a) These vortices may prevent separation of relatively small particles due to the vortice-induced Stokes drag forces which may counteract the PRF (see Fig. 7). The Rayleigh streams are generated by small but strong fluid vortices (Schlichting streams) in the boundary layer (b) which are caused by fluid shear stresses in the steep gradient of viscous dissipation of acoustic energy between free flowing fluid layers and the no-slip layer condition at the rigid channel boundaries (c). *Adapted from the dissertation "On microchannel acuostophoresis" with kind permission from Per Augustsson (a and b).*

In some applications the bulk streaming is used to rapidly mix very small fluid samples which would be hard to mix using macroscale tools[188]. This method has been commercialized by Beckman-Coulter to mix small samples using SAW (PlateBooster™). It should be noted that another type of streaming, called Eckart-streaming after Carl Eckart

who described it in 1948, is also generated by acoustic energy[189,190]. Eckart-streaming or "Quartz-wind" is induced by acoustic energy dissipation into the bulk of the fluid and does not rely on the nodal point patterns. However, this type of streaming does not apply to the system designs, channel dimensions and acoustic frequencies at which the experiments presented here were performed.

Modelling

In this dissertation modelling of the resonating channel cavities was performed throughout the development of the various acoustofluidic systems described. By constructing a model of the proposed channel cross section in a finite element software program (COMSOL Multiphysics®, was used for all simulations presented here) it is possible to acquire eigenmode solutions that show the frequencies at which acoustic standing waves will form in a given channel geometry. The procedure has shown itself to be accurate when comparing modelled systems to experimental results and with more accurate solutions, including PRF and both inner and outer streaming conditions, being presented recently as part of the increased interest in the acoustofluidic field and the technical leaps in computer processing power(Fig. 22)[150,176,187].

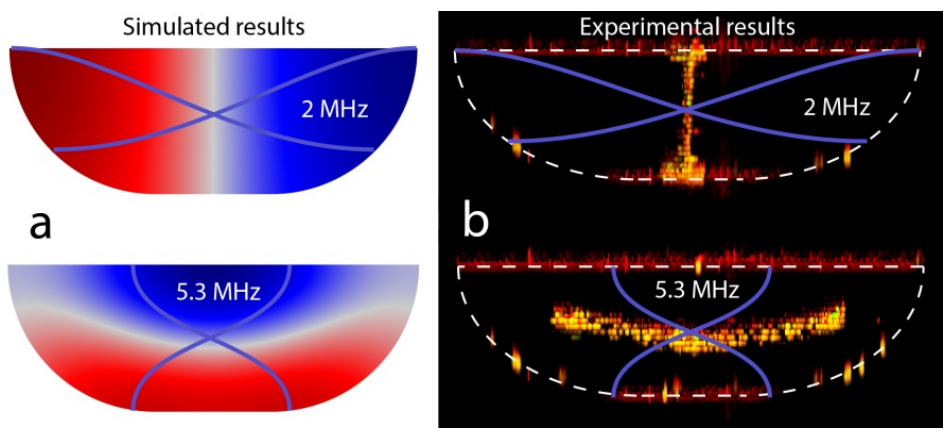

Figure 22, Comparisons between simulated and experimental results of particle focusing in a rounded wall glass acoustofluidic channel. By simulating the eigenmode of acoustofluidic channels it is possible to predict how acoustic field pressure nodes and antinodes will form at certain acoustic frequencies (a). In this dissertation these patterns have been confirmed with confocal microscopy images of focused particles in the system during operation (Paper IV)[67] (b). Rayleigh-stream induced aggregation of particles at the channel top and bottom are visible in the top right figure.

Multiple wavelength acoustics

While most presented acoustofluidic systems make use of half-wavelength resonating geometries it is also possible to increase the number of pressure nodes and antinodes to better suit the intended application. This can either be done by increasing the actuating

frequency to achieve a higher harmonic resonance or by increasing the dimension of the resonating geometry to fit multiple half-wavelengths at the fundamental frequency (Fig. 23)[48,63,66,191].The governing physics are the same for multiple node and single node systems but the PRF will be slightly weaker in multiple node systems due to energy dissipation. However, in most applications this loss of acoustic efficiency can be circumvented by increasing acoustic power input. The additional nodes or antinodes can also be employed as "acoustic barriers" to prevent either positive or negative acoustic contrast force (ACF)-particles from reaching sheath flows or, in the case of negative-ACF, even the channel wall. The acoustic barrier approach is used to prevent fat globules from clogging the separation chip in Paper I (Fig. 23b).

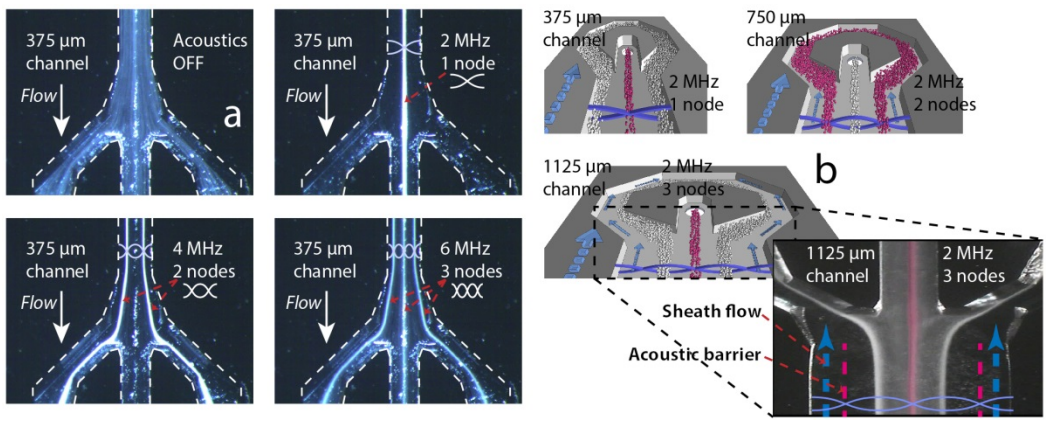

Figure 23, Multiple wavelength resonating channels. By increasing the actuation frequency to a harmonic of the fundamental resonance frequency it is possible to create multiple pressure nodes in a channel (a). By increasing the resonating geometry to a multiple of the original dimension it is possible to achieve multiple pressure nodes at the original frequency (b). In some applications, the increased number of pressure antinodes can be used to achieve binary separation with acoustic barriers that prevent particles from entering sheath flows and reaching the channel walls (b, lower right).

Two-dimensional resonance acoustics

In addition to conventional resonant geometries that support standing waves in one dimension, it is also possible to combine standing waves in two dimensions simultaneously. This can be done by designing a resonant geometry where the second resonant dimension is identical to, or a multiple of, the first which allows two-dimensional actuation using one frequency e.g., a round or square channel in the first case and a rectangular channel with integer aspect ratio in the second case (Fig. 24a)[46,47,57,149,151,186,192]. It is also possible to actuate a less regular resonant geometry with two separate frequencies which are individually adjusted to induce standing waves in the two dimensions respectively (Fig. 24b and c)[56,67,154]. The net PRF from the combined waves in a square channel will result in a pressure node point in the centre of the cross section (Fig. 24a). It is possible to combine single or multiple half-wavelength resonances in each dimension depending on the application. Successful two-dimensional focusing has been shown in round capillaries[193],

rectangular channels[153,154], square channels[186] and semi rectangular channels with rounded walls (Fig. 24c)[67]. In some applications the force from two standing waves can also be used to trap particles in precise positions. In papers III and IV, two-dimensional focusing is used to precisely focus a stream of particles in order to improve microchip cytometers.

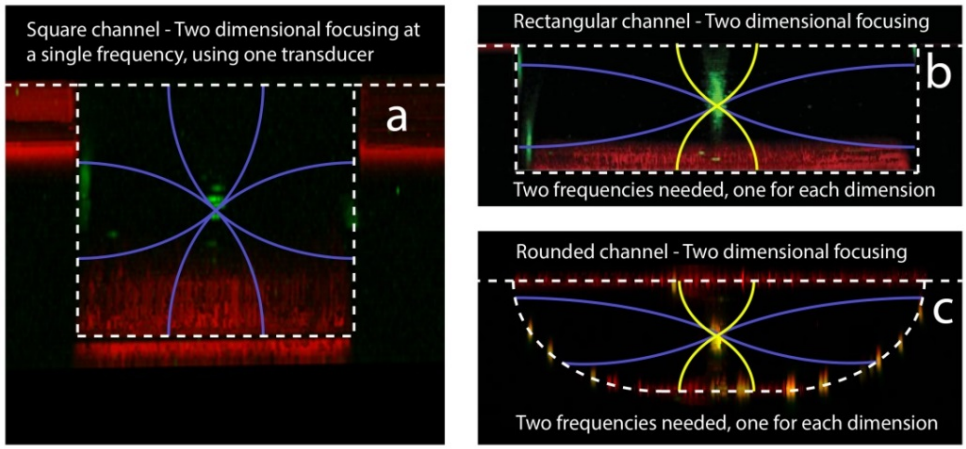

Figure 24, Confocal images of two-dimensional resonance focusing of fluorescent beads. In a square channel it is possible to achieve 2D-focusing of beads using one frequency that matches the resonance criterion of both dimensions (a). In a rectangular geometry where the dimensions are not multiples of each other, two frequencies, each individually tuned to match one of the dimensions, are used to achieve 2D-focusing (b). 2D-focusing can also be achieved in round capillaries or semi-rounded rectangular geometries (c).

Microfabrication

Materials

There are several desired material properties to take into account when designing acoustofluidic systems for cell or particle manipulation. Among them is the need for a simple straightforward fabrication process which can produce multiple structures with high precision and reproducibility. Furthermore, the material should be bio-compatible, and have good acoustic properties, especially in combination with frequently used suspension media e.g., water or blood plasma. If possible, the material should also allow cheap mass production, lab-on-a-chip integration, optical inspection and easy connectivity to fluidic networks. In the following section three materials that more or less fit those requirements are presented: silicon, glass and PDMS.

Silicon microfabrication

Silicon is 2nd most abundant element in the earth's crust (28 wt%) which makes it easy to attain compared to many of the other materials used in the integrated circuit (IC)/MEMS industry. Because of its semiconducting abilities and straightforward microfabrication process it has become very popular in industrial applications ever since the IC-revolution in the 1960s. Today the microfluidic science community benefits from the 50 years of research and advances in silicon microfabrication carried out in the IC/MEMS industry which also helped the development of microfabrication techniques in other materials.

The crystalline properties of silicone allow a variety of fabrication methods to be used in the design and manufacturing of intricate microfluidic channels for acoustofluidic systems. Silicon is bio-compatible and permits acoustic wave propagation with little dampening. Furthermore, the acoustic impedance of silicon is very different from that of water or complex biofluids like blood or milk which allows efficient generation of acoustic standing waves due to the high reflection coefficient, also supported by the straight parallel channel walls that can be produced by anisotropic wet etching along crystal directions. Additionally, the thermal expansion coefficient of silicon is well matched to borosilicate glass (e.g., Pyrex™ or Borofloat™) which makes it possible to anodically bond glass lids on top of the microfluidic channels to facilitate optical inspection during experiments.

The most common methods used to create microfluidic structures on silicon can be described as either dry or wet etching techniques. In common for these techniques is the requirement of a mask which protects the silicon substrate in certain areas while others are

removed by etching to form the structure. The masking method is often the limiting factor that decides how detailed and precise the dimensions of the finished structure can be.

Dry etching (reactive ion etching, RIE) is performed by ionizing a gas with an oscillating electric field which produces a plasma that chemically reacts with the silicon substrate. RIE is typically isotropic in nature, which limits its use in acoustofluidic system fabrication, but it is possible to achieve highly anisotropic etching by instead using deep reactive ion etching (DRIE). In DRIE, etching is performed in cycles and after each cycle a chemically inert material is deposited on the silicon substrate to prevent lateral etching while allowing continued depth etching along the oscillating electric field gradient. The wet etching method has been used throughout this dissertation and is explained in more detail below.

Wet etching

All of the channel structures in this dissertation were made using wet etching. The procedure of manufacturing a silicon microfluidic chip with a glass lid such as those presented in paper I-III and V can be described in 10 steps (also visualized in figure 26):

1. Choose the type of silicon substrate (crystal plane orientation) to be used

When manufacturing silicon substrates for microfabrication the producers cut the bulk silicon crystal into wafers along different planes in relation to the crystal structure. These wafers are identified by their "Miller indices" using the notation (hkl) when dealing with the bounding planes perpendicular to the wafer surface and [hkl] when dealing with crystal directions. Directions [100], [010] and [001] are all part of the <100> group of directions while the group notation for the (100), (010) and (001) planes would be {100} (Fig. 25a). Once the silicon wafers are cut they are marked with "orientation flats", small flat segments on the wafer edge that help to align the substrate in the masking/fabrication process (Fig. 25b). Typically a (100) wafer would be chosen for most applications (including papers I and II) since it allows anisotropic wet etching of a vertical wall rectangular channel (Fig. 25d). In paper V a (110) wafer is used to achieve a square channel with anisotropic etching.

2. Wafer oxidation, silicon dioxide growth

Once a suitable substrate has been chosen the wafer is oxidized in an oven. By heating the wafer to ~1000° C in a flow of oxygen or steam mixed with another gas (N_2) it is possible to grow a layer of silicon dioxide (SiO_2) on the wafer surface. The SiO_2-layer is later used to protect certain surface areas from the etchant according to the photolithographic mask.

3. Mask design

A photolithographic mask is created in order to define which areas of the wafer to etch. This is often done by using computer aided design (CAD) software to create a drawing of the microfluidic structure. The drawing has to account for which type of photoresist that will be used, which crystal orientation the wafer has and also compensate for differences in etch ratio. Markings that allow mask alignment to the wafer orientation flat are also included. The drawing is then transferred to a mask substrate e.g., a glass wafer with a chromium layer which is exposed to a laser and then developed.

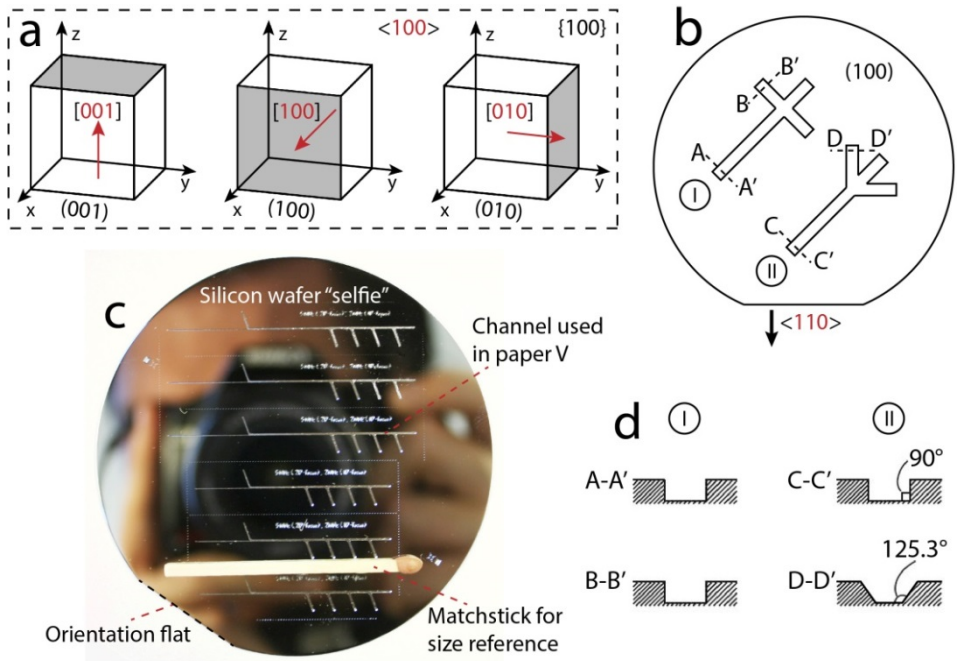

Figure 25, Crystal planes and results of wet etching on a (100) silicon wafer. A (100) wafer has a surface plane that is perpendicular to the [100] crystal direction (a). By aligning the channels in a 45 degree angle to the <110> orientation flat it is possible to achieve channels with straight parallel walls (b-I and d-I). The optical qualities of silicon wafers might even attract young persons from the "selfie" generation to science (c). If a channel structure is aligned perpendicular or parallel to the orientation flat in (b) the etching would result in parallel walls with a 125.3 degree angle to the channel bottom due to the {111} etch stop planes (b-II and d-II). *Adapted with permission: Nilsson[45] (b and d).*

4. Enabling photolithography with photoresist

Once the mask is done it can be used to transfer the structure design to the silicon wafer by only allowing certain areas of a photoresist substance to be exposed by UV-light (photolithography literally means to use light to write in stone (silicon)). There are two types of photoresist, positive and negative. Positive photoresists become soluble when exposed to UV-light while negative resists become insoluble when exposed. The photoresist layer is added, typically by spin-coating, on top of the SiO_2-layer and after UV-light exposure the wafer is baked in an oven to further strengthen the insoluble areas. After baking, the photoresist is developed using a solvent which dissolves the soluble photoresist and leaves a pattern of bared SiO_2 identical to the mask if positive photoresist was used while the use of negative resist will bare an inverse SiO_2 area compared to the mask pattern.

5. SiO_2 removal by etching

The part of the SiO_2-layer that was laid bare by the photoresist development can then be removed by immersing the wafer in hydrofluoric acid (HF) which acts as an oxide etchant. When the exposed oxide has been removed by the HF, the etching process will stop since HF does not etch pure silicon.

6. Stripping of photoresist

After the oxide etching is complete the remaining photoresist is removed with acetone or other solvents depending on the resist type and how long and at what temperature it was baked. The result is a SiO_2-layer with patterns of exposed pure silicon according to the type of mask that was used.

7. Etching of silicon

Once the wafer is cleaned from photoresist residue and other impurities it is time to etch the pure silicon that was laid bare when the SiO_2-layer was removed. The silicon etching in this dissertation was done using potassium hydroxide (KOH). The wafer is immersed in a KOH bath which is then lowered into a heated water tank to increase the etching rate. To speed up etching even more and maintain uniform etching rates in all directions the wafer is rotated and subjected to ultrasound agitation. The wafer is inspected periodically during the etching process and once the desired etch depth and/or width has been achieved the wafer is removed from the bath, the remaining SiO_2-layer is removed with HF and the photolithography step is finished, having resulted in an etched structure in the silicon wafer which can then be post-processed (or undergo a repeat process to add opposite-side structures, typically fluidic access holes).

8. Dicing the wafer into individual channels

Once the wafer is cleaned it is attached to an adhesive plastic film which prevents the brittle substrate from breaking into pieces during dicing. The dicing saw does not cut through the whole wafer, instead leaving about 0.2 mm substrate in order to maintain the alignment of individual channels on the wafer during dicing of multiple channels (which is normally the case). Each individual channel is then carefully broken off along the cuts.

9. Anodic bonding of the glass lid to the silicon substrate

Once an individual channel has been diced, a borosilicate glass lid is attached to it through anodic bonding. The bonding is performed by heating the substrates to about 500° C while pushing the glass down on the silicon with a spring loaded cathode and applying a 1000 V bias voltage. The thermal and electric energy then causes covalent Si-O and Si-Si bonds to form at the glass-silicon contact surface which seals the two substrates together.

10. Facilitation of fluidic network access to the chip

Depending on the design of the chip, the glass will either have holes drilled through it prior to bonding or holes will be etched into the channel from the other side of the silicon wafer. These holes are used to facilitate access to the fluidic network by attaching various fluidic connectors. In papers I-III and V fluidic access was facilitated by gluing soft silicone tubing to the holes which acted as sealants for the Teflon™ tubing that connected the chip to the syringe pumps and other components in the fluidic network. Once fluidic access is achieved the chip is ready for use and acoustic actuation can be performed using numerous methods depending on the application.

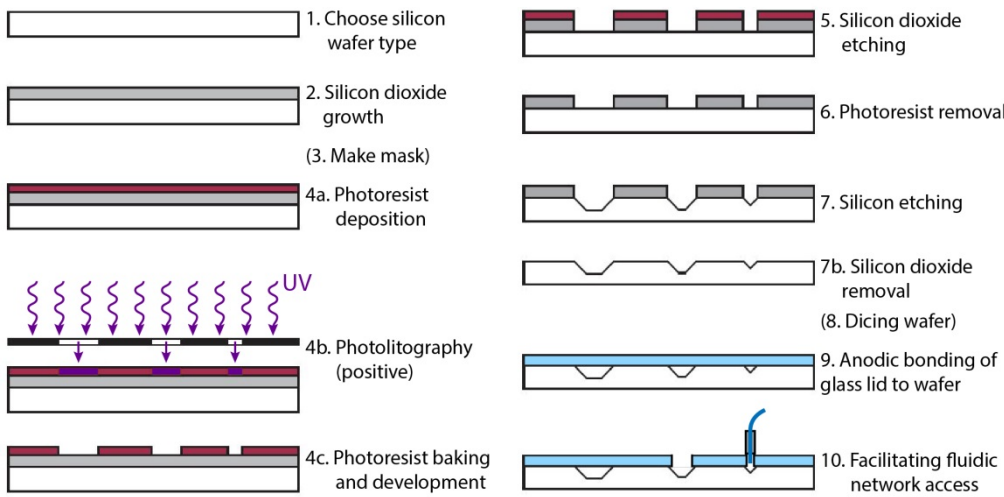

Figure 26, Microfabrication steps involved in positive resist wet etching of a (100) silicon wafer to produce a microfluidic chip. Microfabrication of acoustofluidic channels often follows these steps: A CAD-drawing is used to create a photolithography mask. The mask is then used to expose certain parts of a photoresist layer to UV-light in order to remove specific areas of a silicon dioxide layer which has been grown on a silicon substrate. The remaining oxide layer is then used as a mask for the pure silicon etching. Once etching is complete the remaining oxide is removed and the substrate is diced into individual channels, which have glass lids anodically bonded to them. *Adapted from the dissertation "Acoustic standing wave manipulation of particles and cells in microfluidic chips" with kind permission from Andreas Lenshof.*

Glass microfabrication

Borosilicate glass shares many of the desired properties with silicon when it comes to choosing materials for acoustofluidic chip microfabrication. It is a bio-compatible material that allows easy and cheap manufacturing of detailed microfluidic structures using wet or dry etching[194–199]. While not having quite as good acoustic properties as silicon, glass has been shown to achieve similar results in acoustofluidic applications[67,200]. Due to the amorphous nature of glass it is only possible to perform isotropic wet etching which somewhat limits the number of applications. Typical channels will have a flat bottom with rounded walls, like the one presented in paper IV. However, by using DRIE it is possible to obtain near-straight walls in almost square or rectangular channels[198,199]. The main advantages of using glass is the ability to design curved channels, due to the isotropic properties, and the translucent nature of the material which permits additional optical detection methods to be used compared to silicon substrate channels (Fig. 27). Another area of interest is the use of cheap mass fabricated glass capillaries in acoustofluidic systems that focus or trap cells and particles which might lead to low cost LOC and POC systems[54]. A reliable method that allows capillaries to be connected to a microfluidic network through a polymer interface was recently presented[201].

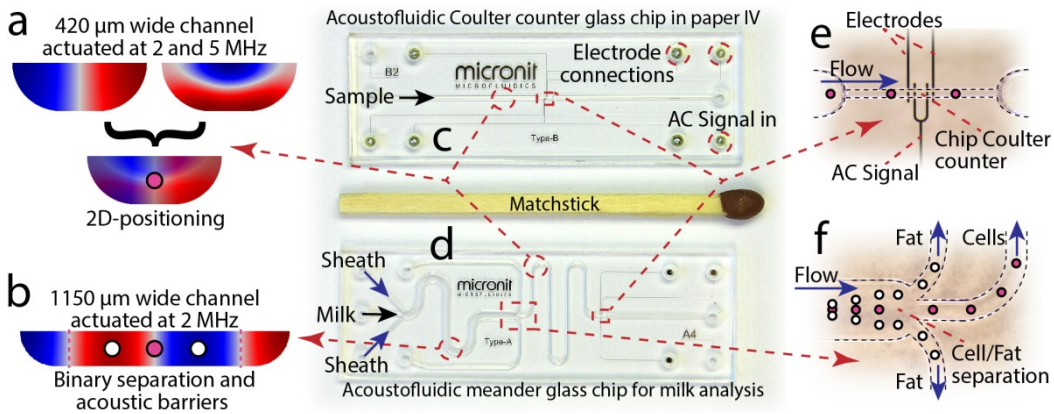

Figure 27, Acoustofluidic glass chips with integrated chip Coulter counters. The acoustic properties of glass are similar to silicon and with the help of rounded wall eigenmode simulations it is possible to adjust the channel dimensions to achieve efficient single (a, upper channels), multiple (b) and two-dimensional (a, lower channel) standing waves at commonly used frequencies. Using borosilicate glass also makes it possible to integrate additional functionality like on chip Coulter counters (c-e) or rounded acoustofluidic channels for binary separation (d and e) with fewer restrictions on the overall chip layout compared to silicon.

Polymers and elastomers (PDMS)

Even though the acoustofluidic systems presented in papers I-V are all based on either silicon or glass substrates, it should be noted that many general microfluidic applications and surface acoustic wave applications can be fabricated in "soft" materials as well. Numerous microfluidic applications and small structures have been fabricated in polymers or elastomers either by using soft lithography, moulds, embossing or imprinting techniques[202–206]. Among these materials poly(dimethylsiloxane) (PDMS) has gained the most attention[9,207]. The benefits of using PDMS include bio-compatibility[208] and the possibility to change the channel surface chemistry for delicate biomedical applications or to prevent cellular materials from adhering, sometimes an issue with hard materials that require high temperature bonding. It is also possible to vary the Young's modulus (material stiffness) of the material according to the application[209] or to include moving parts in the microfluidic system with valves that can close without additional components. Furthermore PDMS is a cheap material to use, costing about ~50 times less than silicon for the same bulk volume while also requiring less stringent microfabrication conditions compared to silicon or glass which eliminates the need for a clean room. Furthermore, most PDMS structures are translucent which allows optical inspection. The drawbacks of using PDMS include the risk of leakage at high fluid pressure settings, the gas permeability which might cause unwanted bubble formation in the system, unwanted ad- or absorption of hydrophobic compounds into the bulk material and the batch-fabrication process which results in slow chip turnover. Most importantly, for the applications presented in this dissertation, PDMS suffers from bad acoustic properties, which prevents acoustic wave propagation and the formation of standing waves, due to attenuation and having an acoustic impedance similar to that of water. On the other hand, the gas permeability also

allows degassing of samples by adding a low-vacuum chamber to the outside of the channel structure and the versatile bonding options allow SAW-actuation with variable acoustic pressure node positions and might also lead to novel applications for BAW silicon systems by facilitating changed acoustic impedance conditions at the channel walls (Fig. 28)[156–158,161,168,210–212].

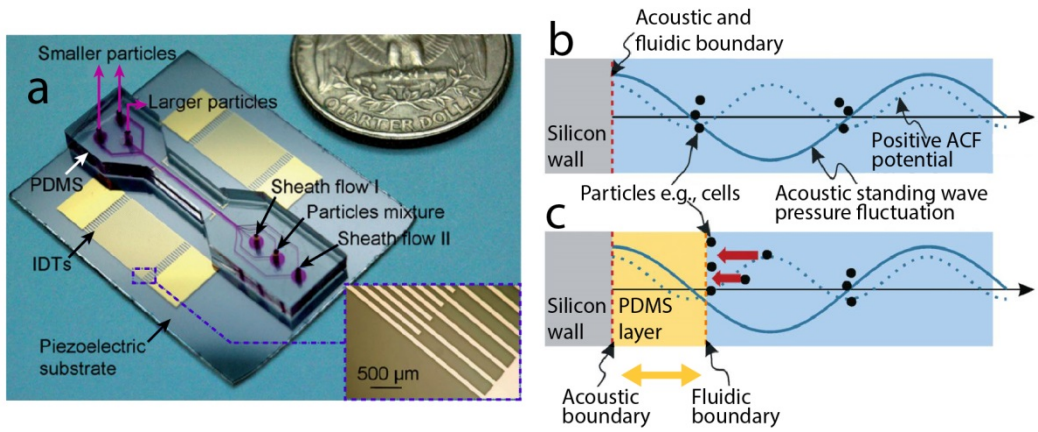

Figure 28, PDMS used in acoustofluidic chips. Due to intrinsic acoustic properties that prevent BAW-propagation and standing waves, PDMS is traditionally used in combination with SAW-actuation, often by using counter propagating interdigital transducers (IDTs) to generate SSAWs, enabling separation, trapping or focusing of particles (a). Recent reports indicate that there may be other applications for PDMS in BAW acoustofluidic channels as well, including the ability to use a layer of PDMS to separate the acoustic and fluidic boundaries of the channel which facilitates positioning of a pressure node at the fluidic boundary (b vs. c). *Adapted with permission: Shi[158](a) and Leibacher[212](b and c).*

Piezoelectricity and Transducers

Piezoelectricity

In order to actuate acoustofluidic systems it is necessary to induce material vibrations. This is most often done with a piezoelectric transducer. The effect known as piezoelectricity (derived from the Greek word for squeeze or press, *piezein)* was discovered by brothers Pierre and Jacques Curie in 1880 and describes the ability of a material to generate an electric field potential gradient (voltage) when subject to mechanical stress (Fig. 29). The gradient is the result of electric displacement along the direction of the applied stress and can be described as the linear electromechanical interaction between the mechanical and the electrical state in a crystalline material. Interestingly the effect is reversible, meaning applied voltage leads to material deformation. These properties make piezoelectric materials ideal as sensors (indicating movement or pressure changes with changes in electric potential), as well as acoustic transducers that can be forced to oscillate at precise frequencies by using function generators to apply alternating currents across them. There are many piezoelectric

materials and common examples include quartz and lead zirconate titanate (PZT). During fabrication of PZT, which is a crystalline ceramic material that is heated and then polarized by a strong electric field to become piezoelectric (Fig. 29a), the doping process can be adjusted to produce transducers with different properties according to the intended application. Typically a high piezoelectric constant (deformation per applied electric unit) comes at the expense of losses in the material due to high internal friction.

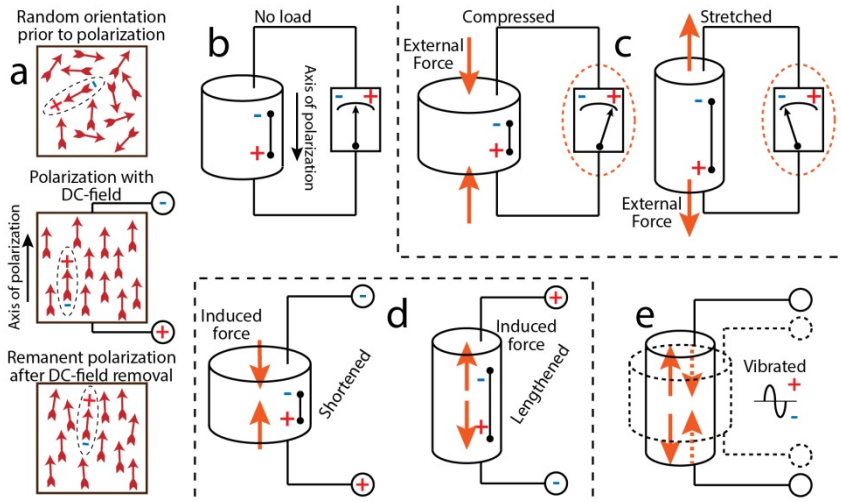

Figure 29, The piezoelectric effect and its applications. PZT is heated above the "Curie-temperature" during fabrication which allows the dipolar molecules in the material to align along a strong applied electric field gradient (a). The electric field is kept active during cooling to prevent the crystal molecules to randomly realign themselves. The remanent polarization (remaining alignment of molecules) results in a substrate which has a high piezoelectric constant along the axis of polarization (b) and can be used as a sensor (c) or actuator (d, e) depending on the application. By applying high frequency AC-fields across it the piezoelectric material can be used to produce ultrasound (e).

Bulk transducers

In all papers presented here, bulk transducers made from PZT-4 (pz26) are used to actuate the acoustofluidic systems. PZT-4 is a hard grade (acceptor doped) piezoelectric material that allows continuous operation with little material loss. By precise dicing it is possible to control the thickness of the PZT-crystal which results in a transducer that resonate at predetermined frequencies. A silver layer is typically deposited on each side of the crystal to achieve uniform actuation. By attaching the transducer to the acoustofluidic chip it is then possible to induce longitudinal acoustic waves in the bulk of the chip by applying an AC-field across the transducer (Fig. 30a). The method can produce strong pressure fields (> 1MPa) inside the chip which facilitates efficient particle manipulation.

Interdigital transducers (IDTs)

An alternative to the bulk transducer is the interdigital transducer (IDT), first presented by White and Voltmer[213] in 1965. They fabricated thin film IDTs on the surface of a piezoelectric substrate to act as electric input and output ports for use in electronic signal processing. The application of an AC-voltage on the input transducer generated a surface acoustic wave (SAW) which was received by the output IDT and converted back to an AC-voltage. Thus the device could be regarded as a delay line (delayed by the amount of time it takes for SAW generation, propagation and reconversion) or as a band-pass filter since only certain wavelengths (frequencies) will fit the pitch (digit-digit distance) of the IDTs and be amplified during generation as well as reconversion. Today IDTs are used to create high frequency SAWs (>10 MHz) on piezoelectric materials to allow acoustic actuation of acoustofluidic systems made from hard as well as soft materials (Fig. 30b). The benefits of using SAW are the high frequency, which allows small particles to be manipulated, and the possibility to control the wave propagation along certain directions, which allows arbitrary positions of multiple pressure nodes within an acoustically actuated chamber through standing surface acoustic wave formation (SSAW) when using multiple IDTs (Fig. 30c). The drawback is the inability to actuate bulk volumes with high efficiency which hampers particle manipulation (the SAW only reaches about one wavelength into the piezoelectric material since it is a combination of transverse (rapidly damped) and longitudinal wave motion)[166].

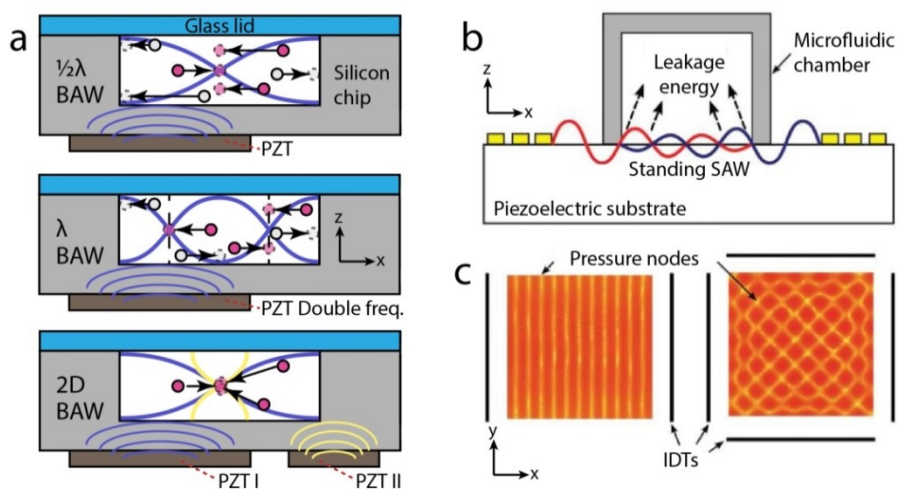

Figure 30, BAW and SAW Piezoelectric transducers. BAW-actuation of the systems presented in this dissertation is done by attaching a PZT-transducer in proximity to the resonance chamber (microfluidic channel) and then actuating the PZT at a frequency that fit the resonance condition for the chamber given the medium within. The actuation causes longitudinal waves to propagate through the chip substrate into the medium where they are reflected between the channel boundaries to cause standing waves (a). SAW-actuation uses IDTs to generate a combined transverse and longitudinal motion wave (Rayleigh-wave) along the surface of a substrate on top of which a fluid chamber or droplet is placed (c). The SAW then leaks energy into the suspension in the chamber or the droplet which allows particle manipulation and/or fluid streaming depending on the IDT positioning and whether or not SSAWs is generated (d). *Adapted with permission: Lin*[214]*(b and c).*

Biofluids and cells

Handling of complex biofluids

In order to design adequate acoustofluidic systems it is important to understand the properties and behaviour of the biofluids and cells that are most frequently handled in biomedical applications. In the following section some important properties of blood and milk will be discussed together with aspects to take into consideration when dealing with bacteria. Due to the complexity of these biofluids the numerical values and quantities of the biofluid and cell properties e.g., cell size, density and concentration as well as biofluid sound velocities or protein concentrations that are stated here varies in literature and should be seen as approximate values at 20° C.

Blood

Blood is the most frequently used biofluid in biomedical applications and of great importance when it comes to health diagnostics and pathologic analysis[215–217]. There are numerous properties of blood that complicates acoustofluidic handling. The high cell volume content (haematocrit, HCT) in blood leads to short cell-cell distances which in turn results in high secondary acoustic radiation forces (SRF) and hydrodynamic coupling between cells. The effect of these particle interactions is a risk of sample clogging, erroneous sorting or fluid capture in large cell clusters. The varying size (~5-15 μm Ø for RBCs and WBCs and ~2 μm Ø for platelets), density (~1.05-1.15 g/ml) and shape (discs or spheres) of blood components also pose a challenge. RBCs are dense disc shaped cells while WBCs are large, spherical and less dense (the disc shape of the RBCs does, however, offer the possibility to orientate them using acoustic forces[218]). In theory this suggests that separation should be simple, but the size overlap, nucleus granularity and density variation of different WBC subpopulations make it difficult to separate WBCs from RBCs or to fractionate WBCs into subpopulations (paper V however presents a method to deal with these issues and separate granulocytes from lymphocytes with high purity and recovery). Furthermore, the high HCT and protein levels in blood lead to variations in the acoustic properties of the suspension itself[219,220]. At normal 40% HCT the sound velocity in blood is 1590 m/s but it decreases to 1540 m/s at 10% HCT. Similarly the sound velocity in plasma decreases when protein concentration is reduced. Also, the sound velocity increases with temperature by about 2 m/s $°C^{-1}$. Thus, the biofluid properties at the inlet might differ from those at the outlet due to cell removal, heating or changes in protein content, which has to be taken into account when designing acoustofluidic systems.

Milk

The acoustic properties of milk make it a good candidate for acoustofluidic treatment. Typically, the handling of raw milk would lead to clogging in acoustic separation systems. This is due to the fact that suspended fat globules (lipid micelles mainly composed of triglycerides, ~1-8 μm in size) in milk has a negative acoustic contrast factor (ACF) which leads to accumulation of fat in the pressure antinodes along the sides of conventional half wavelength resonating acoustic channels. However, the negative ACF also has some benefits since it allows binary separation of the fat from the positive ACF somatic cells (7-10 μm Ø) that are found in raw milk during certain pathological conditions e.g., mastitis. In paper I and II the development of a system for lipid depletion and cell isolation is described. The system uses a multiple wavelength resonating channel to perform binary separation of milk components without clogging to allow cell counting and analysis of fat and protein content. It should be noted that binary separation of milk components is unique to acoustic manipulation techniques. Analogous to blood, suspended particle and protein (casein) content in milk affects the sound velocity (varying from ~1550 to 1520 m/s as concentration decreases). This could possibly be used to detect illegal melamine adulteration of milk, adding to the list of methods in which ultrasound is used in food analysis or processing[221–224]. Interestingly the casein micelles are about 0.3 μm in size which indicates that they might be possible to separate or concentrate using a sufficiently high ultrasonic frequency (>15 MHz)[186].

Bacteria

In addition to the somatic cells found in blood and milk, the bacterial content in different biofluids, foodstuffs and water is also of great interest in biomedical applications in order to detect contamination or pathologic events like sepsis or mastitis[225–230]. The volume of a single bacterium is typically less than one tenth of the volume of a somatic cell (0.5 – 5 μm Ø or length) and vary in shape (cocci are spherical, coccobacilli ovoid and bacilli are rod-shaped)[231–233]. The small sizes makes it hard to manipulate bacteria in acoustofluidic systems since the Stokes drag dominates the PRF at small particle sizes at standard frequencies in the range of 1-5 MHz[234]. However, by increasing the frequency of the ultrasound or by making clever use of secondary effects like fluid streaming or particle-particle interaction it is still possible to sort, position or capture bacterial content for subsequent analysis or culturing[69,186,235–238]. Since the density of most bacteria is slightly higher (*Escherichia coli* 1.08 g/ml and *Bacillus subtilis* 1.22 g/ml) than that of somatic cells, it might be possible to achieve binary separation using medium density adjustments[152].

Acoustofluidic unit operations and application areas

Acoustophoresis – A versatile platform

Acoustophoresis has already been introduced in the "Particle manipulation methods"-section. However, since this acoustic manipulation method is quite versatile, and forms the basis for papers I-V, this section aims to provide a more detailed introduction to the various unit operations and applications available in the acoustofluidic "toolbox". BAW system actuation is presumed throughout the section but it should be noted that SAW-actuation might also be possible in some cases, although with possible negative impact on sample throughput, force amplitudes or integration. A very comprehensive presentation of the current state of the acoustofluidic field including theory, unit operations and applications is presented in the Lab on a Chip tutorial series "Acoustofluidics"[239].

Separation

The basic unit operation of acoustofluidic systems is the translation of suspended particles towards the pressure nodes or antinodes of a standing wave in an acoustically resonant flow channel. By clever design of the system, particles with same or opposite sign ACF can be separated.

Free flow acoustophoresis

By adjusting the sample flow and acoustic force amplitude of the system it is possible to separate particles with same sign ACF according to size, density and/or compressibility, as exemplified in the fractionation of WBCs, presented in paper V. The separation is performed by allowing particles to travel partial distances towards their target node or antinode according to the PRF amplitude, which depends on particle size, density and compressibility. Thus different particles end up in different lateral locations (perpendicular to the direction of flow) of the channel cross section, corresponding to different fluid fractions, which can then be extracted through two or more downstream target outlets. The method is called free flow acoustophoresis (FFA) and has been shown to separate various cells and artificial particles, including blood components[68,152], tumour cells[149,240,241],

polystyrene beads[152,242] and magnetic particles[243], with the latter allowing additional applications through surface chemistry based separation.

Binary separation

FFA separates particles with same sign ACF. However, it is also possible to perform binary separation of particles with different sign ACF. This allows separation of e.g., red blood cells and adipose tissue cells in post-surgery shed blood[44], somatic cells and fat globules in raw milk[66] or targeted separation of cells according to surface chemistry based attachment of opposite sign ACF particles[244,245]. Furthermore, the theoretical purity of binary separation is higher than that of FFA since the binary separation efficiency scales with applied acoustic force and is limited only by maximum system power output or heating issues at extreme power settings (which can be controlled with active cooling). An issue with binary separation is the tendency of negative ACF particles to form aggregates along the side walls of conventional half wavelength channels. This problem was solved in paper I and II, through the use of multiple node geometries, sheath flows and "acoustic barriers"[48,66]. The ability to perform these types of continuous binary separations in homogeneous media or complex biofluids is one of the benefits of using the acoustofluidic platform in comparison to other particle manipulation techniques.

Focusing

The basic translational mechanic of acoustofluidic systems can also be used to focus particles. Instead of separating the particles by their tendency to travel towards nodes or antinodes at different velocity, the particles are allowed to reach their target node/antinode which confines them in a more or less well defined fluid fraction. Focusing can be used to concentrate or precisely position particles and cells for subsequent analysis.

Concentration

The ability to rapidly concentrate samples with minimal manual labour is of great value to the biomedical industry. By concentrating suspended particles in acoustofluidic systems it might be possible to replace centrifuges in many existing protocols and allow gentle concentration of cells or to concentrate and detect rare particles like bacteria in drinking water. The concentration is done by focusing cells or particles to a well-defined fluid fraction and then extracting said fraction in a way similar to FFA. Compared to FFA, where particles might not be allowed to be tightly confined in the node/antinode, a concentration channel allows the PRF (and possibly even the SRF) to confine them to a very small fraction of the fluid. Conventional ~2 MHz half wavelength systems have difficulties with sub-micron particles, but two-dimensional focusing of 0.5 μm particles was recently reported using 3-5 MHz frequencies[154,186]. The concentration method explained here should

not be confused with the macro system concentration/filtration method which uses ultrasound to aggregate and sediment particles and cells[51,191,238].

Two-dimensional positioning

Analogous to the concentration focusing that was recently performed in order to two-dimensionally (2D) focus sub-micron particles, the same method has been used to precisely position larger particles and cells in order to improve various detection methods or sorting techniques. The method uses one or several transducers to actuate the acoustofluidic channel in multiple dimensions, thus focusing particles into a very well defined position in the cross section of the channel which allows very good spatial and temporal control of suspended particles in laminar flow[46,47,57,153]. The method has shown itself to be very useful in flow cytometry and particle sorting and even resulted in a commercial product (the Attune™ flow cytometer)[149,193,243,246]. Paper III presents a fluorescence activated sorting system that utilizes 2D-positioning to achieve higher sorting capabilities in a chip based acoustic FACS[56], paper IV describes how a 2D-positioning channel greatly improves the sensitivity of a Coulter counter on-a-chip[67] and paper V improves the sorting purity of an FFA system by pre-positioning particles prior to separation. Pressure nodes/antinodes are assumed throughout the section.

Particle switching

Due to the high particle translation velocities and the various media that can be used in acoustofluidic systems, acoustic translation of particles can also be used in applications where either rapid switching or multiple buffer media are necessary.

Cell sorting

The maximum experimental force on particle in which translation has been performed exceeds 100 pN. This amount of force will translate a 10 μm particle at a velocity of more than 1 mm/s which opens up the possibility for rapid sorting of particles by switching them into different target outlets[57]. In 2007 a fluorescence activated sorting system was presented[192] and recently an improved system was published which can sort >100 events per second with >75% purity and >90% recovery[56]. The gentle and continuous nature of acoustofluidic switching allows for integrated sorting of particles in LOC systems.

Buffer exchange

Rapid or slow translation of particles can also be performed across different suspension media interfaces. The method can either act as a simple buffer exchange system e.g., to wash

away labelling agents with minimal manual labour involved[59,60,247] or as a way to allow precise temporal control of multi-step chemical reactions by sequential translation of particles or cells into several different buffers e.g., to perform on-chip phage display selection or elution[61]. The method is also able to separate particles at the medium interfaces through clever use of varying PRF for each population given a certain flow medium[62,243,248].

Trapping

By adjusting the sample flow rate and acoustic power it is possible to design systems where the PRF dominates the Stokes drag force and gravity, which results in particle retention or trapping in nodes or antinodes. Early applications included retention, manipulation or filtration of particles[50–52]. Current methods include trapping in perfused systems where acoustic transducers are carefully positioned and used to generate localized acoustic fields that are strong enough to capture particles at these positions. The resulting "trapping sites" allow non-contact cultivation and exposure of cells and particles to different buffers for complex online bioassays[53–55,249] e.g., to capture, enrich, and wash bacteria directly from crude blood cultures[237]. Recently the method has been shown to trap sub-micron (110 nm) particles and bacteria by using large (~10 μm) "seed" particles to generate SRF particle-particle interactions that retain the smaller particles[69]. Flow free systems with single[57] or multiple acoustically resonant "wells"[250,251] has also been used to capture particles in arrays e.g., to observe cell-cell interaction of natural killer cells[252].

Orientation

The acoustic field gradient can also be used to perform shape-dependent manipulation of nonspherical particles. Since particles strive to minimize their exposure to the acoustic field according to the principle of minimum total potential energy, they will align according to the strongest acoustic field gradient. A system which utilizes this phenomenon to arbitrarily orientate RBCs in a flow channel was recently presented[218]. In theory the method could be beneficial to cytometry e.g., by creating uniform incident light beam conditions in flow cytometers for better subpopulation discrimination[253] or by allowing rapid optical analysis of abnormal cell sizes and shapes for rapid identification of e.g., *Plasmodium falciparum* infested RBCs in malaria patients either by direct optical observation or by rotational mechanics during orientation[254].

Multinode systems

Several of the previously presented unit operations can be improved in terms of sample throughput by designing the acoustofluidic channel to allow the formation of multiple

nodes and antinodes. This can be done as previously described in the acoustic theory section, either by increasing the acoustically resonant dimension e.g., widening a separation channel or by increasing the actuation frequency to allow multiple wavelength standing wave formation in a given geometry[191]. By separating highly concentrated suspensions into several streams, a multinode system allows increased sample throughput by distributing particles farther away from each other which alleviates issues with SRF particle-particle interaction that might otherwise cause erroneous system performance[56,149,243]. Multiple node systems can also be used to increase performance in cytometers by allowing concurrent analysis of multiple particles or by diluting particles for easier discrimination, either in acoustic traps with multiple trapping sites or in flow channels with multiple streams[46,63,255].

Acoustic barriers

Multiple wavelength standing waves can also be used as a way to introduce "acoustic barriers" in acoustofluidic systems. This is done by using the nodes or antinodes as a way to confine negative or positive ACF particles to a certain part of the channel cross section by exploiting the tendency of negative contrast particles to be repulsed from nodes just as much as they are attracted to antinodes and vice versa. In paper I and II acoustic barriers are used to prevent fat globules in raw milk from clogging a triple-node acoustofluidic system by laminating the sample in between the two lateral nodes which prevents the fat globules from contaminating the side sheath flows, and eventually aggregating at the channel walls, while the centre node is used to simultaneously extract cells from the sample[48,66]. The fat globules focus into the pair of antinodes on either side of the centre node and can be extracted through side outlets for subsequent analysis.

Fluid flipping

The last unit description described here is the ability to flip the positions of fluids with sufficiently large fluid-fluid ACF variation. The method is analogous to translation of particles into nodes or antinodes according to their ACF, but in fluid flipping it is the entire fluid content that changes position according to the acoustic field. The method can be used as a kind of acoustic valve which for rapid switching e.g., buffers into different target outlets or as a way to manipulate whole populations of suspended particles[58,256–258].

Introduction to included papers

The aim of this section is to briefly introduce the main achievements in each paper in terms of why the research was undertaken, what methods were used and developed and what the results were and how they may benefit the research field and the general public. The main scientific achievement for each paper is stated in the heading.

Paper I – Multinode acoustic barriers for binary separation

In the paper *"Harmonic microchip acoustophoresis: a route to online raw milk sample precondition in protein and lipid content quality control"* the aim was to provide the dairy industry with novel ways to improve raw milk analysis with less impact on the environment. For that reason, a multinode (3*½λ) acoustic silicon chip was developed in order to alleviate the clogging issues inherent to single node half wavelength systems by introducing acoustic barriers that prevent fat globules from reaching the channel walls (Fig. 31a). The resulting acoustofluidic system was able to deplete more than 90% of the fat content in a raw milk sample while collecting the concentrated fat (Fig. 31b). This allowed subsequent optical analysis of milk protein content and fat composition using FTIR-spectroscopy without the need of chemical solvents which may open the path towards rapid milk quality control in small chip based systems. Such systems might benefit the rapidly growing dairy industry in developing countries by providing cheap POC instruments.

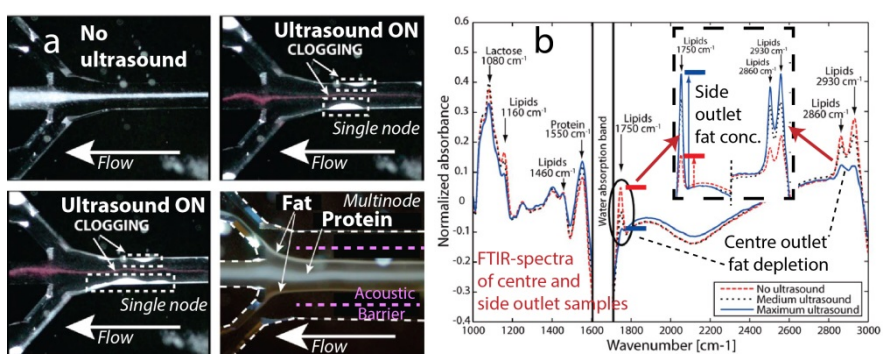

Figure 31, Multinode system with acoustic barriers for improved milk analysis in paper I. Conventional single node systems clog when fat aggregates at the channel walls (a, upper right and lower left). Multinode systems use the lateral nodes as acoustic barriers to prevent fat from reaching the walls (a, lower right). This allows efficient separation and subsequent analysis of raw milk components (b).

Paper II – Multinode acoustic barriers for raw milk cytometry

In the paper *"Label-free somatic cell cytometry in raw milk using acoustophoresis"* the multinode system presented in paper I was used to isolate somatic cells in raw milk and facilitate rapid detection of cows that suffer from mastitis (infection in the uterus) in order to expedite treatment and minimize use of antibiotics (Fig. 32a-b). Raw milk from cows that suffered from different stages of mastitis was handled in the chip and the isolated cells where then counted in a Coulter counter (Fig. 32c). Cell counts from each sample were compared to those achieved with industry standard instruments. The data showed that the chip was able to isolate the somatic cells without any changes to cell counts, which indicate that the system could be integrated in existing instruments to reduce size, cost and fat solvent labelling reagent use. It could also be a part of an LOC-system where cells are first isolated and then counted using an on-chip cytometer. The benefits would be cheaper instrumentation in the dairy industry and faster treatment of cows with the possibility for the farmer to use POC-devices to detect and pinpoint individual cows for treatment on the farm instead of treating the whole herd when the milk has been analysed at a centralized dairy facility.

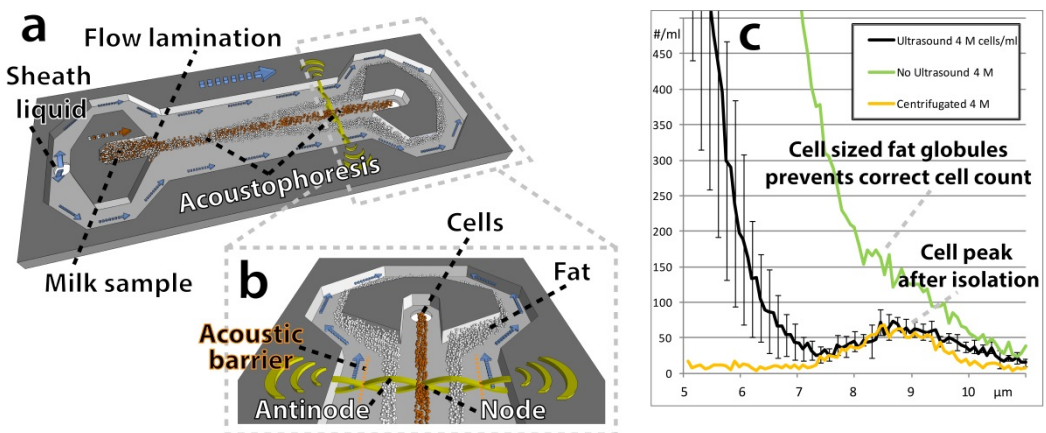

Figure 32, Multinode system with acoustic barriers for raw milk cytometry in paper II. By utilizing the acoustic barrier chip from paper I it is possible to isolate somatic cells from a raw milk sample taken from a cow suffering from mastitis (a). The cells are isolated and extracted through the centre outlet of the chip while the acoustic barriers prevent clogging or erroneous cell isolation (b). Prior to isolation it is not possible to perform label-free cytometry to acquire cell counts, but once the cells are isolated a cell peak is visible in the data (c). The cell counts that were acquired using the acoustic method compared well to those acquired with industrial standard instruments (typically requiring centrifugation and/or labelling for flow cytometry).

Paper III –Two-dimensional positioning for fluorescence activated sorting

In the paper *"Acoustic actuated fluorescence activated sorting of microparticles"* the development of an acoustofluidic chip, which enables fluorescence activated cell sorting in a continuous flow format and allows aseptic integration of downstream microfluidic functionalities for future developments of LOC-devices, is described. The chip utilized two-dimensional acoustic positioning of samples prior to sorting in order to improve performance and sorting purity. Particles were sorted using high amplitude acoustic forces to rapidly deflect positive events into a target outlet based on fluorescent intensity while negative events were allowed to flow into a waste outlet according to the flow regime (Fig. 33). Comparatively high purity and recovery of samples sorted at throughputs of up to 150 particles s^{-1} was reported. These results suggested that it might be possible to integrate online continuous flow sorting of particles and cells in small devices for use in biomedical or clinical applications.

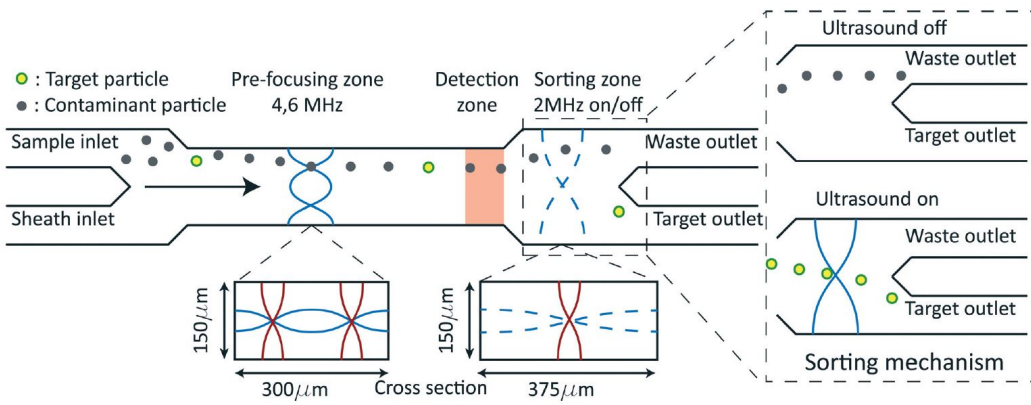

Figure 33, Schematic of the fluorescence activated acoustic cell sorter in paper III. A sample suspension with polystyrene particles was laminated along the side wall of the chip using sheath flow. Two-dimensional positioning of the particles was then performed in a "pre-focusing zone" prior to sorting. The positioning allows precise particle detection and triggering of the transducer that was utilized to deflect target particles into the correct outlet in the downstream sorting zone.

Paper IV – Two-dimensional positioning for improved on-chip cytometry

In the paper *"Two-dimensional acoustic particle focusing enables sheathless chip Coulter counter with planar electrode configuration"* the aim was to develop a low cost - high sensitivity chip cytometer. By utilizing two-dimensional positioning of particles and cells in a glass chip pre-positioning zone it was possible to increase the sensitivity of a downstream planar electrode Coulter-type cytometer. The system was able to precisely count and size particles (polystyrene beads of various size) and cells (diluted whole blood) according to the changes they induce in an electric field within the chip measurement zone. Wet etching of the glass substrate resulted in an acoustofluidic channel with rounded walls. The rounded geometry generated an atypical acoustic node pattern that was successfully modelled in COMSOL during system design and later verified experimentally using confocal microscopy images (Fig. 34a vs. f). With pre-positioning activated it was possible to achieve very good size discrimination of both blood cells and polystyrene beads (CV ~1.5%) (Fig. 34g-h). Each sample was also analysed using a golden standard bench top Coulter counter and the resulting particle counts and size measurement data showed very good correlation with the chip cytometer (Fig. 34h vs. i). These results are proof-of-concept of how acoustic pre-positioning may facilitate a small high sensitivity planar electrode impedance cytometer for use in biomedical or clinical applications. The system could be integrated in POC-devices to allow rapid patient sample analysis in remote areas.

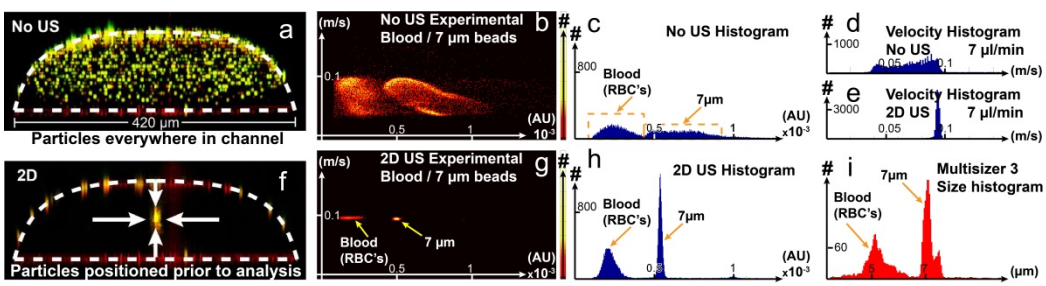

Figure 34, Confocal and Coulter-type measurement experimental data from paper IV. By thorough modelling of the chip it was possible to achieve two-dimensional acoustic positioning in a glass chip with rounded walls (a vs. f). The pre-positioning greatly improved the sensitivity of the on-chip cytometer and allowed discrimination between a population of polystyrene beads and cells in diluted whole blood (b vs. g). Particle velocity data also suggest successful positioning that lead to uniform velocities (d vs. e). A golden standard bench top Coulter-counter was used to evaluate the system and the experimental data from the acoustofluidic device with pre-positioning active correlated well with measurement data from the bench top instrument (c and h vs. i).

Paper V – Two-dimensional positioning for multiple outlet blood sorting

In the paper *"Concurrent isolation of lymphocytes and granulocytes using improved free flow acoustophoresis with cell prefocusing and multiple target outlets"* the aim was to improve current free flow acoustophoresis systems by introducing an upstream pre-positioning zone in combination with multiple downstream target outlets in order to facilitate concurrent isolation of several cell or particle subpopulations. Sample suspension particles were pre-positioned and then laminated along the side of a flow channel prior to sorting. This allowed each particle type to translate towards the pressure node at a velocity that was only dependant on its intrinsic acoustic properties and not on varying initial particle positions in the channel cross section. By careful adjustments of flow vs. acoustic power, polystyrene beads of different sizes and white blood cell subpopulations, was aligned in different flow paths of the medium after sorting and could be extracted from the chip through different target outlets (Fig. 35). The chip was able to isolate lymphocytes, monocytes and granulocytes with high purity and recovery. Notably, the purity and recovery of the lymphocyte (P:95% and R:87%) and granulocyte (P:99% and R:68%) subpopulations compare very well to current methods used to isolate cell subpopulations (most often centrifugation). These results suggest that the acoustic sorting system could be used to reduce the size of current bulky and labour intense blood fractionation instruments or be integrated in other systems to facilitate aseptic continuous flow sorting of biofluids in biomedical or clinical applications.

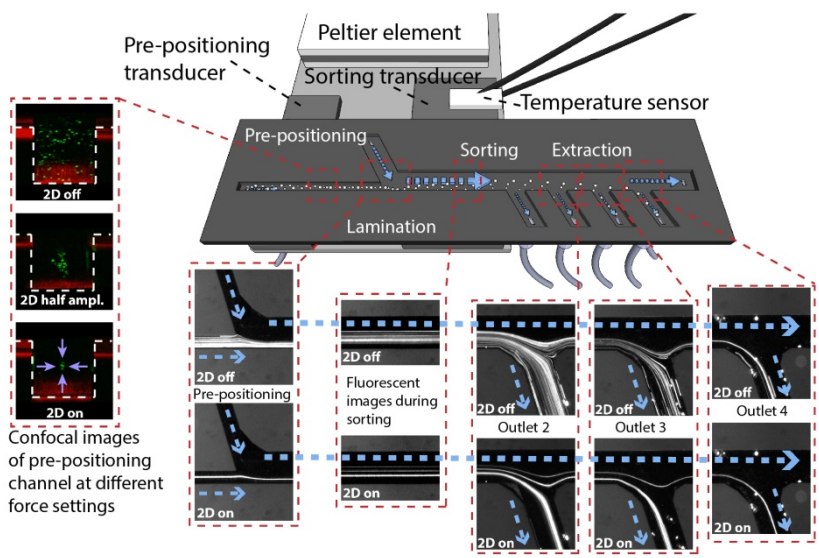

Figure 35, Confocal and fluorescent images from particle sorting experiments in paper V. Using anisotropic wet etching, a chip with a square cross section pre-positioning channel was fabricated (left part). This allowed precise positioning of particles prior to sorting which greatly improved performance (middle part). Sorted particles could then be extracted through multiple target outlets (right part).

Populärvetenskaplig sammanfattning

Vilken musiksmak har blodceller?

Forskningen som presenteras i denna avhandling undersöker och drar nytta av hur olika celler uppför sig när de utsätts för ljud. På samma sätt som människor uppskattar olika sorters musik så reagerar olika typer av celler annorlunda beroende på vilka ljud de utsätts för. Cellerna är dessutom ganska konservativa. När de utsätts för ett visst ljud så dansar eller rör de därför på sig på ett väldigt förutsägbart sätt.

Varför har jag då ägnat flera år åt att forska på hur celler reagerar på ljud? Jo, eftersom cellerna är väldigt små kan de fås att röra på sig i väldigt små utrymmen. Detta underlättar i sin tur för mig i min forskning som går ut på att förflytta celler med hjälp av ljudkrafter med målet att förbättra och förminska system som används för cellsortering eller analys. Metoden kallas akustofores.

Jag har bland annat utvecklat ett sorteringschip som kan minska den tid det tar att sortera och sedan analysera olika typer av blodceller var för sig. Ofta sorteras blodet i stora centrifuger på sjukhusens laboratorier. Innan centrifugeringen kan ske måste dock blodprovet förbehandlas och efter centrifugeringen krävs det fingerfärdig personal för att plocka ut rätt sorts celler. I mitt sorteringschip, som inte är större än en femkrona, går det att sortera olika typer av blodceller från varandra med bättre resultat än de stora centrifugerna utan att det går åt en massa manuell arbetstid.

I avhandlingen visar jag även hur det går att förbättra analysmetoder inom livsmedelsindustrin. Jag presenterar ett mikrochip där celler och fett i mjölk separaras med akustofores vilket gör det möjligt att miniatyrisera de redskap som används för kvalitetskontroll av mjölk. Istället för att mjölkbonden ska behöva vänta på resultat från mejeriernas stora mjölkanalysinstrument så kan hen själv kontrollera mjölken på gården och direkt få reda på om en viss ko till exempel blivit sjuk. På så vis får inte bara kon snabbare behandling utan bonden slipper också ge antibiotika till de andra korna helt i onödan. Således kan vi minska mängden antibiotika i den mjölk vi ska dricka, korna blir friska snabbare och bonden sparar pengar. Samtidigt minskas användandet av både antibiotika och onaturliga fettlösningsmedel inom mejeriindustrin.

För att ytterligare kunna förminska analysinstrumenten så har jag även utvecklat ett litet chip som inte bara sorterar cellerna utan även analyserar dem direkt. Tekniken går ut på att mäta cellernas storlek eller se vilken typ av celler det är med hjälp av svaga elektriska strömmar. Normalt sett krävs det avancerade elektrodlösningar för att kunna utföra elektrisk cellanalys (impedansspektroskopi) med hög noggrannhet. I mikrochippet används ljudkrafter för att placera cellerna på en bestämd plats i chippet vilket gör det möjligt att använda enkla elektrodkonfigurationer för att analysera dem.

I likhet med resten av forskningen jag presenterar så gör även detta chip det möjligt att utveckla små, billiga eller handburna instrument.

Resultaten av min forskning är viktiga eftersom de gör det enklare och billigare för samhället att upptäcka sjukdomar eller genomföra grundläggande forskning på olika celltyper. Det är dock inte bara Sverige eller andra länder med välutvecklad infrastruktur för hälsovård eller livsmedelkontroll som kan dra nytta av mina forskningsresultat. I Kina ökar till exempel mjölkdrickandet kraftigt samtidigt som det inte finns några bra rutiner för kvalitetskontroll och i Indien där det både produceras och dricks mest mjölk i världen har inte alla råd med bra analysinstrument. Genom att göra det möjligt för bönder och statliga verk i dessa länder att få tillgång till billiga handburna ”point-of-care” instrument kan min teknik göra stor nytta.

Billiga ”point-of-care” instrument är även till stor nytta för hälsovårdsarbetare i fattiga länder. De skulle kunna använda handburna medicinska instrument för att upptäcka och behandla sjukdomar på landsbygden och på så sätt förhindra spridning av epedemier. Med det miniatyriserade blodsorteringsinstrumentet som jag presenterar här skulle man till exempel kunna mäta förhållandet mellan olika vita blodkroppar i ett blodprov och på så sätt kanske avgöra om en patient lider av HIV eller andra sjukdomar.

Bakgrunden till att vi på institutionen för Biomedicinsk Teknik vid Lunds universitet bedriver denna typ av forskning är att vi sedan flera årtionden har forskat på ljudets egenskaper och vidareutvecklat de apparater som krävs för att alstra och använda ljud i olika applikationer, med speciell inriktning på ultraljud, dvs ljud med frekvenser över 20 000 Hz. Inom ramen för forskningen på vår institution utvecklades under 1950- och 60-talet det medicinska ultraljudet som idag är en av de viktigaste diagnostikmetoderna på sjukhus världen över. Den som bedrev denna forskning i Lund var Hellmuth Hertz, den första professorn på vår institution. Det medicinska ultraljudet alstras med hjälp av kristaller som vibrerar i hög frekvens. Hellmuth Hertz använde senare samma sorts kristaller för att stabilisera droppbildningen i de första bläckstråleskrivarna.

Arbetet med medicinska applikationer för ultraljud har fortsatt på institutionen och nyligen presenterade vi en metod för att detektera cirkulerande tumörceller som bygger på samma teknik som jag använder i den här avhandligen. Inom cancerforskningen har det på senare år visat sig att dessa celler kan indikera att en cancertumör har spridit sig. Genom att upptäcka de cirkulerande tumörcellerna kan man då i ett tidigt skede sätta in rätt sorts behandling för patienten. Eftersom metoden inte bara möjliggör små utan även relativt billiga analysinstrument hoppas vi att den ska leda till att fler kontroller genomförs och således minska antalet patienter som inte får rätt behandling från början.

Den typ av kristaller som Hellmuth Hertz använde när han uppfann det medicinska ultraljudet använder jag idag för att alstra de ultraljudskrafter som genom akustofores sorterar och flyttar cellerna till olika positioner i mina mikrochip. Genom att dra nytta av de senaste årtiondenas framsteg inom mikrofabrikation kan jag tillverka små flödeskanaler i mikrochippen där cellerna i till exempel mjölk, vatten eller blod kan adresseras till olika utlopp eller positioner. Ljudvågor breder ut sig genom tryckvariationer. Det är dessa tryckvariationer som får oss att höra ljud genom att trumhinnan rör på sig när den utsätts för tryckvariationen i ljudvågen. På samma sätt använder jag

krafterna som alstras av tryckvariationerna i mina flödeskanaler för att röra på celler och andra små partiklar. Genom att fästa vibrerande piezokeramiska kristaller på mikrochippet kan ljudet ledas in i flödeskanalen. Genom att anpassa ljudfrekvensen (oftast runt 2 MHz) till flödeskanalerns storlek kan jag sedan skapa stående ultraljudsvågor, dvs ljudekon som studsar från vägg till vägg, eller mellan tak och botten i kanalerna, utan att tappa nämnvärt mycket energi. De stående vågorna orsakar en dramatisk ökning av ljudkrafterna inne i kanalen vilket gör det möjligt att snabbt flytta cellerna till bestämda positioner i flödeskanalen. Ljudkraften påverkar cellerna olika beroende på deras storlek, densitet och kompressibilitet. Genom att anpassa ljudkrafterna och kanalernas utformning efter olika celltyper kan jag sedan sortera dem från varandra eller fokusera dem i väldigt exakta positioner i kanalen.

Hur var det då med blodcellernas musiksmak? Jo, i en 375 mikrometer bred kanal blir det full fart på dem när de utsätts för musik i form av 2 MHz ultraljud.

References

1. R. Hooke, *Micrographia*, Royal Society, 1665.
2. A. van Leeuwenhoek, *Letters to the Royal Society*, 1676.
3. R. Feynman, *Caltech Eng. Sci.*, 1960, **23**, 22–36.
4. E. Bassous, H. H. Taub, and L. Kuhn, *Appl. Phys. Lett.*, 1977, **31**, 135.
5. S. C. Terry, J. H. Jerman, and J. B. Angell, *IEEE Trans. Electron Devices*, 1979, **26**, 1880–1886.
6. A. Manz, N. Graber, and H. M. Widmer, *Sensors Actuators B Chem.*, 1990, **1**, 244–248.
7. A. Manz, D. J. Harrison, E. M. J. Verpoorte, J. C. Fettinger, A. Paulus, H. Li, and H. M. Widmer, *J. Chromatogr.*, 1992, **593**, 253–258.
8. D. Harrison, K. Fluri, and K. Seiler, *Science (80-.).*, 1993, **261**, 895–897.
9. D. C. Duffy, J. C. McDonald, O. J. Schueller, and G. M. Whitesides, *Anal. Chem.*, 1998, **70**, 4974–84.
10. D. R. Reyes, D. Iossifidis, P.-A. Auroux, and A. Manz, *Anal. Chem.*, 2002, **74**, 2623–2636.
11. V. Srinivasan, V. K. Pamula, and R. B. Fair, 2004.
12. P. S. Dittrich and A. Manz, *Nat. Rev. Drug Discov.*, 2006, **5**, 210–8.
13. D. Erickson and D. Li, *Anal. Chim. Acta*, 2004, **507**, 11–26.
14. F. Balagaddé, L. You, and C. Hansen, *Science (80-.).*, 2005, **309**, 137–40.
15. M. A. Shoffner, J. Cheng, G. E. Hvichia, L. J. Kricka, and P. Wilding, 1996, **24**, 375–379.
16. E. T. Lagally, I. Medintz, and R. A. Mathies, 2001, **73**, 565–570.
17. S. Haeberle and R. Zengerle, *Lab Chip*, 2007, **7**, 1094–110.
18. D. Mark, S. Haeberle, G. Roth, F. von Stetten, and R. Zengerle, *Chem. Soc. Rev.*, 2010, **39**, 1153–82.
19. G. M. Whitesides, *Nature*, 2006, **442**, 368–73.
20. E. Verpoorte, *Electrophoresis*, 2002, **23**, 677–712.

21. A. A. S. Bhagat, H. Bow, H. W. Hou, S. J. Tan, J. Han, and C. T. Lim, *Med. Biol. Eng. Comput.*, 2010, **48**, 999–1014.

22. B. Cetin and D. Li, *Electrophoresis*, 2011, **32**, 2410–27.

23. D. Di Carlo, *Lab Chip*, 2009, **9**, 3038–46.

24. D. R. Gossett, W. M. Weaver, A. J. Mach, S. C. Hur, H. T. K. Tse, W. Lee, H. Amini, and D. Di Carlo, *Anal. Bioanal. Chem.*, 2010, **397**, 3249–67.

25. D. G. Grier, *Nature*, 2003, **424**, 810–6.

26. J. S. McGrath, M. Jimenez, and H. L. Bridle, *Lab Chip*, 2014, **14**, 4139–4158.

27. N. Pamme, *Lab Chip*, 2007, **7**, 1644–59.

28. T. M. Squires and S. R. Quake, *Rev. Mod. Phys.*, 2005, **77**.

29. H. Watarai, *Annu. Rev. Anal. Chem. (Palo Alto. Calif).*, 2013, **6**, 353–78.

30. N.-T. Nguyen and Z. Wu, *J. Micromechanics Microengineering*, 2005, **15**, R1–R16.

31. H. Klank, G. Goranovi , J. P. Kutter, H. Gjelstrup, J. Michelsen, and C. H. Westergaard, *J. Micromechanics Microengineering*, 2002, **12**, 862–869.

32. D. Di Carlo, D. Irimia, R. G. Tompkins, and M. Toner, *Proc. Natl. Acad. Sci. U. S. A.*, 2007, **104**, 18892–7.

33. I. Gregoratto, C. J. McNeil, and M. W. Reeks, in *SPIE 6465, Microfluidics, BioMEMS, and Medical Microsystems V*, eds. I. Papautsky and W. Wang, 2007, vol. 6465, pp. 646503–646503–8.

34. M. Yamada, M. Nakashima, and M. Seki, *Anal. Chem.*, 2004, **76**, 5465–71.

35. L. R. Huang, E. C. Cox, R. H. Austin, and J. C. Sturm, *Science*, 2004, **304**, 987–90.

36. S. Choi and J.-K. Park, *Lab Chip*, 2007, **7**, 890–7.

37. R. Pethig, *Crit. Rev. Biotechnol.*, 1996, **16**, 331–348.

38. C. Wilhelm, F. Gazeau, and J.-C. Bacri, *Eur. Biophys. J.*, 2002, **31**, 118–25.

39. M. M. Wang, E. Tu, D. E. Raymond, J. M. Yang, H. Zhang, N. Hagen, B. Dees, E. M. Mercer, A. H. Forster, I. Kariv, P. J. Marchand, and W. F. Butler, *Nat. Biotechnol.*, 2005, **23**, 83–7.

40. Z. Mandralis and D. Feke, *Chem. Eng. Sci.*, 1993, **48**, 3897–3905.

41. C. Simonnet and A. Groisman, *Appl. Phys. Lett.*, 2005, **87**, 114104.

42. J. Voldman, *Annu. Rev. Biomed. Eng.*, 2006, **8**, 425–54.

43. J. J. Hawkes and W. T. Coakley, *Sensors Actuators B Chem.*, 2001, **75**, 213–222.

44. F. Petersson, A. Nilsson, C. Holm, H. Jonsson, and T. Laurell, *Lab Chip*, 2005, **5**, 20–2.

45. A. Nilsson, F. Petersson, H. Jönsson, and T. Laurell, *Lab Chip*, 2004, **4**, 131–5.

46. R. J. Townsend, M. Hill, N. R. Harris, and N. M. White, *Ultrasonics*, 2006, **44 Suppl 1**, e467–71.

47. G. Goddard and G. Kaduchak, *J. Acoust. Soc. Am.*, 2005, **117**, 3440.

48. C. Grenvall, P. Augustsson, J. R. Folkenberg, and T. Laurell, *Anal. Chem.*, 2009, **81**, 6195–6200.

49. T. Laurell, F. Petersson, and A. Nilsson, *Chem. Soc. Rev.*, 2007, **36**, 492–506.

50. J. Wu, *J. Acoust. Soc. Am.*, 1991, **89**, 2140.

51. F. Trampler, S. A. Sonderhoff, P. W. S. Pui, D. G. Kilburn, and J. M. Piret, *Bio/Technology*, 1994, **12**, 281–284.

52. H. M. Hertz, *J. Appl. Phys.*, 1995, **78**, 4845.

53. T. Lilliehorn, M. Nilsson, U. Simu, S. Johansson, M. Almqvist, J. Nilsson, and T. Laurell, *Sensors Actuators B Chem.*, 2005, **106**, 851–858.

54. B. Hammarström, M. Evander, H. Barbeau, M. Bruzelius, J. Larsson, T. Laurell, and J. Nilsson, *Lab Chip*, 2010, **10**, 2251–2257.

55. M. Evander and J. Nilsson, *Lab Chip*, 2012, **12**, 4667–76.

56. O. Jakobsson, C. Grenvall, M. Nordin, M. Evander, and T. Laurell, *Lab Chip*, 2014, **14**, 1943–50.

57. O. Manneberg, S. Melker Hagsäter, J. Svennebring, H. M. Hertz, J. P. Kutter, H. Bruus, and M. Wiklund, *Ultrasonics*, 2009, **49**, 112–9.

58. M. D. Ward, C. C. Stewart, and G. Kaduchak, 2012.

59. J. Persson, P. Augustsson, T. Laurell, and M. Ohlin, *FEBS J.*, 2008, **275**, 5657–66.

60. P. Augustsson, J. Persson, S. Ekström, M. Ohlin, and T. Laurell, *Lab Chip*, 2009, **9**, 810–8.

61. P. Augustsson, J. Malm, and S. Ekström, *Biomicrofluidics*, 2012, **6**, 34115.

62. F. Petersson, A. Nilsson, H. Jönsson, and T. Laurell, *Anal. Chem.*, 2005, **77**, 1216–21.

63. M. E. Piyasena, P. P. Austin Suthanthiraraj, R. W. Applegate, A. M. Goumas, T. a Woods, G. P. López, and S. W. Graves, *Anal. Chem.*, 2012, **84**, 1831–9.

64. S. Graves, R. W. Applegate, G. Lopez, and M. E. Piyasena, *US Pat. …*, 2014, 1.

65. L. a Kuznetsova and W. T. Coakley, *Biosens. Bioelectron.*, 2007, **22**, 1567–77.

66. C. Grenvall, J. R. Folkenberg, P. Augustsson, and T. Laurell, *Cytom. Part A J. Int. Soc. Anal. Cytol.*, 2012, **81**, 1076–83.

67. C. Grenvall, C. Antfolk, C. Zoffmann Bisgaard, and T. Laurell, *Lab Chip*, 2014.

68. C. Grenvall, C. Magnusson, H. Lilja, and T. Laurell, *Manuscr. Submiss.*, 2014.

69. B. Hammarström, T. Laurell, and J. Nilsson, *Lab Chip*, 2012, **12**, 4296–304.

70. J. F. Nye, *J. Glaciol.*, 1952, **2**, 82–93.

71. P. A. Shumskiy, *Int. Assoc. Sci. Hydrol.*, 1961, **55**, 142–147.

72. O. Reynolds, *Philos. Trans. R. Soc. London*, 1883, **174**, 935–982.

73. X. Zheng and Z. Silber-Li, *Exp. Fluids*, 2008, **44**, 951–959.

74. P. J. Crosland-Taylor, *Nature*, 1953, **171**, 37–38.

75. W. A. Bonner, H. R. Hulett, R. G. Sweet, and L. A. Herzenberg, *Rev. Sci. Instrum.*, 1972, **43**, 404–409.

76. H. Shapiro, *Practical flow cytometry*, John Wiley & Sons, 2005.

77. S. Miller, D. Dykes, and H. Polesky, *Nucleic Acids Res.*, 1988, **16**, 55404.

78. J. Graham, *Biological Centrifugation*, Garland Science, 2001.

79. J. Lebowitz, M. S. Lewis, and P. Schuck, *Protein Sci.*, 2002, **11**, 2067–79.

80. T. Svedberg and K. O. Pedersen, *The Ultracentrifuge*, 1940.

81. W. a Skoog and W. S. Beck, *Blood*, 1956, **11**, 436–54.

82. A. Bøyum, *Nature*, 1964, **204**, 793–794.

83. A. Bøyum, *Scand. J. Immunol.*, 1976, **Suppl 5**, 9–15.

84. G. Oster and M. Yamamoto, *Chem. Rev.*, 1963, **63**, 257–268.

85. R. Yang, D. L. Feeback, and W. Wang, *Sensors Actuators A Phys.*, 2005, **118**, 259–267.

86. N. Sundararajan, M. S. Pio, L. P. Lee, and A. A. Berlin, *J. Microelectromechanical Syst.*, 2004, **13**, 559–567.

87. C.-C. Chang, Z.-X. Huang, and R.-J. Yang, *J. Micromechanics Microengineering*, 2007, **17**, 1479–1486.

88. M. Rhee, P. M. Valencia, M. I. Rodriguez, R. Langer, O. C. Farokhzad, and R. Karnik, *Adv. Mater.*, 2011, **23**, H79–83.

89. A. Wolff, I. R. Perch-Nielsen, U. D. Larsen, P. Friis, G. Goranovic, C. R. Poulsen, J. P. Kutter, and P. Telleman, *Lab Chip*, 2003, **3**, 22–7.

90. D. Spencer and H. Morgan, *Lab Chip*, 2011, **11**, 1234–9.

91. P. M. Goodwin, W. P. Ambrose, J. C. Martin, and R. a Keller, *Cytometry*, 1995, **21**, 133–44.

92. G. Segré and A. Silberberg, *Nature*, 1961, **189**, 209–210.

93. L. G. Leal, *Annu. Rev. Fluid Mech.*, 1980, **12**, 435–476.

94. A. P. Sudarsan and V. M. Ugaz, *Proc. Natl. Acad. Sci. U. S. A.*, 2006, **103**, 7228–33.

95. P. G. Saffman, *J. Fluid Mech.*, 1965, **22**, 385–400.

96. B. P. Ho and L. G. Leal, *J. Fluid Mech.*, 1974, **65**, 365–400.

97. P. Cherukat and J. McLaughlin, *J. Fluid Mech.*, 1994, **263**, 1–18.

98. E. Asmolov, *J. Fluid Mech.*, 1999, **381**, 63–87.

99. A. Acrivos, *Zeitung Angew. Math. Phys.*, 1985, **36**, 174–178.

100. S. C. Hur, S.-E. Choi, S. Kwon, and D. Di Carlo, *Appl. Phys. Lett.*, 2011, **99**, 044101.

101. S. C. Hur, N. K. Henderson-MacLennan, E. R. B. McCabe, and D. Di Carlo, *Lab Chip*, 2011, **11**, 912–20.

102. H. Amini, W. Lee, and D. Di Carlo, *Lab Chip*, 2014, **14**, 2739–61.

103. W. R. Dean, *London, Edinburgh, Dublin Philos. Mag. J. Sci.*, 1927, **4**, 208–223.

104. A. A. S. Bhagat, S. S. Kuntaegowdanahalli, and I. Papautsky, *Lab Chip*, 2008, **8**, 1906–14.

105. J. Seo, M. H. Lean, and A. Kole, *Appl. Phys. Lett.*, 2007, **91**, 033901.

106. J. F. Ashley, C. N. Bowman, and R. H. Davis, *AIChE J.*, 2013, **59**, 3444–3457.

107. T. Morijiri, S. Sunahiro, M. Senaha, M. Yamada, and M. Seki, *Microfluid. Nanofluidics*, 2011, **11**, 105–110.

108. O. Shardt, S. K. Mitra, and J. J. Derksen, *Chem. Eng. Sci.*, 2012, **75**, 106–119.

109. A. L. Vig and A. Kristensen, *Appl. Phys. Lett.*, 2008, **93**, 203507.

110. J. Takagi, M. Yamada, M. Yasuda, and M. Seki, *Lab Chip*, 2005, **5**, 778–84.

111. D. W. Inglis, K. J. Morton, J. a Davis, T. J. Zieziulewicz, D. a Lawrence, R. H. Austin, and J. C. Sturm, *Lab Chip*, 2008, **8**, 925–31.

112. J. P. Beech and J. O. Tegenfeldt, *Lab Chip*, 2008, **8**, 657–9.

113. J. a Davis, D. W. Inglis, K. J. Morton, D. a Lawrence, L. R. Huang, S. Y. Chou, J. C. Sturm, and R. H. Austin, *Proc. Natl. Acad. Sci. U. S. A.*, 2006, **103**, 14779–84.

114. D. W. Inglis, *Appl. Phys. Lett.*, 2009, **94**, 013510.

115. J. P. Beech, P. Jönsson, and J. O. Tegenfeldt, *Lab Chip*, 2009, **9**, 2698–706.

116. S. Chang and Y.-H. Cho, *Lab Chip*, 2008, **8**, 1930–6.

117. J. Zhou, S. Kasper, and I. Papautsky, *Microfluid. Nanofluidics*, 2013, **15**.

118. S. Choi, T. Ku, S. Song, C. Choi, and J.-K. Park, *Lab Chip*, 2011, **11**, 413–8.

119. S. Song, M. S. Kim, and S. Choi, *Small*, 2014, **Advance ar**.

120. H. a. Pohl, *J. Appl. Phys.*, 1951, **22**, 869.

121. R. Pethig, *Biomicrofluidics*, 2010, **4**.

122. C. Chou, J. O. Tegenfeldt, O. Bakajin, S. S. Chan, E. C. Cox, N. Darnton, T. Duke, and R. H. Austin, 2002, **83**, 2170–2179.

123. I. Barbulovic-Nad, X. Xuan, J. S. H. Lee, and D. Li, *Lab Chip*, 2006, **6**, 274–9.

124. J. Suehiro and R. Pethig, *J. Phys. D. Appl. Phys.*, 1998, **31**, 3298–3305.

125. J. Voldman, R. A. Braff, M. Toner, M. L. Gray, and M. A. Schmidt, 2001, **80**, 531–542.

126. R. C. Gallo-Villanueva, C. E. Rodríguez-López, R. I. Díaz-de-la-Garza, C. Reyes-Betanzo, and B. H. Lapizco-Encinas, *Electrophoresis*, 2009, **30**, 4195–205.

127. S. Bunthawin, P. Wanichapichart, A. Tuantranont, and H. G. L. Coster, *Biomicrofluidics*, 2010, **4**, 14102.

128. D. S. Gray, J. L. Tan, J. Voldman, and C. S. Chen, *Biosens. Bioelectron.*, 2004, **19**, 771–780.

129. N. Pamme and A. Manz, *Anal. Chem.*, 2004, **76**, 7250–6.

130. M. a. M. Gijs, *Microfluid. Nanofluidics*, 2004, 22–40.

131. S. Miltenyi, W. Muller, W. Weichel, and A. Radbruch, *Cytometry*, 1990, **11**, 231–238.

132. N. Pamme, *Lab Chip*, 2006, **6**, 24–38.

133. M. Zborowski, G. R. Ostera, L. R. Moore, S. Milliron, and J. J. Chalmers, *Biophys. J.*, 2003, **84**, 2638–2645.

134. J. Ugelstad and F. K. Hansen, *Rubber Chem. Technol.*, 1976, **49**, 536–609.

135. N. Pamme, *Curr. Opin. Chem. Biol.*, 2012, **16**, 436–43.

136. S. a Peyman, A. Iles, and N. Pamme, *Lab Chip*, 2009, **9**, 3110–7.

137. A. Ashkin, *Phys. Rev. Lett.*, 1970, **24**, 156–159.

138. A. Ashkin, J. M. Dziedzic, J. E. Bjorkholm, and S. Chu, *Opt. Lett.*, 1986, **11**, 288.

139. A. Ashkin, *Proc. Natl. Acad. Sci. U. S. A.*, 1997, **94**, 4853–4860.

140. M. MacDonald, G. Spalding, and K. Dholakia, *Nature*, 2003, **426**, 421–424.

141. J. E. Curtis, B. A. Koss, and D. G. Grier, *Opt. Commun.*, 2002, **207**, 169–175.

142. C. G. Hebert, A. Terray, and S. J. Hart, *Anal. Chem.*, 2011, **83**, 5666–72.

143. L. A. Crum, *J. Acoust. Soc. Am.*, 1971, **50**, 157.

144. N. V. Baker, *Nature*, 1972, **239**, 398–399.

145. E. Benes, F. Hager, W. Bolek, and M. Gröschl, in *Ultrason. Int. Conf., Le Touquet, France*, 1991, pp. 167–170.

146. G. Whitworth, M. A. Grundy, and W. T. Coakley, *Ultrasonics*, 1991, **29**, 439–444.

147. O. Doblhoff-Dier, T. Gaida, H. Katinger, W. Burger, M. Gröschl, and E. Benes, *Biotechnol. Prog.*, 1994, **10**, 428–32.

148. K. Yasuda, S. Umemura, and K. Takeda, *Jpn. J. Appl. Phys.*, 1995, **34**, 2715–2720.

149. P. Augustsson, C. Magnusson, M. Nordin, H. Lilja, and T. Laurell, *Anal. Chem.*, 2012, **84**, 7954–62.

150. J. J. Hawkes, W. T. Coakley, M. Gröschl, E. Benes, S. Armstrong, P. J. Tasker, and H. Nowotny, *J. Acoust. Soc. Am.*, 2002, **111**, 1259.

151. S. M. Hagsäter, T. G. Jensen, H. Bruus, and J. P. Kutter, *Lab Chip*, 2007, **7**, 1336–44.

152. F. Petersson, L. Aberg, A.-M. Swärd-Nilsson, and T. Laurell, *Anal. Chem.*, 2007, **79**, 5117–23.

153. O. Manneberg, J. Svennebring, H. M. Hertz, and M. Wiklund, *J. Micromechanics Microengineering*, 2008, **18**, 095025.

154. M. Nordin and T. Laurell, *Lab Chip*, 2012, **12**, 4610–6.

155. C. D. Wood, S. D. Evans, J. E. Cunningham, R. O'Rorke, C. Wälti, and a. G. Davies, *Appl. Phys. Lett.*, 2008, **92**, 044104.

156. J. Shi, X. Mao, D. Ahmed, A. Colletti, and T. J. Huang, *Lab Chip*, 2008, **8**, 221.

157. T. Franke, A. R. Abate, D. a Weitz, and A. Wixforth, *Lab Chip*, 2009, **9**, 2625–7.

158. J. Shi, H. Huang, Z. Stratton, Y. Huang, and T. J. Huang, *Lab Chip*, 2009, **9**, 3354–9.

159. L. Y. Yeo and J. R. Friend, *Biomicrofluidics*, 2009, **3**, 12002.

160. J. Shi, D. Ahmed, X. Mao, S.-C. S. Lin, A. Lawit, and T. J. Huang, *Lab Chip*, 2009, **9**, 2890–5.

161. J. Shi, S. Yazdi, S.-C. S. Lin, X. Ding, I.-K. Chiang, K. Sharp, and T. J. Huang, *Lab Chip*, 2011, **11**, 2319–24.

162. Z. Wang and J. Zhe, *Lab Chip*, 2011, **11**, 1280–5.

163. J. Hultström, O. Manneberg, K. Dopf, H. M. Hertz, H. Brismar, and M. Wiklund, *Ultrasound Med. Biol.*, 2007, **33**, 145–51.

164. M. Wiklund, *Lab Chip*, 2012, **12**, 2018–28.

165. M. a Burguillos, C. Magnusson, M. Nordin, A. Lenshof, P. Augustsson, M. J. Hansson, E. Elmér, H. Lilja, P. Brundin, T. Laurell, and T. Deierborg, *PLoS One*, 2013, **8**, e64233.

166. M. Gedge and M. Hill, *Lab Chip*, 2012, **12**, 2998–3007.

167. L. Y. Yeo and J. R. Friend, *Annu. Rev. Fluid Mech.*, 2014, **46**, 379–406.

168. A. T. Islam, A. H. Siddique, T. S. Ramulu, V. Reddy, Y.-J. Eu, S. H. Cho, and C. Kim, *Biomed. Microdevices*, 2012, **14**, 1077–84.

169. E. Chladni, *Entdeckungen über die Theorie des Klanges*, 1787.

170. H. L. F. von Helmholtz, *On the Sensations of Tone as a Physiological Basis for the Theory of Music*, Druck und Verlag von Friedrich Vieweg und Sohn, 1863.

171. L. Rayleigh, *Philos. Trans. R. Soc. London*, 1884, **175**, 1–21.

172. Lord Rayleigh, *Philos. Mag.*, 1902, **3**, 338–346.

173. L. V. King, *Proc. R. Soc. London, Ser. A (Mathematical Phys. Sci.*, 1934, **147**, 212–240.

174. K. Yosioka and Y. Kawasima, *Acta Acust. united with Acust.*, 1955, **5**, 167–173.

175. L. P. Gorkov, *Sov. Phys. Dokl.*, 1962, **6**, 773–775.

176. R. Barnkob, P. Augustsson, T. Laurell, and H. Bruus, *Lab Chip*, 2010, **10**, 563–70.

177. A. Kundt, *Ann. Phys.*, 1866, **127**, 497–523.

178. A. A. Doinikov, *J. Acoust. Soc. Am.*, 1997, **101**, 713–721.

179. M. Settnes and H. Bruus, *Phys. Rev. E*, 2012, **85**, 016327 1–12.

180. M. Gröschl, *Acta Acust. united with Acust.*, 1998, 432–447.

181. V. Bjerknes, *Fields of Force*, 1909.

182. C. Mikkelsen, M. Fougt Hansen, and H. Bruus, *J. Magn. Magn. Mater.*, 2005, **293**, 578–583.

183. M. Faraday, *Philos. Trans. R. Soc. London*, 1831, **121**, 299–340.

184. V. Dvorak, *Ann. Phys.*, 1876, **157**, 42.

185. H. Schlichting, *Phys. Zeitung*, 1932, **33**, 327–335.

186. M. Antfolk, P. B. Muller, P. Augustsson, H. Bruus, and T. Laurell, *Lab Chip*, 2014, **14**, 2791–9.

187. P. B. Muller, R. Barnkob, M. J. H. Jensen, and H. Bruus, *Lab Chip*, 2012, **12**, 4617–27.

188. A. Wixforth, *Superlattices Microstruct.*, 2003, **33**, 389–396.

189. C. Eckart, *Phys. Rev.*, 1948, **73**, 68–76.

190. W. L. Nyborg, *J. Acoust. Soc. Am.*, 1953, **25**, 68.

191. J. J. Hawkes and S. Radel, *Lab Chip*, 2013, **13**, 610–27.

192. C. Grenvall, M. Carlsson, P. Augustsson, F. Petersson, and T. Laurell, in *Eleventh International Conference on Miniaturized Systems for Chemistry and Life Sciences*, 2007, vol. 2, pp. 1813–1815.

193. G. Goddard, J. C. Martin, S. W. Graves, and G. Kaduchak, *Cytometry. A*, 2006, **69**, 66–74.

194. M. Stjernström and J. Roeraade, *J. Micromechanics …*, 1998, **33**.

195. C.-H. Lin, G.-B. Lee, Y.-H. Lin, and G.-L. Chang, *J. Micromechanics Microengineering*, 2001, **11**, 726–732.

196. Y. Liao, J. Song, E. Li, Y. Luo, Y. Shen, D. Chen, Y. Cheng, Z. Xu, K. Sugioka, and K. Midorikawa, *Lab Chip*, 2012, **12**, 746–9.

197. C. Iliescu, B. Chen, and J. Miao, *Sensors Actuators A Phys.*, 2008, **143**, 154–161.

198. X. Li, T. Abe, and M. Esashi, *Sensors actuators A Phys.*, 2001, **87**, 139–145.

199. L. Li, T. Abe, and M. Esashi, *J. Vac. Sci. Technol. B Microelectron. Nanom. Struct.*, 2003, **21**, 2545.

200. M. Evander, A. Lenshof, T. Laurell, and J. Nilsson, *Anal. Chem.*, 2008, **80**, 5178–85.

201. M. Evander and M. Tenje, *J. Micromechanics Microengineering*, 2014, **24**, 027003.

202. Y. Xia and G. Whitesides, *Annu. Rev. Mater. Sci.*, 1998.

203. S. R. Quake, *Science (80-.).*, 2000, **290**, 1536–1540.

204. M. a. Unger, *Science (80-.).*, 2000, **288**, 113–116.

205. D. B. Weibel, W. R. Diluzio, and G. M. Whitesides, *Nat. Rev. Microbiol.*, 2007, **5**, 209–18.

206. S. Y. Chou, P. R. Krauss, and P. J. Renstrom, *Appl. Phys. Lett.*, 1995, **67**, 3114.

207. J. McDonald and G. Whitesides, *Acc. Chem. Res.*, 2002, **35**.

208. P. M. van Midwoud, A. Janse, M. T. Merema, G. M. M. Groothuis, and E. Verpoorte, *Anal. Chem.*, 2012, **84**, 3938–44.

209. D. Armani, C. Liu, and N. Aluru, *Micro Electro Mech. Syst. …*, 1999, 222–227.

210. L. Johansson, J. Enlund, S. Johansson, I. Katardjiev, M. Wiklund, and V. Yantchev, *J. Micromechanics Microengineering*, 2012, **22**, 025018.

211. Y. Chen, A. A. Nawaz, Y. Zhao, P.-H. Huang, J. P. McCoy, S. J. Levine, L. Wang, and T. J. Huang, *Lab Chip*, 2014, **14**, 916–23.

212. I. Leibacher, S. Schatzer, and J. Dual, *Lab Chip*, 2014, **14**, 463–70.

213. R. M. White and F. W. Voltmer, *Appl. Phys. Lett.*, 1965, **7**, 314.

214. S.-C. S. Lin, X. Mao, and T. J. Huang, *Lab Chip*, 2012, **12**, 2766–70.

215. Z. T. F. Yu, K. M. Aw Yong, and J. Fu, *Small*, 2014, **10**, 1687–703.

216. F. A. Duck, *Physical properties of tissues: a comprehensive reference book*, Academic Press, 1990.

217. E. Carstensen, K. Li, and H. Schwan, *J. Acoust. …*, 1953, 22–25.

218. O. Jakobsson, M. Antfolk, and T. Laurell, *Anal. Chem.*, 2014, **86**, 6111–4.

219. H. Azhari, *Basics of biomedical ultrasound for engineers*, John Wiley & Sons, 2010.

220. S. A. Goss, L. A. Frizzell, and F. Dunn, *J. Acoust. Soc. Am.*, 1980, **67**, 1041.

221. D. J. McClements, *Crit. Rev. Food Sci. Nutr.*, 1997, **37**, 1–46.

222. T. Mason, L. Paniwnyk, and J. Lorimer, *Ultrason. Sonochem.*, 1996, **3**.

223. L. Elvira, J. Rodríguez, and L. C. Lynnworth, *J. Acoust. Soc. Am.*, 2009, **125**, EL177–82.

224. D. McClements and M. Povey, *Ultrasonics*, 1992, **30**, 383–388.

225. K. A. Wichterman, A. E. Baue, and I. H. Chaudry, *J. Surg. Res.*, 1980, **29**, 189–201.

226. D. C. Angus, W. T. Linde-Zwirble, J. Lidicker, G. Clermont, J. Carcillo, and M. R. Pinsky, *Crit. Care Med.*, 2001, **29**, 1303–1310.

227. M. C. Rea, T. M. Cogan, and S. Tobin, 1992, 331–336.

228. N. J. Ashbolt, *Toxicology*, 2004, **198**, 229–38.

229. P. Leonard, S. Hearty, J. Brennan, L. Dunne, J. Quinn, T. Chakraborty, and R. O'Kennedy, *Enzyme Microb. Technol.*, 2003, **32**, 3–13.

230. D. Ivnitski, I. Abdel-Hamid, P. Atanasov, and E. Wilkins, *Biosens. Bioelectron.*, 1999, **14**, 599–624.

231. M. R. J. Salton and K. S. Kim, in *Medical Microbiology*, ed. S. Baron, 4th edn., 1996.

232. W. W. Baldwin, R. Myer, T. Kung, E. Anderson, A. L. Koch, W. W. Baldwin, R. Myer, T. Kung, and E. Anderson, *J. Bacteriol.*, 1995, **177**, 235–237.

233. M. Carrera, R. O. Zandomeni, and J.-L. Sagripanti, *J. Appl. Microbiol.*, 2008, **105**, 68–77.

234. H. Bruus, *Lab Chip*, 2012, **12**, 1578–86.

235. Y. Ai, C. K. Sanders, and B. L. Marrone, *Anal. Chem.*, 2013, **85**, 9126–34.

236. S. P. Martin, R. J. Townsend, L. a Kuznetsova, K. a J. Borthwick, M. Hill, M. B. McDonnell, and W. T. Coakley, *Biosens. Bioelectron.*, 2005, **21**, 758–67.

237. B. Hammarström, B. Nilson, T. Laurell, J. Nilsson, and S. Ekström, *Anal. Chem.*, 2014.

238. J. J. Hawkes, M. S. Limaye, and W. T. Coakley, *J. Appl. Microbiol.*, 1997, **82**, 39–47.

239. H. Bruus, *Lab Chip*, 2011, **11**, 3742–51.

240. A. H. J. Yang and H. T. Soh, *Anal. Chem.*, 2012, **84**, 10756–62.

241. P. Thévoz, J. D. Adams, H. Shea, H. Bruus, and H. T. Soh, *Anal. Chem.*, 2010, **82**, 3094–8.

242. J. D. Adams and H. T. Soh, *Appl. Phys. Lett.*, 2010, **97**, 28–31.

243. A. Lenshof, A. Jamal, J. Dykes, A. Urbansky, I. Astrand-Grundström, T. Laurell, and S. Scheding, *Cytometry. A*, 2014, **85**, 933–41.

244. L. M. Johnson, L. Gao, C. W. Shields IV, M. Smith, K. Efimenko, K. Cushing, J. Genzer, and G. P. López, *J. Nanobiotechnology*, 2013, **11**, 22.

245. K. W. Cushing, M. E. Piyasena, N. J. Carroll, G. C. Maestas, B. A. López, B. S. Edwards, S. W. Graves, and G. P. López, *Anal. Chem.*, 2013, **85**, 2208–15.

246. G. R. Goddard, C. K. Sanders, J. C. Martin, G. Kaduchak, and S. W. Graves, *Anal. Chem.*, 2007, **79**, 8740–6.

247. J. J. Hawkes, R. W. Barber, D. R. Emerson, and W. T. Coakley, *Lab Chip*, 2004, **4**, 446–52.

248. Y. Liu, D. Hartono, and K.-M. Lim, *Biomicrofluidics*, 2012, **6**, 12802–1280214.

249. M. Evander, L. Johansson, T. Lilliehorn, J. Piskur, M. Lindvall, S. Johansson, M. Almqvist, T. Laurell, and J. Nilsson, *Anal. Chem.*, 2007, **79**, 2984–91.

250. M. Ohlin, A. E. Christakou, T. Frisk, B. Önfelt, and M. Wiklund, *J. Micromechanics Microengineering*, 2013, **23**, 035008.

251. B. Vanherberghen, O. Manneberg, A. Christakou, T. Frisk, M. Ohlin, H. M. Hertz, B. Önfelt, and M. Wiklund, *Lab Chip*, 2010, **10**, 2727–32.

252. A. E. Christakou, M. Ohlin, B. Vanherberghen, M. A. Khorshidi, N. Kadri, T. Frisk, M. Wiklund, and B. Önfelt, *Integr. Biol. (Camb).*, 2013, **5**, 712–9.

253. P. N. Dean, D. Pinkel, and M. L. Mendelsohn, *Biophys. J.*, 1978, **23**, 7–13.

254. S. K. Mohanty, A. Uppal, and P. K. Gupta, *Biotechnol. Lett.*, 2004, **26**, 971–974.

255. M. Ward, P. Turner, M. Dejohn, and G. Kaduchak, *Curr. Protoc. Cytom.*, 2009, **49**, 1.22.1–12.

256. T. Franke, S. Braunmüller, L. Schmid, a Wixforth, and D. a Weitz, *Lab Chip*, 2010, **10**, 789–94.

257. S. Deshmukh, Z. Brzozka, T. Laurell, and P. Augustsson, *Lab Chip*, 2014, **14**, 3394–400.

258. L. Johansson, F. Nikolajeff, S. Johansson, and S. Thorslund, *Anal. Chem.*, 2009, **81**, 5188–96.

Anal. Chem. **2009,** *81,* 6195–6200

Harmonic Microchip Acoustophoresis: A Route to Online Raw Milk Sample Precondition in Protein and Lipid Content Quality Control

Carl Grenvall,[†] Per Augustsson,[†] Jacob Riis Folkenberg,[‡] and Thomas Laurell*[,†]

Department of Electrical Measurements, Division Nanobiotechnology, Lund University, P.O. Box 118, S-221 00 Lund, Sweden, and FOSS Analytical A/S, Slangerupgade 69, DK-3400 Hillerød, Denmark

A microfluidic approach for raw milk sample preconditioning prior to protein and lipid content analysis has been developed. The system utilizes microchip acoustophoresis and is a further extension of our previously reported multiple node ultrasonic standing wave focusing platform (Grenvall, C.; Augustsson, P.; Matsuoka, H.; Laurell, T. ***Proc. Micro Total Anal. Syst.*** **2008,** ***1,*** **161−163). The microfluidic approach offers a method for rapid raw milk quality control using Fourier transform infrared spectroscopy (FT-IR). Two acoustophoresis modes are explored, $2\lambda/2$ and $3\lambda/2$, offering lipid content enrichment or depletion, respectively. Lipid content depletion above 90% was accomplished. FT-IR data on microchip-processed raw milk samples, enabling direct lipid and protein content analysis, are reported. Most importantly, the harmonic operational modes bypass the problem of lipid aggregation and subsequent clogging, inherent in $\lambda/2$ acoustophoresis systems.**

Raw milk quality control is becoming increasingly important worldwide, partly due to the fast growing industrial dairy sector in large countries like China and India, and partly due to the continuous improvements in dairy herd control and production of dairy products.

Rapid and well-established methods already exist for measuring the concentration of the most abundant solids in milk; in particular lipid, protein, and lactose. These solids determine the value of the milk as a raw material for a dairy product, and typically, the price of the traded milk is directly calculated from the lipid and protein concentrations.

In this respect, one of the main nuisances in raw milk is the presence of lipid globules, which leads to pronounced light scattering and prevents the use of conventional microscopy or spatially resolved spectroscopy for analysis. A simple method of removing the lipid particles in milk may thus be a very useful pretreatment step for microbiological analysis. Alternatively, the selective removal and concentration of the lipid globules may facilitate new methods for analyzing the detailed milk fat properties, e.g., determining the fatty acid composition, the amount of unsaturated fat, or trans fat.

Although being slow and requiring manual handling centrifugation is still a major work horse as a sample preprocessing step. Microchip-based acoustophoresis, on the other hand, has enabled new noncontact means of manipulating particles and cells in a continuous flow microfluidic format.[1−6] Acoustophoresis offers a rapid and continuous flow based mode of operation, using the acoustic standing wave forces as a gentle sample pretreatment method to reduce biocomplexity. Early work in the ultrasonic standing wave technology (USW) field of research aimed to use the acoustic radiation force for spatial handling of microparticles within the acoustic field, in different media.[7,8] Later work has reported USW as a means to discriminate between different types of bioparticles or particle size.[9,10] Previous experiences gained in acoustophoretic separation of lipid microemboli in shed blood[11,12] serve as a knowledge basis for the work reported in this paper, addressing separation requirements in other complex biofluids.

A key process step to enable milk quality control is the discrimination of the lipid emulsion in raw milk. Microchip integrated acoustophoresis has therefore in this paper been evaluated as a fundamental platform to either provide raw milk samples with depleted lipid emulsion content for further bioanalytical milk quality control or to generate concentrated lipid emulsions enabling direct FT-IR spectroscopic analysis of the lipid content.

MATERIALS AND METHODS

Channel Design. The acoustic resonator channels were fabricated according to earlier reported microfabrication process-

* To whom correspondence should be addressed.
[†] Lund University.
[‡] FOSS Analytical A/S.

(1) Grenvall, C.; Augustsson, P.; Matsuoka, H.; Laurell, T. *Proc. Micro Total Anal. Syst. 2008* **2008**, *1*, 161–163.
(2) Nilsson, A.; Petersson, F.; Jönsson, H.; Laurell, T. *Lab Chip* **2004**, *4*, 131–135.
(3) Laurell, T.; Petersson, F.; Nilsson, A. *Chem. Soc. Rev.* **2007**, *36*, 492–506.
(4) Augustsson, P.; Aberg, L. B.; Sward-Nilsson, A. M. K.; Laurell, T. *Microchim. Acta* **2009**, *164*, 269–277.
(5) Augustsson, P.; Persson, J.; Ekström, S.; Ohlin, M.; Laurell, T. *Lab Chip* **2009**, *9*, 810–818.
(6) Persson, J.; Augustsson, P.; Laurell, T.; Ohlin, M. *FEBS J.* **2008**, *275*, 5657–5666.
(7) Kundt, O. L. *Ann. Phys. Chem.* **1874**, *229*, 1–12.
(8) Weiser, M. A. H.; Apfel, R. E.; Neppiras, E. A. *Acustica* **1984**, *56*, 114–119.
(9) Kapishnikov, S.; Kantsler, V.; Steinberg, V. *J. Stat. Mech.* **2006**, P01012.
(10) Petersson, F.; Åberg, L.; Sward-Nilsson, A. M.; Laurell, T. *Anal. Chem.* **2007**, *79*, 5117–5123.
(11) Jonsson, H.; Holm, C.; Nilsson, A.; Petersson, F.; Johnsson, P.; Laurell, T. *Ann. Thorac. Surg.* **2004**, *78*, 1572–1577.
(12) Petersson, F.; Nilsson, A.; Holm, C.; Jonsson, H.; Laurell, T. *Lab Chip* **2005**, *5*, 20–22.

10.1021/ac900723q CCC: $40.75
Published on Web 07/02/2009

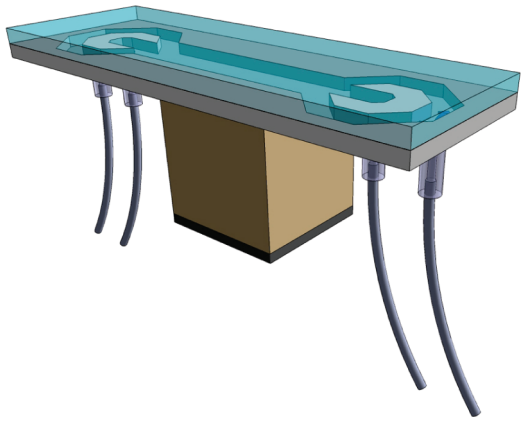

Figure 1. Schematic of the acoustic separator chip with the silicon channel visible through the glass lid, the aluminum block on the actuation side underneath the channel with the piezo crystal (dark gray) attached at the bottom. Fluidic docking ports and external tubing are also visible.

ing.[2] Two different chip designs were used, channels 150 μm deep and 23 mm long, with widths of 750 and 1125 μm, respectively. Each channel has a center inlet with a separate fluidic connection and two side inlets, which share the same fluidic connection. The same design was used for the outlets, Figure 1. The fluidic network was managed by syringe pumps (WPI sp210iwz, World Precision Instruments Inc., Sarasota, FL).

Actuation Setup. Acoustic actuation was performed with a piezo crystal (12 mm × 12 mm × 1 mm, PZ26, Ferroperm Piezoceramics AS, Kvistgard, Denmark) resonant at 2 MHz, placed underneath the microchip. An aluminum block (10 mm × 10 mm × 16 mm), placed between the piezo crystal and the microchip, act as a heat-sink when doing experiments at high driving voltages. For improved acoustic coupling ultrasound gel (Aquasonic Clear, Parker Laboratories Inc., Fairfield, NJ) was applied between the microchip and the aluminum distance and between the aluminum distance and the piezo crystal. Electronic actuation of the piezo crystal has previously been reported.[2] The mounted chip can be seen in Figure 1.

Analysis Instrumentation. To evaluate the composition of the separated fractions, two different analytical methods were used: multiangle light scattering (MALS) and (FT-IR). The FT-IR spectrometer was a prototype of OenoFoss (FOSS Analytical A/S, Hillerød, Denmark), with a spectral range of 1000−3500 cm^{-1} and a resolution of 14 cm^{-1}, equipped with a deuterated L-alanine-doped triglycene sulfate (DLATGS) pyroelectric detector. Each spectrum was obtained with an integration time of 5 s. MALS was performed with a MasterSizer X (Malvern Instruments Ltd., Malvern, U.K.) and used to determine the size distribution of particles in the liquids by measuring the angle-resolved scattering of monochromatic light incident on the sample. Since the analysis is based on the theory of Mie scattering, it is possible to quantify the amount of particles with diameters both larger and smaller than the wavelength of the light source (632.8 nm).

FT-IR provides a full absorption spectrum of the samples in the spectral range of 1000−3000 cm^{-1}, where organic molecules have unique absorption peaks due to vibrational resonances, which allow for identification and quantification. For milk, the main absorption peaks are due to CH_2 and CH_3 bonds in lipid and lactose molecules, the ester bond in lipid molecules, the amide bond in proteins, and a number of so-called "fingerprint" absorptions in the low-energy range, 1000−1500 cm^{-1}. In addition to this, very strong water absorption is observed particularly in the range of 1600−1700 cm^{-1}, which typically masks all other information in this region.

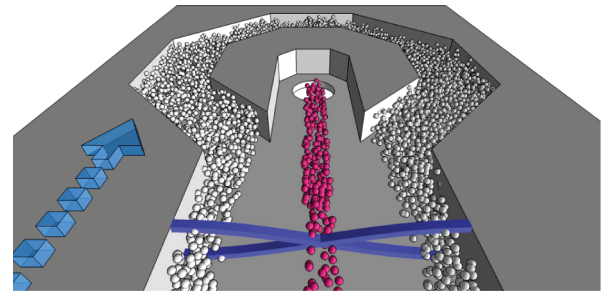

Figure 2. Schematic of original configuration for lipid microemboli separation in blood using a $\lambda/2$ separator. Lipid particles subject to an acoustic force field will focus into either the node (ϕ-positive red blood cells, red) or antinode (ϕ-negative lipid microemboli, white).

THEORY

Acoustic Force. The main driving force in acoustophoresis is the primary acoustic radiation force (PRF) that is exerted upon suspended particles in the presence of a resonant acoustic field (eq 1).[13−15] The PRF will move particles toward either the pressure nodes of the standing wave, or toward the pressure antinodes, depending on the acoustic contrast factor (ϕ-factor, eq 2) of the particles. The ϕ-factor is determined by the density and compressibility (eq 3) of the particles relative to that of the surrounding medium. Consequently, a particle with a higher density than that of the suspending medium has a tendency to move toward the pressure nodes, whereas particles of densities lower than that of the suspending medium move toward the pressure antinodes (Figure 2). Similarly, the compressibility of a particle with respect to the surrounding medium will impact the acoustic contrast factor.

$$F_r = -\left(\frac{p_0^2 V_p \beta_m \pi}{2\lambda}\right)\phi(\beta,\rho)\sin\left(\frac{4\pi x}{\lambda}\right) \quad (1)$$

where

$$\phi = \frac{5\rho_p - 2\rho_m}{2\rho_p + \rho_m} - \frac{\beta_p}{\beta_m} \quad (2)$$

and

$$\beta = \frac{1}{c^2\rho} \quad (3)$$

The parameters of eqs 1 and 2 have the following notation:

p_0, pressure amplitude;

λ, ultrasonic wavelength;

x, distance from a pressure node in the direction of the wave;

(13) Gorkov, L. P. *Sov. Phys. Dokl.* **1962**, *6*, 773–775.
(14) King, L. V. *Proc. R. Soc. London* **1934**, *147*, 29.
(15) Yosioka, K.; Kawasima, Y. *Acustica* **1955**, *5*, 167–173.

V_p, particle volume;
β_m, compressibility of the suspending medium;
β_p, compressibility of the particle;
ρ_m, density of the suspending medium;
ρ_p, density of the particle.

The particle diameter (d_p) is an important factor as the velocity of a particle in the pressure field is mainly determined by the PRF ($\propto d_p^3$) and the counteracting Stokes' drag force ($\propto d_p$).[16] Small particles thus move slower in the suspending medium compared to larger particles. Molecular material or debris will consequently not be subjected to any considerable movement in a sound field that has been properly adjusted to separate cells or lipid particles.

Lipid Emulsion Manipulation in Milk. In view of acoustophoresis as the means of depleting milk from the lipid emulsion a most straightforward approach is to employ the strategy originally pursued in lipid microemboli reduction in shed blood during cardiac surgery, Figure 2.[17] A major difference in the system composition for milk separation is the fact that the lipid content in raw milk is substantially much higher (typically 3.5−4.5%) than in shed blood processing (0.1−0.5%).[18] This fact calls for attention to increased problems of lipid emulsion trapping along the side walls of the separation channel, a phenomenon beneficial to some applications.[19] Lipid trapping along the side walls, although initially not noted, has later also been observed in blood processing after extended period of operation. Once the lipid trapping is initiated along the side walls, it rapidly accumulates at localized areas along the acoustophoresis channel, disturbing the flow profile and thus the separation efficiency. With the high lipid content in raw milk the accumulation of lipid emulsion on the side walls of the acoustophoresis channel occurs within seconds of operation at sample flow rates of 10 μL/min. Figure 3a−c shows a sequence of images taken over 30 s illustrating the initiation of lipid trapping and the further growth of the lipid aggregate. In this perspective the strategy of removing lipids by translation to the side walls of the separation channel is not a viable route for lipid emulsion separation or enrichment in raw milk quality control.

The core of the problem is that the $\lambda/2$ excitation mode of operation drives the lipids to the side walls where the flow rate is at its minimum in the channel, which in turn means that the arrival rate of lipid particles to the side walls easily becomes higher than the removal rate. As the lipid particle density builds up along the side wall some lipid vesicles also collapse and stick to the wall surface, initiating a nucleation site for the growth of a lipid constriction in the channel. Although earlier work on lipid separation in shed whole blood, at substantially lower lipid concentration than raw milk, initially did not reveal this sticking problem, lipid concentrations of several percent as the case is for raw milk becomes an immediate problem. Operation of the sample preparation chip for sufficient time, typically 10 min to collect a fraction of 100−200 μL, for subsequent FT-IR analysis was not possible.

(16) Yasuda, K.; Kamakura, T. *Appl. Phys. Lett.* **1997**, *71*, 1771–1773.
(17) Petersson, F.; Nilsson, A.; Holm, C.; Jonsson, H.; Laurell, T. *Analyst* **2004**, *129*, 938–943.
(18) Eyjolfsson, A.; Scicluna, S.; Johnsson, P.; Petersson, F.; Jonsson, H. *Ann. Thorac. Surg.* **2008**, *85*, 978–981.
(19) Hawkes, J. J.; Long, M. J.; Coakley, W. T.; McDonnell, M. B. *Biosens. Bioelectron.* **2004**, *19*, 1021–1028.

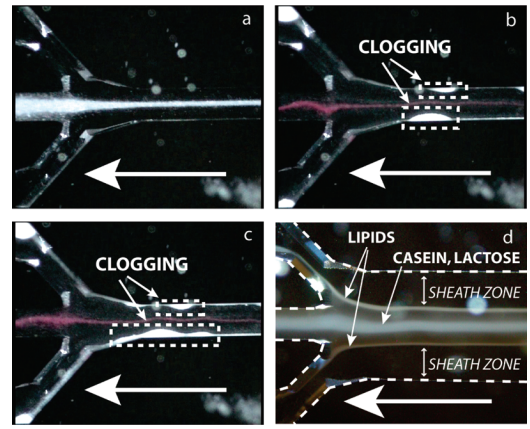

Figure 3. (a) Laminated flow of 5% lipid emulsion spiked with 1 μm polystyrene particles as model bacteria (red) leaves through the center outlet in a $\lambda/2$ wide channel; ultrasound is inactive. (b) When the ultrasound is activated, lipids start to accumulate along the side walls (white aggregates formed along the side walls) and red particles are focused to the channel center. (c) Thirty seconds after ultrasound activation the flow is erratic, and lipid clogging is severe. (d) As comparison, a 3 $\lambda/2$ wide channel with raw milk and sheath flow between the sample and the channel walls (dashed lines) shows no sign of lipid aggregation 30 min after ultrasound activation. Milk lipids go to the side outlets while casein and lactose go to the center outlet.

To avoid lipid accumulation along the side walls a system that focused the lipid emulsion in a high flow rate region was therefore designed. This can be accomplished either by operating the acoustic resonator channel at a higher harmonic of the fundamental resonance or by increasing the channel width in $\lambda/2$ steps to accommodate additional nodes and antinodes. In this paper we have investigated either 2 $\lambda/2$ or 3 $\lambda/2$ wide channels as operating modes.

Operating at the Second Harmonic (2 $\lambda/2$): Lipid Enrichment. The reason for running a system at a higher harmonic is to generate multiple nodes and antinodes in the microchannel. Exciting the resonator at a given harmonic n will produce n nodes and $n + 1$ antinodes. By utilizing hydrodynamic (sheet flow) focusing it is possible to choose a subset of these nodes and antinodes toward which particles are directed. Precise sample collection is then facilitated by adjustments to the outlet flow ratios. The possibility to choose different sheath flow media to match the current operation mode is also a benefit with this system. In lipid enrichment mode of operation the exciting frequency is set to match one acoustic wavelength across the acoustic resonance channel. In this paper a 750 μm channel was produced to allow 2 $\lambda/2$ mode of operation at the same excitation frequency, 2 MHz, and input power as used in the narrower 375 μm channel, and thus similar acoustic forces can be anticipated to drive the system. The particle suspension (raw milk) enters the channel in the center inlet with flow conditions set to sheath flow media (skimmed milk or water) laminate the particle suspension into the central one-third of the channel, Figure 4a. When particles enter the acoustic field they focus into nodes and antinodes within the one-third central channel section, in this case the center antinode with its two adjacent nodes. Lipid particles focus in the center antinode since they are prevented from reaching the side wall antinodes by the two nodes on both sides of the center antinode, which act as acoustic barriers in addition to the fluidic

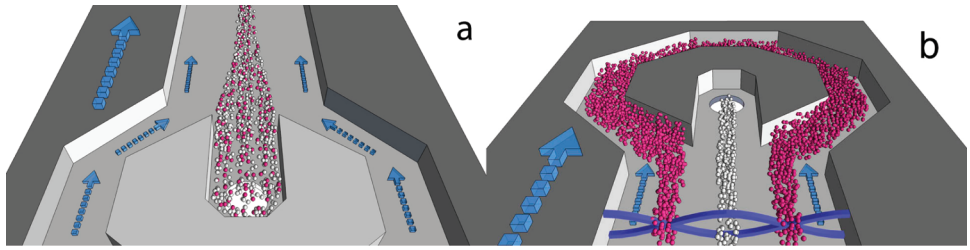

Figure 4. Schematic of lipid enrichment in raw milk using a 2 $\lambda/2$ separator. (a) Sample sheet flow configuration at the chip inlet. (b) By utilizing the 2 $\lambda/2$ channel it is possible to collect a narrow and enriched fraction of lipid particles (white) through the center outlet and a residual fraction (red) through the side outlets, thus preventing lipid particles from reaching the side walls and inducing clogging.

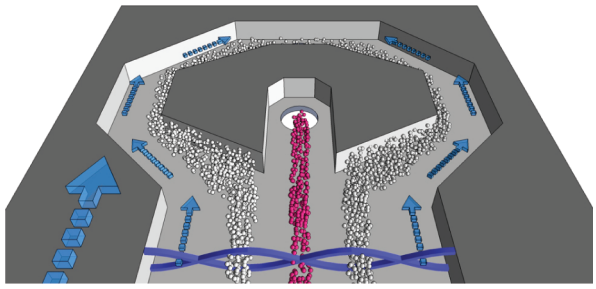

Figure 5. Schematic of lipid depletion in raw milk using a 3 $\lambda/2$ separator. By utilizing the 3 $\lambda/2$ channel it is possible to collect a narrow fraction containing dissolved species, e.g., lactose and proteins, as well as small casein particles (red) through the center outlet and a residual fraction of lipid particles (white) through the side outlets without risk of clogging. The increased distance between the virtual acoustic barriers and the side walls offers better sheath flow ratio in the 3 $\lambda/2$ channel as compared to the 2 $\lambda/2$ version.

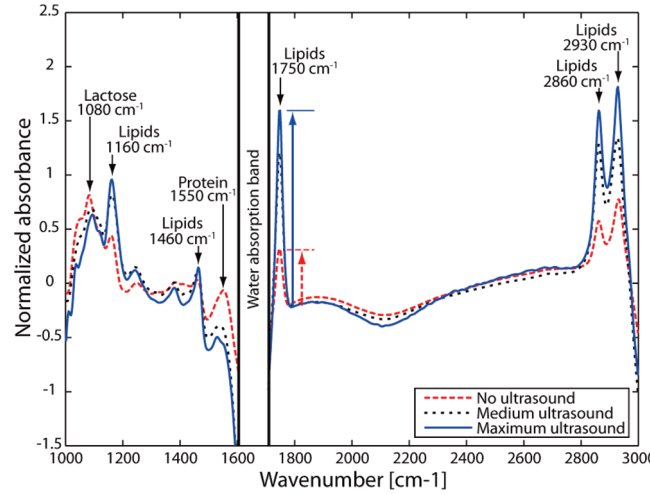

Figure 6. FT-IR spectra of the samples taken from the center outlet in lipid enrichment mode of operation (2 $\lambda/2$). The peak at 1750 cm^{-1} indicates factor 3.5 lipid enrichment with maximum ultrasound applied to the system. Increased lipid concentration prevents correct analysis of the 1550 cm^{-1} protein amide absorption peak.

barrier created by the sheath flows, Figure 4. Ideally this mode allows for extraction of all the lipids through the center outlet in a volume fraction (typically $^1/_{10}$) of the initial one-third of the channel volume, offering a substantial lipid enrichment and improved analytical conditions. Particles that focus into the nodes will simultaneously be collected in the side outlets.

Operating at the Third Harmonic (3 $\lambda/2$): Lipid Depletion. When operating the chip for lipid depletion it is more beneficial to move the larger lipid particles into the sheath flow while keeping the protein and lactose content in the center portion of the channel, thereby eliminating any dilution of this fraction. This translates into placing a pressure node in the center of the channel, and the lipid content will thus be focused into the antinodes adjacent to the channel center. In order to maintain the actuation frequency as reasoned above, a new chip was produced, having an 1125 μm wide channel which matched three half-wavelengths (3 $\lambda/2$) at 2 MHz. As in lipid enrichment mode, raw milk entered the chip through the center inlet. Sheath flows in combination with additional nodes and antinodes constrained the solid particle content of the raw milk to the channel center, Figure 5. Since lipids are now focused into the adjacent antinodes it is possible to extract a lipid depleted sample in the center outlet and collect a lipid fraction in the side outlets. Figure 3d shows a photograph of raw milk separation after 30 min of operation using the 3 $\lambda/2$ excitation mode. Lipid trapping is effectively avoided.

RESULTS AND DISCUSSION

Data 2 $\lambda/2$ Mode of Operation: Lipid Enrichment. In Figure 6, the FT-IR spectra of the emulsions taken from the center outlet are shown. Three different samples have been measured corresponding to the highest possible ultrasound amplitude (10.5 V), a lower amplitude (8.5 V), and no applied ultrasound. All spectra are normalized using an SNV function (standard normal variate) and referenced against the spectrum of pure water; thus, the ordinate values are not the physical absorbance and may, e.g., be negative. The data in the region of 1600−1700 cm^{-1} have been omitted due to the high water absorption here that causes spectral saturation.

The three spectra show a clear increase of all the spectral absorption peaks originating from the lipid molecules when the ultrasound is applied—most prominently the CH_2/CH_3 absorptions at 2860 and 2930 cm^{-1}, the −CO−O− ester linkage absorption at 1750 cm^{-1}, and the fingerprint absorptions at 1160 and 1460 cm^{-1}. The lactose concentration is estimated as the difference between the lactose peak at 1080 cm^{-1} and the background level at 1000 cm^{-1} and is practically unaffected by the application of the ultrasound.

The analysis of the protein content based on the amide absorption at 1550 cm^{-1} is complicated by the increasing absorption on the left side (lower wave numbers) due to lipids and the decreasing absorption on the right side (higher wave numbers) due to water displacement. This causes a peak shift toward lower wave numbers and a reduction of the apparent peak height. Thus, we cannot rule out a reduction of the protein content in the center outlet when the ultrasound is applied,

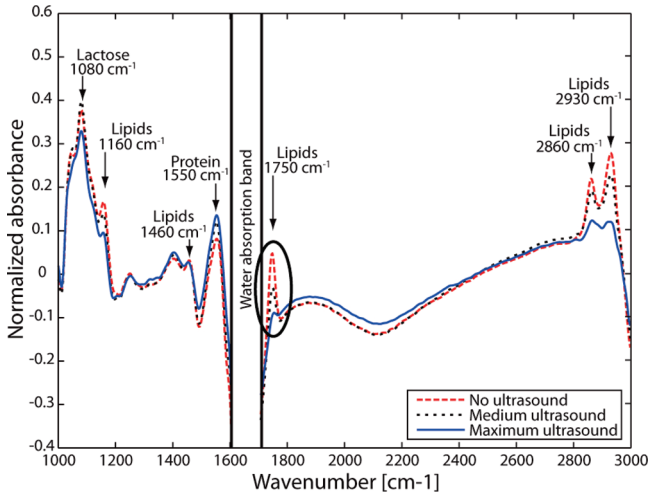

Figure 7. FT-IR spectra of the samples taken from the center outlet in lipid depletion mode of operation (3 $\lambda/2$). The lipid peak at 1750 cm^{-1} (circled) indicates significant lipid depletion when running the system with maximum ultrasound applied. The unchanged lactose and protein peaks at 1080 and 1550 cm^{-1}, respectively, suggest that the concentrations of these milk solids are virtually unaffected by the ultrasound.

but the effect is smaller than what is deduced directly from the amide peak height in the FT-IR spectra.

From the FT-IR spectra, it is concluded that the 2 $\lambda/2$ mode of operation allows a significant concentration of milk lipids in the center outlet, whereas the lactose content is practically unaffected. The increase of the peak at 1750 cm^{-1}, which is unique for lipids in milk, indicates that the lipid is concentrated by a factor of 3.5.

Data 3 $\lambda/2$ Mode of Operation: Lipid Depletion Mode. In Figure 7, the FT-IR spectra of the emulsions taken from the center outlet are shown for increasing ultrasound amplitude. Following the same analysis as for the spectra in Figure 6, it is observed that the lipid content, 1750 cm^{-1}, in the center outlet is significantly reduced as the ultrasound is increased, whereas the lactose and protein contents are practically constant, why the 3 $\lambda/2$ mode of operation is well-suited for milk sample preconditioning in protein analysis.

Figure 8a shows the MALS measurements of the particle size distribution in the center outlet for increasing ultrasound amplitude. It is noted that all distributions are normalized to a total area of 100%, and thus only the shapes can be compared, but not the absolute magnitudes. As expected the pure raw milk has the same distribution as a sample from the center outlet when no ultrasound is applied. As the ultrasound amplitude is increased two effects are noted—the peak of the distribution shifts toward smaller diameters, and a second peak centered at approximately 0.3 μm become more prominent.

The particles in the range of 1−10 μm are the lipid globules in the milk, and thus the shift of the peak toward smaller diameters show that the large lipid globules are separated more efficiently in the ultrasound field than the smaller globules. This is consistent with the larger ultrasound forces that act on large particles compared to small particles.

The particles with diameters below 1 μm are mainly casein micelles (milk protein). Light scattering due to lipid emulsions is much stronger than for casein due to the larger dielectric contrast, and thus the casein peak is not resolved in the MALS measurements until the lipid concentration is sufficiently low. The increasing casein peak is therefore consistent with the decreasing lipid contents observed in the FT-IR measurements.

In Figure 8b the particle size distribution at the highest ultrasound amplitude is compared to that of commercial skimmed milk (lipid content less than 0.1%) and low-fat milk (0.5% lipid content). The commercial milks have the same casein (protein) content and show a similar casein peak shape as the milk exposed to the ultrasound field. Thus, there is no indication that the ultrasound forces alter the size distribution of the casein micelles.

In summary, the 3 $\lambda/2$ configuration facilitates an efficient removal of lipid emulsion from milk with practically no effect on the lactose and protein composition. The lipid depletion in terms of the total concentration may be better than 90%, and for the highest ultrasound amplitude lipid particles larger than 4 μm disappear below the detection limit of MALS.

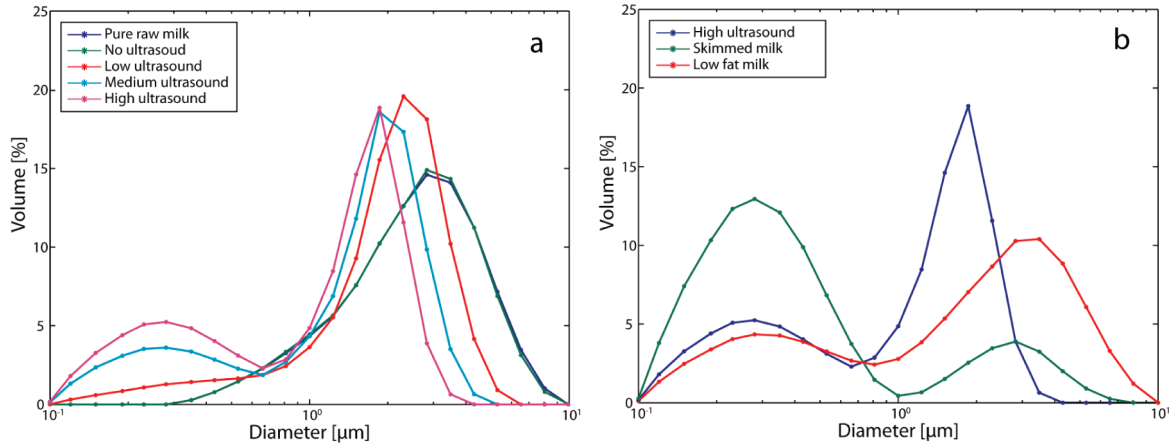

Figure 8. (a) MALS measurements of samples from the center outlet when operating the system in lipid depletion mode with varying ultrasound effects applied. All distributions are normalized; thus, only the curve shapes should be compared. A shift toward smaller fat globules can be seen as ultrasound effect increases. The casein micelle peak at ~0.3 μm is consistent with FT-IR measurements where lipids were depleted, whereas milk proteins are virtually unaffected by the ultrasound. (b) Comparisons between commercially available milk and a high ultrasound center outlet sample also suggest protein content to be unaffected by the ultrasound.

CONCLUSIONS

This paper demonstrates that multinodal acoustophoretic operation in continuous flow separation of milk constituents avoids the problem of side wall lipid particle adhesion and subsequent clogging. Two modes of acoustophoretic operation have been investigated offering either lipid enrichment or depletion, where the $2\,\lambda/2$ acoustophoresis mode opens the route to improved analytical conditions for lipid content analysis in milk sample quality control and the $3\,\lambda/2$ mode of operation displays excellent raw milk sample preconditioning for protein analysis. Further work will focus on integration of the proposed raw milk sample preparation with analytical instrumentation for milk quality control.

ACKNOWLEDGMENT

Vinnova programme Multidisciplinary Bio, Swedish Research Council, Royal Physiographic Society in Lund, Crafoord Foundation, and Carl Trygger Foundation are acknowledged for their support.

Received for review April 5, 2009. Accepted June 10, 2009.

AC900723Q

ORIGINAL ARTICLE

Cytometry PART A
Journal of the International Society for Advancement of Cytometry

Label-Free Somatic Cell Cytometry in Raw Milk Using Acoustophoresis

Carl Grenvall,[1]* Jacob Riis Folkenberg,[2] Per Augustsson,[1] Thomas Laurell[1,3]

[1]Department of Measurement Technology and Industrial Electrical Engineering, Lund University, Sweden

[2]FOSS Analytical A/S, Denmark

[3]Department of Biomedical Engineering, Dongguk University, Seoul, Korea

Received 3 July 2012; Revision Received 6 September 2012; Accepted 14 September 2012

Grant sponsor: FOSS A/S, FORMAS Tvärlivs, VINNOVA IFFH CellCARE, Swedish Research Council, Stiftelsen Olle Engkvist Byggmästare;

*Correspondence to: Carl Grenvall, Lunds Universitet, Elektrisk Mätteknik, Box 118, 221 00, Lund.

Email: carl.grenvall@elmat.lth.se

Published online 18 October 2012 in Wiley Online Library (wileyonlinelibrary.com)

DOI: 10.1002/cyto.a.22214

Abstract

A microfluidic system for cell enumeration in raw milk was developed. The new method, preconditions the milk sample using acoustophoresis that removes lipid particles which are larger than a few micrometers. The acoustophoretic preprocessing eliminates the need for conventional sample preparation techniques, which include chemical solvents, cell labeling and centrifugation, and facilitates rapid cell enumeration using microscopy or coulter counter measurements. By introducing an acoustic standing wave with three pressure nodes in a microchannel at the same time as the milk sample is laminated to the channel center, lipids are acoustically driven to the closest pressure antinode at each side of the channel center and the cells in the milk sample are focused in the central pressure node. The extracted center fraction with cells becomes sufficiently clean from lipid vesicles to enable enumeration of somatic cells without any labeling step either by direct light microscopy or by coulter counting. Obtained lipid free milk fractions clearly revealed the cell fraction when analyzed by Coulter Counting. Cell counting as measured by a Coulter Counter after acoustophoretic lipid depletion aligned with the corresponding data obtained by reference measurements based on fluorescence staining and subsequent flow cytometer analysis. © 2012 International Society for Advancement of Cytometry

Key terms

milk; acoustophoresis; ultrasound; somatic cell count; label free; microfluidic chip

CELL enumeration in biological field samples is often labor intense, requiring substantial sample pretreatment prior to analysis. As opposed to laboratory samples, there are typically a much larger number of non cellular particles in field samples that potentially interfere with cell counting instruments, regardless of the chosen technology platform. One example of such a sample is raw milk, where the number of somatic cells is an important indicator of the health status of the cow, specifically the mammary gland, which directly affects milk yield and quality (1). High somatic cell count (SCC, somatic cells/ml milk) is often a result of mastitis, an inflammation in the mammary gland. Common mastitis-causing organisms include *Staphylococcus aureus*, *Staphylococcus epidermis*, *Escherichia coli* and different streptococci, typically transmitted during milking by contact to contaminated milking machines, hands, or equipment. As part of the inflammatory response the number of leukocytes increases, from $\sim 10^5$ in an uninfected cow and $\sim 3 \times 10^5$ during subclinical mastitis to several millions during clinical mastitis, leading to an elevated SCC. Milk with an SCC of $>4 \times 10^5$ is deemed unfit for human consumption in the European Union while slightly higher levels are permitted in the United States (the State of Indiana has a 10^6 SCC limit). Mastitis has adverse effects on total yield and quality of milk. Levels of casein and lactose decrease while levels of proteolytic enzymes from bacteria, lipase enzymes from the leukocytes and activated plasmin from blood all increase. More precisely, the result of the infection is lower milk and cheese yields, poor curding, bitter taste, and lower shelf life even after pasteurization. Thus it is important to rapidly identify infected animals to stop further spreading of the pathogens, treat the infected

ISAC International Society for Advancement of Cytometry

animals with minimal amounts of drugs, of which no residues are permitted in milk, and, in the end, maximize milk yield and quality (2,3).

Raw milk samples may be contaminated with medium sized objects such as grains of sand, parts of insects, or pieces of hair that can be easily removed with filters. However, even without these contaminants the multitude of lipid particles with sizes identical to the somatic cells (diameters 7–10 μm) will prevent the use of simple technologies like microscopy or coulter counting for cell enumeration. Instead, flow cytometry is commonly used, which alleviates the problem of erroneous cell enumeration. Flow cytometry, however, requires several steps of manual sample processing, including fluorescent staining of the cells in the sample and is commonly followed by centrifugation based wash steps prior to introduction in the cytometry instrument. Alternatively, the raw milk samples can be centrifuged and the precipitate resuspended and analyzed in a Coulter counter or by staining cells and manually counting cells in sample smears (4–10).

With the emerging possibilities of microfluidic systems, it is relevant to investigate compatible technologies that would allow integration of raw milk analysis on a single chip. Recently, it was demonstrated that lipid particles can be efficiently removed from raw milk samples using acoustophoresis to allow direct protein and lipid content analysis (11). In this report, we demonstrate how a combination of acoustophoresis and conventional Coulter Counting or phase contrast microscopy can be used to count the number of somatic cells in raw milk samples, using only an isotonic solution of NaCl as additional buffer.

Materials and Methods

Microfluidic System

The principle of using acoustic standing wave forces for particle manipulation has been well researched and in the past decade a transition to a chip integrated microfluidic format has gained attention (12–15). In acoustophoresis, the primary acoustic radiation force F_{rad} [Eq. (1)] is utilized to focus particles into either nodes or antinodes according to their acoustic contrast factor Φ [Eq. (2)], which is dependent on the density and compressibility of the particles compared to the surrounding medium. Studies have shown that ultrasonic cell manipulation in microfluidic systems are gentle to cells (16,17). Dense particles (i.e., cells) tend to have a positive contrast factor in most commonly used flow media including water, and they, consequently, focus into the acoustic pressure nodes. Less-dense particles (i.e., lipids) have a negative contrast factor and thus focus into pressure antinodes. The primary acoustic radiation force scales linearly with an increased contrast factor, Φ, and the particle volume, a^3, and for a polystyrene particle of diameter 10 μm the highest achievable force to date is $\sim$100 pN corresponding to an acoustophoretic velocity of 1,000 μm s^{-1}.

$$\text{Primary acoustic radiation force: } F_{rad} = 4\pi a^3 \Phi k_y E_{ac} \sin(2k_y y) \quad (1)$$

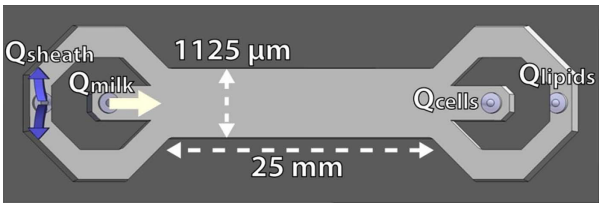

Figure 1. Schematic top view of the microfluidic channel (not to scale). Trifurcations at both ends with connected sides simplify the fluidic setup. [Color figure can be viewed in the online issue which is available at wileyonlinelibrary.com]

where

$$\text{Acoustic contrast factor: } \Phi = \frac{\kappa_o - \kappa_p}{3\kappa_o} + \frac{\rho_p - \rho_o}{2\rho_p + \rho_o} \quad (2)$$

and a ($\approx$10 μm) is the particle radius, Φ is the acoustic contrast factor, $k_y = 2\pi/\lambda$ is the wave vector, E_{ac} ($\approx$100 J m^{-3}) is the acoustic energy density, y is the distance from the wall, κ_p ($\approx 2.5 \times 10^{-10}$ Pa^{-1}) is the isothermal compressibility of the particle, κ_o ($\approx 5 \times 10^{-10}$ Pa^{-1}) is the isothermal compressibility of the fluid, ρ_p ($\approx$1,030 kg m^{-3}) is the density of the particle (cell) and ρ_o ($\approx$1,000 kg m^{-3}) is the density of the fluid.

To enable efficient lipid removal from raw milk samples, an acoustically resonating microfluidic chip was fabricated in silicon with an anodically bonded glass lid (11,13). The acoustophoresis channel was 25-mm long, having a width of 1,125 μm and a depth of 150 μm, as shown in Figure 1. The channel was provided with trifurcation inlets and outlets, each with a separate fluidic connection for the center flow and a common fluidic connection for the two side flows.

Four syringe pumps (WPI sp210iwz, World Precision Instruments, Sarasota, FL) were used to control the flows, sheath inlet (Q_{sheath}), sample inlet (Q_{milk}), side outlet (Q_{lipids}), and center outlet (Q_{cells}). Samples were collected using loop valves (V-451, IDEX Health and Science LLC, Oak Harbor, WA) with a sample volume of 100 μl. During sampling a volume corresponding to three times the loop volume was allowed to flow through the loop.

Sample and buffer syringes, 1 ml at the centers and 10 ml at the sides, (BD Plastipak, Becton Dickinson, Franklin Lakes, NJ) were connected to the flow chip using Teflon tubing (TFE Teflon tubing 58697-U, Supelco, Bellefonte, PA) and PEEK luer slip connectors (P-659 and F-120X, Upchurch Scientific, Oak Harbor, WA). Silicone tubing glued around inlets and outlets at the bottom of the chip constituted fluidic docking ports into which the Teflon tubes were pushed to fit tightly. To avoid sedimentation of the somatic cells, a Teflon encapsulated magnet was placed in the sample syringe and continuously moved during the experiments by a magnet stirrer.

Acoustic actuation of the channel was performed with a piezoelectric transducer ($12 \times 12 \times 1$ mm^3, PZ26, Ferroperm Piezoceramics AS, Kvistgard, Denmark). The transducer was glued to the bottom of an aluminum block, Figure 2. To ensure good ultrasound coupling, an ultrasound gel (Aquasonic Clear, Parker Laboratories, Fairfield, NJ) was applied

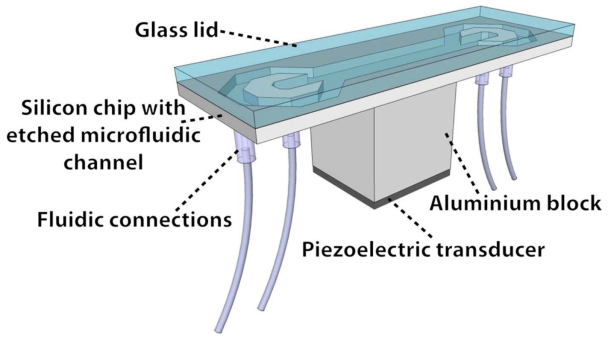

Figure 2. A complete chip with bonded glass lid, fluidic connections and piezoelectric transducer which is glued underneath the aluminum block. The aluminum block was glued to the silicon chip and acted as a heat sink for the transducer. [Color figure can be viewed in the online issue which is available at wileyonlinelibrary.com]

between the chip and the aluminum tip. An acoustic frequency of 1.970 MHz, corresponding to three half acoustic wavelengths across the channel, with a 30 kHz modulation (FM) was used. The aluminum block acted as a heat sink. The frequency modulation prevented acoustic hot spot formation.

The piezoelectric transducer was actuated by a signal generator (HP 33220A, Hewlett-Packard, Palo Alto, CA) and an RF-amplifier (75A250A, Amplifier Research, Souderton, PA). The total amplification from the function generator to the output of the RF-amplifier is nominally 30 dB, but due to an impedance mismatch typically half of the power is reflected from the transducer. The assembly of the flow chip and ultrasound transducer was placed under a microscope, and imaged during the separation process. The complete system can be seen in Figure 3.

Label-Free Analysis

As the aim of the project is to provide label free detection and counting of cells, thus eliminating the need for chemicals used to dissolve lipids and stain cells in conventional cell enumeration, several techniques were employed to investigate the samples. Original sample cell numbers were analyzed using a flow cytometer (Fossomatic FC, FOSS Analytical A/S, Hillerød, Denmark). Protein and lactose concentrations were measured to verify that the raw milk samples used were typical in composition. Collected samples after acoustophoresis treatment were then analyzed using microscopy as well as Coulter counting (Multisizer 3, Beckman Coulter, Brea, CA) and flow cytometry (BD FACS Canto, Becton Dickinson, Franklin Lakes, NJ). Cells were labeled by adding staining solution (Fossomatic staining, FOSS Analytical A/S, Hillerød, Denmark) 1:20 to the raw milk at room temperature, stirring the sample and letting it sit for a few minutes. The microscope inspection was carried out by alternating between phase contrast and fluorescent mode to verify that objects thought to be cells really were somatic cells and not false positives. In fluorescent mode a mercury lamp (Osram HBO, Osram AG, Munich, Germany) was used in combination with a 520-550 nm excitation, 565 nm mirror and 580 nm emission filter cube (UMWIG-2, Olympus, Hamburg, Germany). Samples from a chip with the ultrasound turned off were inspected using the same protocols to further illustrate the difficulties encountered when trying to count cells in samples with normal lipid content concentrations. Samples were all left to rest for a few minutes before observation in the microscope to allow somatic cells to sink to the bottom and lipid vesicles to float to the top of the observation chamber.

Acoustic Power and Flow Control Optimization

A well-defined flow in the channel is a prerequisite for efficient separation of lipids from the raw milk sample while losing only a minor fraction of the cells. With the present choice of flow rates and acoustic operation the lipid particles, having a lower density than both milk serum and water, were extracted from the sample stream and focused in the two antinodes immediately at either side of the channel center, Figure 4. Because the cells have a higher density and speed of sound (i.e., $\Phi > 0$) than the milk serum, they were focused into the center node and remained in the milk serum, and thus the lipids were separated from the milk by balancing the flow rates at the chip outlet.

It is preferable to maximize the acoustic force that particles are exposed to in the channel since this allows even low contrast (Φ) as well as small lipid particles to separate. With a fixed channel length the total lateral displacement of particles may be increased by lowering the flow rate, thus increasing particle exposure time in the acoustic field, or by an increase in acoustic power input. At low flow rates or high acoustic power, lipid particles, reported in our earlier work (11), tended to accumulate along the channel walls. The current three node design now addresses these problems and allows lower flow rates (or a higher acoustic power). By introducing three acoustic nodes into the system and using sheath flow to laminate the milk sample into less than one-third of the total channel width in the channel center, the two side nodes act as acoustic barriers that prevent lipids from travelling further into the sheath fluid and reaching the channel walls. However, at very low flow rates, the lipids can still be trapped in hot

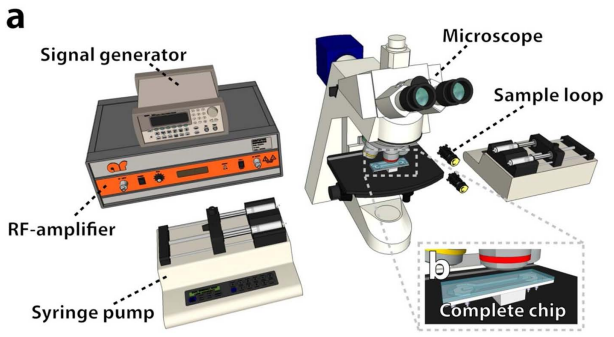

Figure 3. A schematic of the experimental setup. (**a**) Raw milk and sheath liquid were injected into the chip with the left syringe pump and then withdrawn through the sample loops (visible as black/yellow tubes) into the right hand side pump. (**b**) The insert shows the chip underneath the microscope lens. A custom-made holder allows the fluidic connections and acoustic connections to fit in the XY-stage. [Color figure can be viewed in the online issue which is available at wileyonlinelibrary.com]

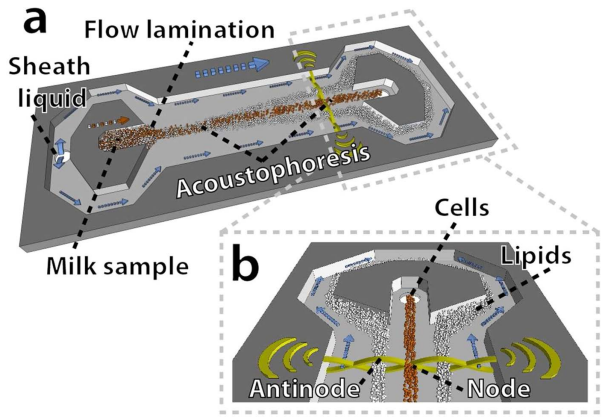

Figure 4. By combining the inherent laminar properties of microfluidic channels with the different acoustic properties of milk components it is possible to achieve a binary separation between lipids (white) and somatic cells (brownish). (**a**) Sheath liquid (water) enters the main channel from the sides and laminates the raw milk sample to the center flow lane of the channel. (**b**) The acoustic radiation force translates the lipid content into the antinodes while simultaneously focusing the somatic cells in the channel center. By using a triple node system in combination with sheath flows lipids are prevented from reaching and aggregating at the channel walls (11). [Color figure can be viewed in the online issue which is available at wileyonlinelibrary.com]

spots at the trifurcation zone of the inlet and outlet channels as illustrated in Figure 5.

When lipids aggregate at the inlet trifurcation the flow and separation becomes asymmetric. Typically, large lumps of lipids are also released from the first aggregate at an irregular rate, which prevents optimal separation. Likewise, if lipid lumps build up at the outlet trifurcation the side outlets may become partially blocked, causing flow disturbances where some of the lipids flow into the center outlet and some of the cells flow into the opposite side outlet.

Observations show a strong correlation between lipid aggregation and the loss of cells during separation. It is also believed that the lipid lumps tend to trap some of the cells, which cause even worse separation when these cells are transported with the lumps into the waste outlet. A similar phenomenon is observed when milk is centrifuged—although the cells are heavier than the milk serum, a significant fraction of the cells are trapped in the lipid layer at the top.

To avoid lipid aggregation while maintaining good separation and throughput, the system was investigated at varying transducer actuation voltages and flow rate settings. With the transducer actuated at 30 V, corresponding to a maximum force of ~100 pN acting on a 9 μm particle, lipids started to aggregate even at flow speeds of 500 μl min^{-1}. This might be because the no-slip conditions at the channel top and bottom will cause lipids to aggregate there at relatively high acoustic settings. At 20–25 V actuation, corresponding to ~50–75 pN force, separation was stable and no lipid aggregation occurred.

Taking these inherent system properties into consideration, transducer actuation was set to 22 V and microfluidic conditions set to Q_{sheath} = 420 μL min^{-1}, Q_{sample} = 30 μL min^{-1}, Q_{cell} = 60 μL min^{-1}, and Q_{waste} = 390 μL min^{-1}. These settings facilitate symmetric and stable separation of the lipid particles into bands that flow into the side outlets, as shown in Figure 6. Cell-sized particles will be subject to a maximum acoustic force of ~25–50 pN at this acoustic setting. A center outlet flow of 60 μL min^{-1}, result in samples that consist of 50% milk and 50% sheath liquid when no ultrasound is applied (later visible in measurements, Figure 10b). An isotonic solution of NaCl in deionized water (9 g NaCl added to 1 L Milli-Q water) was used for the sheath liquid, such that the mixing of sample and sheath liquid does not change the liquid osmolality.

Results and Discussion

FTIR Analysis

To quantify the lipid depletion efficiency of the system, an FTIR spectrum was obtained from a center outlet sample, with ultrasound active as well as inactive. The result of a representative measurement is shown in Figure 7, where the ester

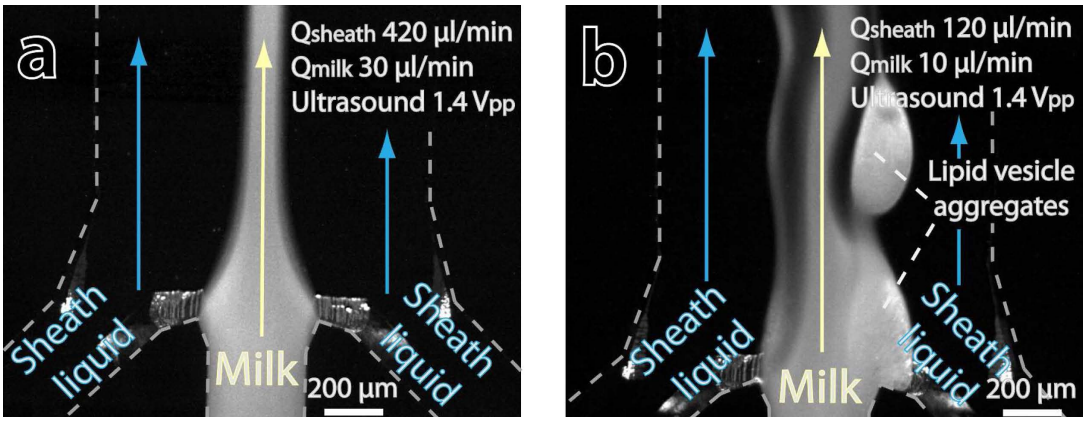

Figure 5. Microscope images of the sample and sheath liquid flow at the inlet side of the channel for two different settings of flow rates. (**a**) When the chip is operated at the flow rates and acoustic power used in the experiments presented herein, no lipid aggregation occurs. (**b**) However, at lower flow rates lipids start to aggregate/trap at the trifurcation branch as well as further down the channel (top-bottom aggregation). It should be noted that with a conventional single node channel lipid aggregation would occur even at higher flow rates, see (11). [Color figure can be viewed in the online issue which is available at wileyonlinelibrary.com]

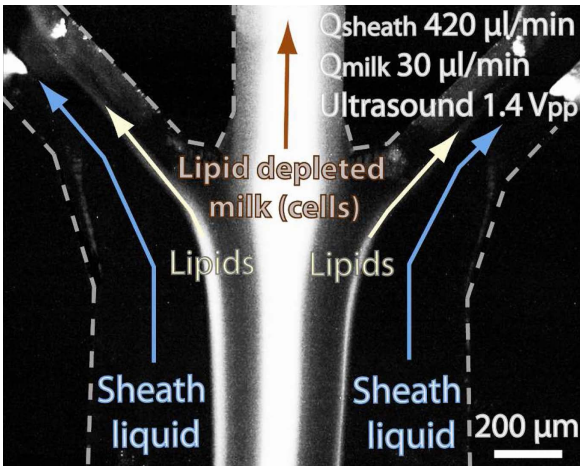

Figure 6. The figure shows the flow at the outlet side of the channel during acoustophoretic lipid separation from milk. The larger lipid particles are separated symmetrically into two bands that flow into the side outlets, while the milk constituents flow into the center outlet. The broader central band of light scattering casein micelles and small lipid particles visualizes the lipid depleted milk stream. [Color figure can be viewed in the online issue which is available at wileyonlinelibrary.com]

linkage peak at 1,750 cm^{-1} (dashed circle) indicates a factor 6 in lipid depletion. This aligns with our previously reported experiments, which had longer acoustic exposure times, thus resulting in higher depletion rates (11). Most important, though, is that the removed lipid vesicles composed the larger size fraction as measured by Coulter counting and multiangle light scattering. The data suggest that sufficient amounts of lipid vesicles in the size range of cells have been removed to enable label free somatic cell detection.

Phase Contrast Microscopy

Center outlet samples with ultrasound active and inactive were collected, and phase contrast as well as fluorescence microscopy were used to investigate the feasibility of label free somatic cell detection in acoustophoretically preprocessed samples. The top of the observation chamber was imaged in phase contrast mode and the bottom in both phase contrast and fluorescent mode. Figure 8 shows the schematic set-up for imaging the two samples, where a thick layer of lipid vesicles were observed floating at the top of the observation chamber for the untreated sample, Figure 8a, whereas the acoustophoretically "polished" milk sample displayed a significant reduction of interfering lipid vesicles, Figure 8b. The corresponding microscope images are seen in Figures 9a and 9d, respectively.

When focusing at the chamber bottom in the treated sample, it was possible to discern somatic cells, Figure 9e. This was not possible in the untreated sample due to lipid vesicles obscuring the cells. It can also be noted that the untreated sample displayed some larger lipid vesicles that can be mistaken for a cell, marked as "false cell," Figure 9b. When switching to fluorescent mode, it was possible to observe the cells in both samples, Figures 9c and 9f. Comparisons between phase contrast and fluorescent images revealed the "false cells."

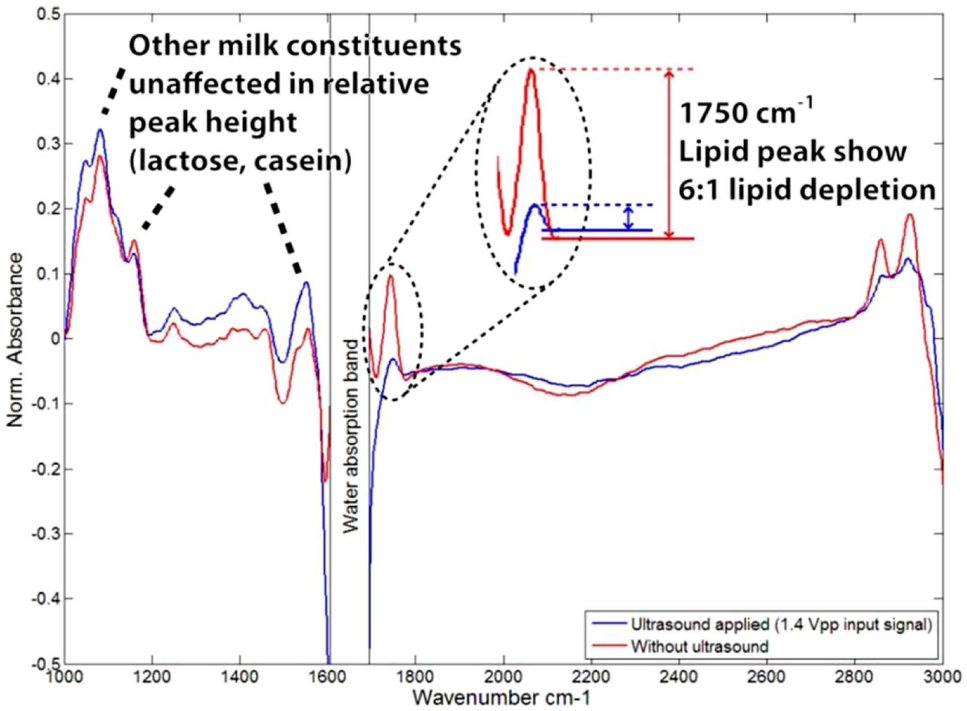

Figure 7. FTIR spectrum of the sample collected from the center outlet, with and without the ultrasound applied. The peak at 1,750 cm^{-1} (dashed circle) originates from the C−O−C ester linkage bond, and is a measure of the lipid content in the milk. The measurement show a factor of 6 in lipid depletion of the treated sample (blue) compared to the untreated sample (red). [Color figure can be viewed in the online issue which is available at wileyonlinelibrary.com]

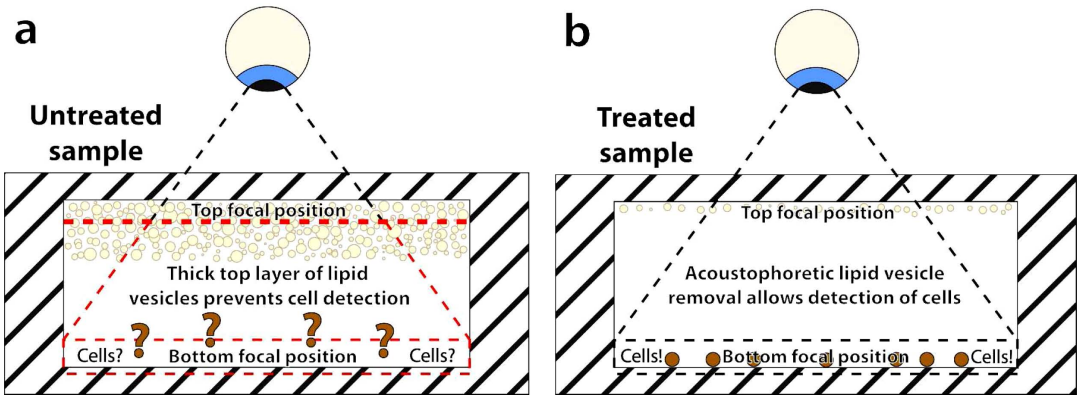

Figure 8. Schematic cross section of the observation chamber. Chamber top and bottom illustrate the focal position in Figure 9 (top illustrates Figs. 9a and 9d and bottom Figs. 9b, 9c, 9e, and 9f). (**a**) It is not possible to detect unlabeled cells in an untreated sample due to the high amounts of lipid vesicles in the sample. (**b**) When using acoustophoresis to deplete the sample from lipids, cells can be detected without any need for labeling. [Color figure can be viewed in the online issue which is available at wileyonlinelibrary.com]

This finding opens the route to the development of automated image analysis as a detection mode for somatic cell counting in raw milk without elaborate chemical preprocessing protocols.

Coulter Counting

The quantitative agreement between the SCCs obtained by the manual procedure using cell staining, centrifugation and flow cytometry, and the new proposed method (acoustophoresis in combination with Coulter counting) was investigated. Samples from three cows suffering from mastitis were analyzed using both techniques. The resulting SCCs for each sample are shown in Table 1 together with Coulter counter data for untreated samples.

Treated samples were also compared to centrifuged samples as well as untreated raw samples using Coulter counting, Figure 10. In the raw samples (solid green line), it was not possible to distinguish cells from lipid vesicles due to the

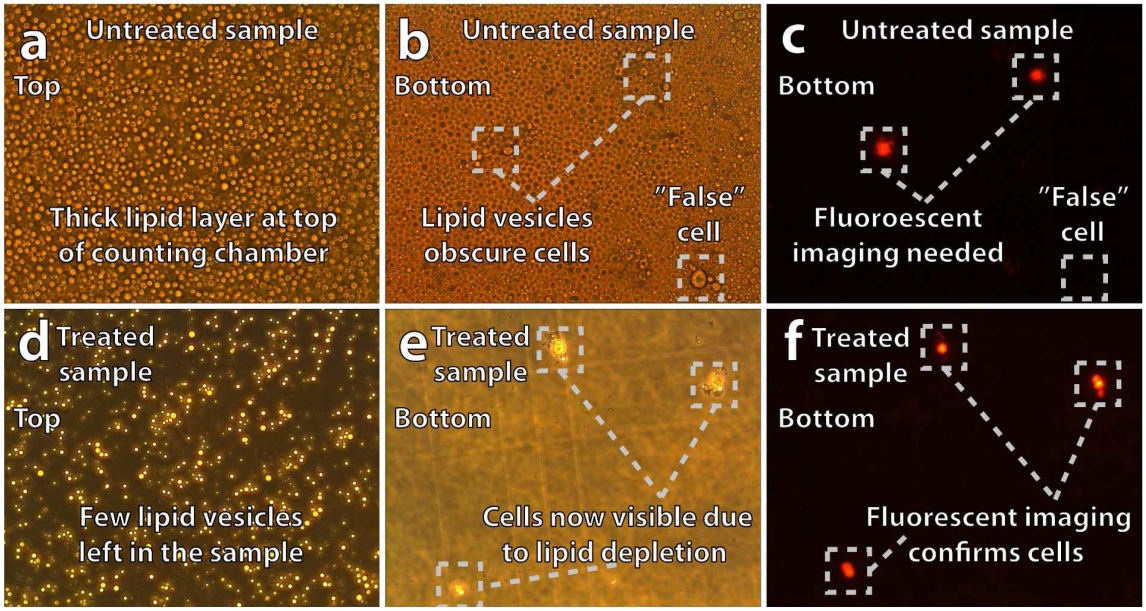

Figure 9. **a—c**, show microscope images of an untreated sample taken at different focal depths as outlined in Figure 8a. (**d—f**), show the corresponding images of an acoustophoretically pretreated sample, as outlined in Figure 8b. (a) When focusing on the top of the observation chamber in an untreated sample, a thick layer of lipid vesicles was seen. By focusing at the bottom of the chamber and then alternating between phase contrast and fluorescent imaging modes, we observed that the lipid vesicles obscured the somatic cells. Also, lipid vesicles form ''false cell'' aggregates (dashed insert square), b and c. When focusing on the top of a treated sample, and comparing to an untreated sample, the efficiency of the lipid removal becomes apparent (a vs. d). In a treated sample the cells can be clearly seen at the chamber bottom in phase contrast mode (e). When switching to fluorescent mode the visually observed cells in (e) were also confirmed (f). [Color figure can be viewed in the online issue which is available at wileyonlinelibrary.com]

Table 1. Raw milk measurements

RAW MILK SAMPLE NO.	TRADITIONAL FLOW CYTOMETRY SCC (CELLS/ML RAW MILK)	TREATED SAMPLE CC SCC (NO. OF 7.2–10.5 μM PARTICLES/ML)	UNTREATED SAMPLE CC SCC (NO. OF 7.2–10.5 μM PARTICLES/ML)
1.	4.03×10^6	3.93×10^6 (2% error)	12.06×10^6 (199% error)
2.	0.97×10^6	1.22×10^6 (26% error)	3.25×10^6 (235% error)
3.	5.76×10^6	5.73×10^6 (1% error)	8.27×10^6 (46% error)

overlapping size distribution. However, in the acoustophoretically treated samples, a cell peak (solid black line) centered at ~8.6 μm diameter emerged once the lipids were removed. Comparisons with centrifuged samples and standard fluorescent flow cytometry confirmed that the peak consisted of somatic cells. The acoustically treated sample has a slightly higher particle count as compared to the centrifuged sample (solid yellow line), indicating a non complete removal of all lipid vesicles in the cell size regime, Figure 10a. Samples passing through the microchip with the ultrasound turned off, as well as samples left in the inlet syringe, were unaffected, except for a 1:2 dilution in the chip sample which corresponds to the sheath liquid/milk ratio in the center outlet, cf. solid green line vs. solid yellow and blue lines Figure 10b.

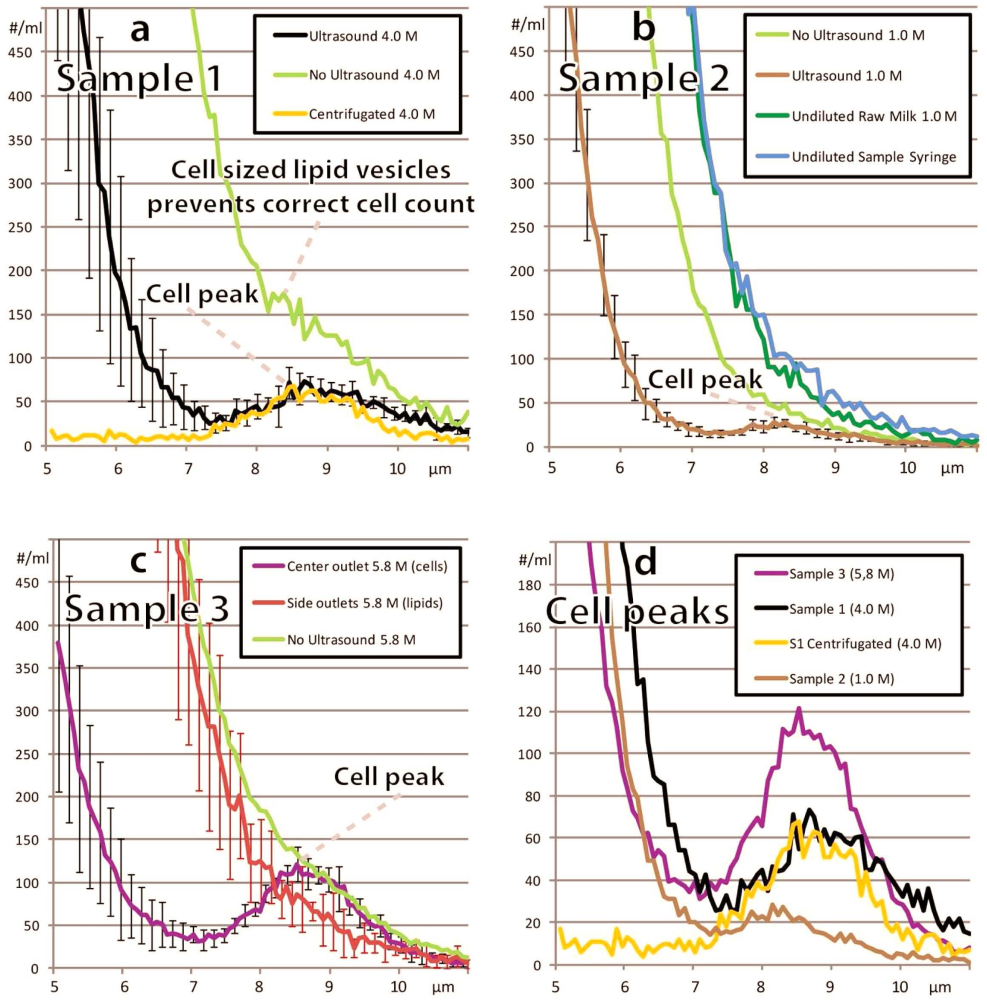

Figure 10. Relative cell counts from Coulter measurements of the three raw milk samples (1.0, 4.0, and 5.8 M SC mL^{-1}). Graph (**a**) compares acoustophoretically treated, untreated and centrifuged samples of sample 1 ($n = 4$). Graph (**b**) shows that cells even in the lowest SCC sample 2 ($n = 5$) can be seen (cell peak emerges). It also shows that samples are unaffected, except for 1:2 dilution, when run in the system with the ultrasound turned off (blue and dark green lines vs. light green line). Graph (**c**) shows both center and side outlets for sample 3 ($n = 5$) to illustrate more stable cell counts compared to lipid vesicle counts (smaller error bars for cell sized particles). Graph (**d**) shows how the Coulter measurements of treated samples scales according to the flow cytometry data with the 970 SC μL^{-1} (1.0 M, black line) sample having a peak that is ~1/6 of the 5,758 SC μL^{-1} (5.8 M, purple line) sample. [Color figure can be viewed in the online issue which is available at wileyonlinelibrary.com]

The different milk samples that were treated acoustophoretically, suggest a good correlation between the Coulter counter cell data in these samples. The number of cells also corresponded well with the values measured with traditional flow cytometry using a Fossomatic FC+ instrument (a sample of ~2.5 mL raw milk was mixed with an Ethidium bromide based staining agent, surrounded by a sheath liquid and then passed through a flow cell in which fluorescent flow cytometry was performed by detecting emitted light from stained cells using a laser and a photomultiplier tube). For example, in sample 2 the flow cytometer measurement indicated 0.97×10^6 SC mL^{-1} whereas the corresponding mean number of particles in the cell-peak region 7.2–10.5 μm, as measured by Coulter counting was 1.27×10^6 SC mL^{-1} Figure 10b. It can be noted that without the acoustic pretreatment of the sample the corresponding Coulter counter data indicated 3.25×10^6 SC mL^{-1}. A number totally dominated by the lipid vesicles. The respective data for sample 1 and 3 are also shown in Table 1. The relative deviation in flow cytometry cell count and Coulter counter data averaged 10% (2, 26, and 1%, respectively). A reason for the deviation between flow cytometry data and particle numbers obtained by Coulter counting is that the high amount of lipid vesicles compared to cells makes the system sensitive to fluidic imbalance, i.e., a minor flow disturbance may cause leakage of lipid vesicles into the center outlet and thus generate an over estimation of the somatic cell count. The cases where the cell counts actually was lower by means of Coulter counting versus flow cytometry, may be explained by the fact that samples with a significant number of cells having lipid vesicles adhering to the cell membrane may be deflected into the lipid fraction. Although these values suggest that the current setup might not be suited for exact SCC counts, it can still be used as a fast indicator of healthy or diseased live stock, not requiring elaborate chemical sample processing.

Conclusion

Acoustic focusing of cells in flow cytometry has already entered the market in the recently launched Attune® flow cytometer (Life Technologies, Carlsbad, CA) and have demonstrated valuable improvements in sample throughput and simplified sample processing. Presumably these benefits could also be harvested in the application of somatic cell counting in milk. The work presented herein, however, aims at taking, acoustic sample handling one step further in an effort to move away from flow cytometry as the analytical platform and rather pave the way to imaging cytometry at microchip level offering a less complex route forward to the next generation somatic cell counting systems in the dairy industry.

In this perspective the reported phase contrast microscopy images of raw milk samples after lipid depletion using acoustophoresis, demonstrates a simple strategy to the development of a system for somatic cell counting in raw milk, using automated image analysis without elaborate lipid solvation and cell staining preprocessing protocols. The ability to discern a "cell peak" in all samples including the one with 0.97×10^6 SC mL^{-1}, Figure 10b, indicates that it may be possible to detect early stages of mastitis (current thresholds advocate cut-offs between healthy and sick live stock at between 1 and 5×10^6 SC mL^{-1} with cows typically reaching 0.97×10^6 SC mL^{-1} after 2–3 days of inflammation). Comparisons with conventional methods as well as the correct ratio between the three samples that were analyzed using flow cytometry demonstrates that the method is able to quantify somatic cell counts in raw milk within an approximate accuracy of 10%. This opens the route to a possible integration of a Coulter counter unit on chip. Coulter counters integrated with micro fluid systems have been reported previously (18–21) and on-going work in our group now targets the development of a microfluidic system with integrated acoustophoretic and Coulter counter functionality.

Literature Cited

1. Schukken YH, Wilson DJ, Welcome F, Garrison-Tikofsky L, Gonzalez RN. Monitoring udder health and milk quality using somatic cell counts. Veterinary Res 2003;34:579–596.
2. Auldist MJ, Hubble IB. Effects of mastitis on raw milk and dairy products. Aust J Dairy Technol 1998;53:28–36.
3. Ma Y, Ryan C, Barbano DM, Galton DM, Rudan MA, Boor KJ. Effects of somatic cell count on quality and shelf-life of pasteurized fluid milk. J Dairy Sci 2000;83:264–274.
4. Viguier C, Arora S, Gilmartin N, Welbeck K, O'Kennedy R. Mastitis detection: Current trends and future perspectives. Trends Biotechnol 2009;27:486–493.
5. Miller RH, Paape MJ, Acton JC. Comparison of milk somatic-cell counts by coulter and fossomatic counters. J Dairy Sci 1986;69:1942–1946.
6. Gonzalo C, Linage B, Carriedo JA, De la Fuente F, San Primitivo F. Evaluation of the overall accuracy of the DeLaval cell counter for somatic cell counts in ovine milk. J Dairy Sci 2006;89:4613–4619.
7. Redelman D, Butler S, Robison J, Garner D. Identification of inflammatory cells in bovine milk by flow cytometry. Cytometry 1988;9:463–468.
8. Moon JS, Koo HC, Joo YS, Jeon SH, Hur DS, Chung CI, Jo HS, Park YH. Application of a new portable microscopic somatic cell counter with disposable plastic chip for milk analysis. J Dairy Sci 2007;90:2253–2259.
9. Dosogne H, Vangroenweghe F, Mehrzad J, Massart-Leen AM, Burvenich C. Differential leukocyte count method for bovine low somatic cell count milk. J Dairy Sci 2003;86:828–834.
10. Dulin AM, Paape MJ, Weinland BT. Cytospin centrifuge in differential differential counts of milk somatic-cells. J Dairy Sci 1982;65:1247–1251.
11. Grenvall C, Augustsson P, Folkenberg JR, Laurell T. Harmonic microchip acoustophoresis: A route to online raw milk sample precondition in protein and lipid content quality control. Anal Chem 2009;81:6195–6200.
12. Petersson F, Nilsson A, Holm C, Jonsson H, Laurell T. Continuous separation of lipid particles from erythrocytes by means of laminar flow and acoustic standing wave forces. Lab Chip 2005;5:20–22.
13. Nilsson A, Petersson F, Jonsson H, Laurell T. Acoustic control of suspended particles in micro fluidic chips. Lab Chip 2004;4:131–135.
14. Barnkob R, Augustsson P, Laurell T, Bruus H. Measuring the local pressure amplitude in microchannel acoustophoresis. Lab Chip 2010;10:563–570.
15. Hawkes JJ, Coakley WT. Force field particle filter, combining ultrasound standing waves and laminar flow. Sens Actuat B Chem 2001;75:213–222.
16. Hultstrom J, Manneberg O, Dopf K, Hertz HM, Brismar H, Wiklund M. Proliferation and viability of adherent cells manipulated by standing-wave ultrasound in a microfluidic chip. Ultrasound Med Biol 2007;33:145–151.
17. Dykes J, Lenshof A, Astrand-Grundstrom IB, Laurell T, Scheding S. Efficient removal of platelets from peripheral blood progenitor cell products using a novel micro-chip based acoustophoretic platform. Plos One 2011;6:e23074.
18. Gawad S, Schild L, Renaud P. Micromachined impedance spectroscopy flow cytometer for cell analysis and particle sizing. Lab Chip 2001;1:76–82.
19. Bao N, Wang J, Lu C. Recent advances in electric analysis of cells in microfluidic systems. Anal Bioanal Chem 2008;391:933–942.
20. Sun T, Morgan H. Single-cell microfluidic impedance cytometry: A review. Microfluidics Nanofluidics 2010;8:423–443.
21. Holmes D, Pettigrew D, Reccius CH, Gwyer JD, van Berkel C, Holloway J, Davies DE, Morgan H. Leukocyte analysis and differentiation using high speed microfluidic single cell impedance cytometry. Lab Chip 2009;9:2881–2889.

Lab on a Chip

PAPER

View Article Online
View Journal | View Issue

Acoustic actuated fluorescence activated sorting of microparticles†

Cite this: *Lab Chip*, 2014, **14**, 1943

Ola Jakobsson,*[a] Carl Grenvall,[a] Maria Nordin,[a] Mikael Evander[a] and Thomas Laurell[ab]

Received 19th December 2013,
Accepted 21st March 2014

DOI: 10.1039/c3lc51408k

www.rsc.org/loc

In this paper, we present a fluorescence activated sorter realized in a continuous flow microfluidic chip. Sorting is achieved by deflecting a focused particle stream with short acoustic bursts (2.5 ms), in a fluorescence activated configuration. The system utilizes two-dimensional acoustic pre-focusing, using a single actuation frequency, to position all particles in the same fluid velocity regime at flow rates up to 1.7 mL min^{-1}. Particles were sorted based on their fluorescence intensities at throughputs up to 150 particles s^{-1}. The highest purity reached was 80% when sorting at an average rate of 50 particles s^{-1}. The average recovery of a sort was 93.2 ± 2.6%. The presented system enables fluorescence activated cell sorting in a continuous flow microfluidic format that allows aseptic integration of downstream microfluidic functionalities, opening for medical and clinical applications.

Introduction

Background

The Fluorescence Activated Cell Sorter (FACS) remains a major workhorse in cell biology laboratories. After more than 40 years of development, the FACS excels at analyzing and sorting cells at very high speeds. Although throughput is an important factor, many applications involving cell sorting also put high demands on viability and require labor-intensive protocols both pre- and post-sorting. Exposure to high shear forces, from the hydrodynamic focusing and the droplet generation process, may affect cell viability.[1] The droplet based sorting mechanism in the conventional FACS complicates closed/aseptic system operation, which is needed when handling clinical or hazardous samples. By retaining sorted cells in a continuous flow throughout the sorting process, some of these limitations can potentially be overcome and additional functionality may be added in sequential downstream microfluidic unit operations.

Historically, a number of different FACS sorting mechanisms have been suggested, many of which are microchip based. Electro-osmotic,[2] dielectrical,[3] optical,[4] and hydrodynamic forces[5] have been used to achieve fluorescence activated cell sorting in a continuous flow. The first FACS device based on the use of standing wave acoustic forces was presented by Johansson *et al.* in 2009,[6] utilizing the difference in fluid densities at a fluid–fluid interface to achieve deflection of particles. While many of these solutions demonstrate state-of-the-art technological solutions, they still suffer from limitations in terms of throughput[7] or require complicated fabrication protocols[8] in order to make them feasible for general cell sorting purposes.

An alternative approach to accomplish chip integrated cell sorting without any moving parts is to employ acoustophoresis, a technique based on standing wave acoustic forces that act directly on cells, in a fluorescence activated configuration. By actuating an acoustically resonant microfluidic structure with ultrasound at its resonance frequency, the resulting standing wave will induce an acoustic radiation force on cells and particles within this structure.[9] With proper design of the microfluidic structure, it is possible to fabricate acoustofluidic components that enables focusing,[10,11] enrichment,[12] separation,[13,14] or gating of cells between multiple outlets[15,16] in continuous flow based microsystems. An additional benefit of acoustophoretic cell handling is that it has been shown to be a gentle method for manipulation and sorting of cells.[17,18] Acoustophoresis is a non-invasive, robust and easy-to-use technique for manipulation of cells in suspensions. The uncomplicated design allows simple fabrication techniques to be used, opening a path towards low cost disposable lab-on-a-chip devices.

[a] *Lund University – Dept. of Biomedical Engineering, Lund, Sweden. E-mail: ola.jakobsson@bme.lth.se*
[b] *Dongguk University – Dept. Biomedical Engineering, Seoul, Republic of Korea*

† Electronic supplementary information (ESI) available. See DOI: 10.1039/c3lc51408k

In commercial FACS instruments, sheath flow is typically used to focus the sample into a very narrow stream prior to the laser interrogation point. The sample to sheath flow ratio typically ranges from 100 : 1 to 1000 : 1, diluting the sample during the analysis process. The sample flow rate for a commercial cytometer is typically limited to ranges between 30 and 120 μL min^{-1}. The hydrodynamic focusing is essential both for the analysis of the cells and the drop delay timing for the sorting process. Two-dimensional hydrodynamic focusing (sometimes also referred to as three-dimensional focusing in the literature), typically reserved for coaxial systems with large flow cells, can also be achieved in planar microchip systems using more elaborate fabrication techniques.[19] Other methods for achieving two-dimensional focusing in planar microchips includes hydrophoresis,[20] inertia,[21] dielectrophoresis[22] and "microfluidic drift focusing".[23,24] In previous work, Goddard *et al.*[25] have shown that acoustic focusing can be used to either eliminate or reduce the needs of hydrodynamic focusing for flow cytometry. While their work was done in coaxial capillary systems, the same principle can be applied to rectangular micro-channels using a single[14] or multiple actuation frequencies[12,26] in a planar format on-chip.

In this work, we present a microchip based FACS that is actuated with ultrasound as the sorting mechanism to achieve a binary sorting of particles based on fluorescence detection. Furthermore, the acoustic FACS described herein employs two-dimensional acoustic focusing, using a single actuation frequency. The acoustic actuated FACS (AFACS) can analyze and sort an event in the span of milliseconds, enabling chip integrated single cell sorting with relatively high throughput and purities.

Theory

Acoustophoresis

Acoustophoresis utilizes ultrasound standing waves to generate a force that acts on particles suspended in a medium. Acoustic actuation of the flow medium gives rise to a number of more or less complex acoustic force phenomena, out of which the primary acoustic radiation force, F_{rad}, dominates and can be used to explain the particle manipulation described in this paper (eqn (1)). By proper chip design, this force can be utilized to position particles in a well-defined position in the flow channel cross-section.

The primary acoustic radiation force translates particles into acoustic pressure nodes or antinodes according to the acoustic contrast factor, Φ, of the particles (eqn (2)). The contrast factor is derived from differences in the density and compressibility of the particles and the surrounding medium. Dense particles (*i.e.* cells) have a positive contrast factor and focus into the nodes when suspended in most commonly used media (water or PBS). In comparison, particles that are less dense than the medium will focus into the acoustic antinodes due to having a negative contrast factor. F_{rad} scales linearly with the contrast factor and the volume, a^3, of the particles.

$$F_{rad} = 4\pi a^3 \Phi k_y E_{ac} \sin(2k_y y) \quad (1)$$

where

$$\Phi = \frac{\kappa_o - \kappa_p}{3\kappa_o} + \frac{\rho_p - \rho_o}{2\rho_p + \rho_o} \quad (2)$$

and a is the particle radius, Φ is the acoustic contrast factor, $k_y = 2\pi/\lambda$ is the wavenumber, E_{ac} is the acoustic energy density, y is the distance from the wall, κ_p is the isothermal compressibility of the particle, κ_o is the isothermal compressibility of the fluid, ρ_p is the density of the particle and ρ_o is the density of the fluid.

Materials and methods

Fabrication of the microchip

The AFACS microfluidic chip was fabricated on a 400 μm thick 3 inch silicon wafer using conventional photolithography and wet etching protocols.[10] Wet etching of <100> silicon in KOH resulted in microfluidic-channels with a rectangular cross-section. Typically, 12 chips could be fitted on one wafer. The chips were diced and anodically bonded to a 1.1 mm thick borosilicate glass lid, and fluidic ports were glued to the chip. Two piezoelectric ceramic plates, 1 mm and 400 μm thick, respectively (Pz26, Ferroperm Piezoceramics AS, Denmark), were attached to the microchip using cyanoacrylate glue. Silicon and glass were chosen as materials in favor of polymeric materials such as PDMS, due to their superior acoustic properties for acoustophoresis applications.

Acoustic actuation

The two piezoelectric transducers were driven separately by two function generators (33120A, Agilent Technologies Inc., Santa Clara, CA, USA). The signal from the function generator that continuously actuated the "pre-focusing zone" with a 4.6 MHz sine wave was amplified with an in-house built circuit, based on a power amplifier (LT1012, Linear Technology Corp., Milpitas, CA, USA).

The function generator actuating the sorting zone with a 2 MHz sine wave was operating in "external triggered burst mode", meaning that upon a trigger signal, the sorting zone was actuated with a programmable number of periods and then was idle until the next trigger signal. The signal was amplified using an amplifier (AR 75A250, Amplifier Research, Souderton, PA, USA). The function generator could not be retriggered unless a burst sequence was complete.

Optical detection and sorting trigger

A Photomultiplier Tube (PMT) (Photomultiplier tube R1617, Hamamatsu, Japan) was mounted in a fluorescence microscope (DM2500 M, Leica Microsystems CMS GmbH, Wetzlar, Germany) monitoring the desired area of the microchip (by adjusting pinhole and aperture settings). The signal from the PMT was coupled to a Schmitt trigger with an adjustable threshold level and hysteresis. When a preset threshold level

was exceeded, a 5 V TTL signal triggered the function generator, actuating the sorting zone. Both the PMT signal and the trigger signal were sampled by a data acquisition card (PCI-6024, National Instruments, Austin, TX, USA) and monitored in a computer environment (LabVIEW), recording the trigger event rate. A block diagram of the system is shown in Fig. 1.

Fluidics

Sample and sheath fluids were continuously infused through their respective inlets using syringe pumps (NeMESYS, Cetoni GMBH, Korbussen, Germany). The outflow ratio between the outlets was controlled by choosing tubing with different hydrodynamic resistance (diameter and length). The flow was split approximately at a 30 : 70 ratio between waste and target outlets. The samples from the target and waste outlets were collected in 15 mL Falcon tubes.

Particle suspensions for sorting experiments

A suspension of 10 μm fluorescent particles (10 μm Melamine Resin FITC, Fluka/Sigma Aldrich, Buchs, Switzerland) and 10 μm non-fluorescent particles (10 μm Melamine Resin Plain, Fluka/Sigma Aldrich, Buchs, Switzerland) suspended in de-ionized water was prepared and diluted to three samples with different concentrations. The concentration was matched to give a throughput of ~50, 100 and 150 particles s^{-1} at a flow rate of 200 μL min^{-1}. The purity of the samples was measured to be 19.5%.

Evaluating sorting purity

The purity of the samples before and after a sort was analyzed with a commercial flow cytometer (FACS Canto II with FACS Diva software, BD Biosciences, San Jose, CA, USA). The purity of a sample was defined as:

$$\text{Purity} = \frac{\text{number of fluorescent particles}}{\text{total number of particles}}$$

Aggregated beads (doublets and triplets) were excluded from the analysis to exclude non-system inherent bias. This gating did not affect the results significantly.

The recovery of target particles in the target outlet was estimated by analyzing the amount of target particles in the collected waste tube. The recovery was estimated by:

$$\text{Recovery\%} = 100 - \frac{\text{purity waste outlet\%}}{\text{starting purity\%}}$$

Confocal microscopy

Confocal microscopy was used to image the spatial distribution of microparticles in the micro-channel cross-section at the end of the pre-focusing zone of the microchip. FITC labeled fluorescent particles (10 μm FITC Polystyrene, Fluka/Sigma Aldrich, Buchs, Switzerland), suspended in de-ionized water, were used to obtain confocal images with an Olympus microscope (BX51WI, Olympus Corporation, Tokyo, Japan) and software (Fluoview 300) was subsequently used to reconstruct cross-sectional images.

Measuring particle velocity and retention time within the sorting zone

Particle velocity was measured by comparing particle positions between two subsequent frames. Images were recorded by using a microscope (DM2500 M, Leica Microsystems CMS GmbH, Wetzlar, Germany) mounted high frame rate CCD camera (EoSens mini MC-1370, Mikrotron GmbH, Unterschleissheim, Germany) and particle positions were determined using image analysis software (ImageJ). The length of the sorting zone was estimated to be 1.7 mm. The retention time of a particle in the sorting zone was calculated by dividing this length with the average measured velocity for a given flow rate.

AFACS operating principle

Based on the acoustophoresis principle, we have developed an acoustically actuated FACS where short ultrasound bursts drive the sorting mechanism. The principle of the AFACS is illustrated in Fig. 2. Particles are continuously injected into the chip through the sample inlet. A sheath fluid is injected through the sheath flow inlet, laminating the particle sample stream along the side wall. All particles are then two-

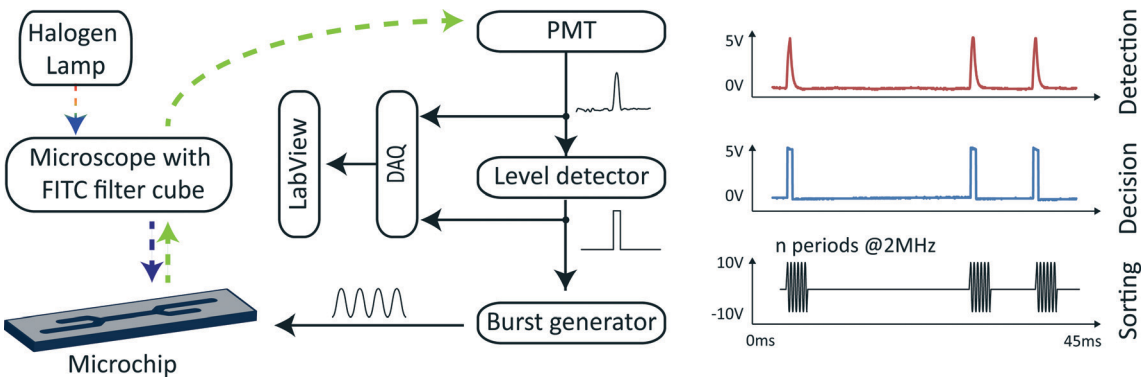

Fig. 1 A block diagram of the optical system and sort trigger electronics. The signal from the PMT (red, top right) and the level detector (blue, middle right) are actual recordings. The signal from the burst generator (black, bottom right) is illustrated. Typically, a burst contained between 5000 and 12 000 periods at 2 MHz.

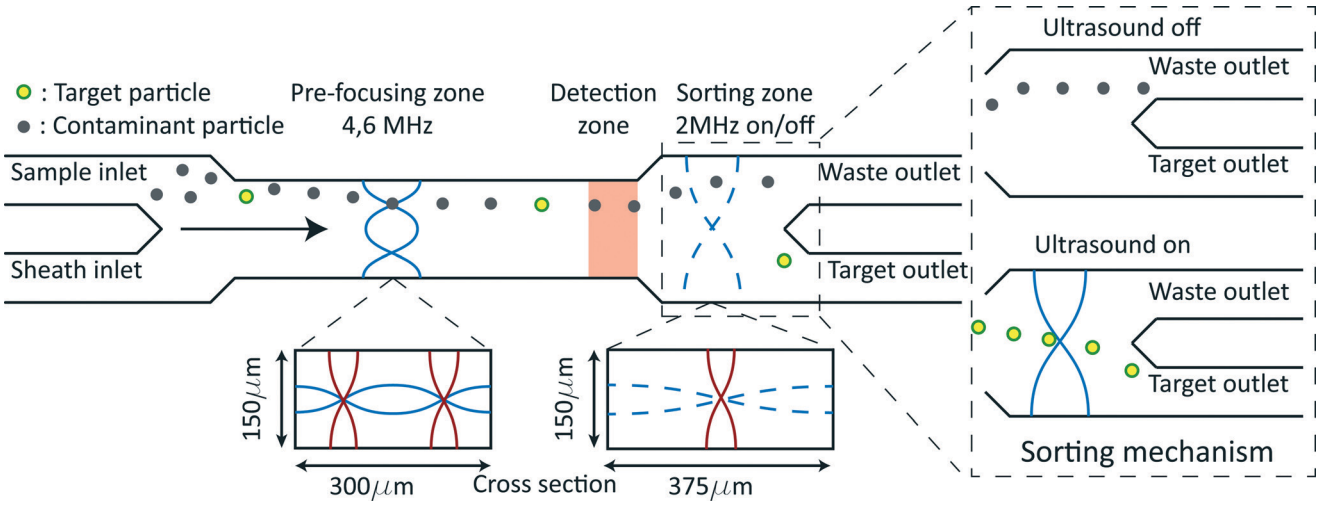

Fig. 2 Schematic of the operating principle of the AFACS.

dimensionally aligned in the "pre-focusing zone" by the acoustic radiation force. A piezoelectric transducer is continuously actuating the microfluidic channel at 4.6 MHz (one wavelength resonator), resulting in a standing wave with two horizontal pressure nodes, symmetrically placed on both sides of the channel centre, approximately 90 μm away from the walls, respectively. The particles will, however, only reach and be forced into the horizontal pressure node closest to the sample side wall because of the sheath flow confinement to one side of the micro-channel. Due to the 2 : 1 aspect ratio of the channel, a vertical pressure node (1/2 wavelength resonator) will also form, which will force particles to the vertical center of the structure, hence providing two-dimensional focusing (simultaneous vertical and horizontal focusing) of the particles in the pre-focusing zone. This "pre-focusing step" improves the optical detection, sorting accuracy and throughput of the AFACS by aligning all particles in the same flow velocity vector.

After being precisely aligned in the "pre-focusing zone", the particles pass a "detection zone" before they reach the "sorting zone". The detection zone is monitored by a fluorescence filtered PMT which, upon detecting a fluorescent particle, sends a signal to an electronic system that triggers a sorting event. When a sorting decision is made, the sorting zone of the chip is actuated with a 2 MHz (1/2 wavelength resonator) ultrasonic burst, deflecting particles towards the horizontal center of the sorting zone, approximately 90 μm, which is sufficient to allow translation of these particles into the target outlet. The flow ratio between the waste and target outlets is approximately 30 : 70. The ultrasonic burst length is matched to the retention time of a particle in the sorting zone of the chip, thus achieving optimal system performance (see S1 of the ESI†).

An image of the AFACS-microchip used for the experiments is presented in Fig. 3, showing the sample and sheet flow inlet (upper left inset) and the waste and target outlets (lower right inset). The two piezoelectric actuators are seen

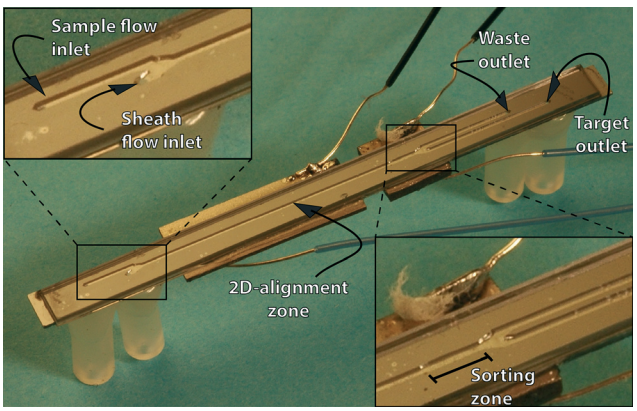

Fig. 3 A photograph of the AFACS-microchip. The insets show close-up images of the inlet and outlet of the chip.

glued to the back side of the chip where the long rectangular transducer operates the 2-dimensional pre-focusing zone and the smaller square transducer drives the sorting zone. The total length of the chip is 45 mm.

Results and discussion

Characterization of the two-dimensional pre-focusing

The two-dimensional pre-focusing is essential for the AFACS in 3 ways:

1. Positioning all particles into the same flow vector, resulting in uniform velocities and retention times within the system.

2. Positioning the particles where the acoustic radiation force is at its maximum when performing the acoustophoretic particle switching, thus minimizing the acoustic actuation time for deflection of pre-aligned particles.

3. Positioning the particles in the focal plane of the detector, improving detection performance.

The two-dimensional focusing was experimentally verified using confocal microscopy, as shown in Fig. 4. At flow rates

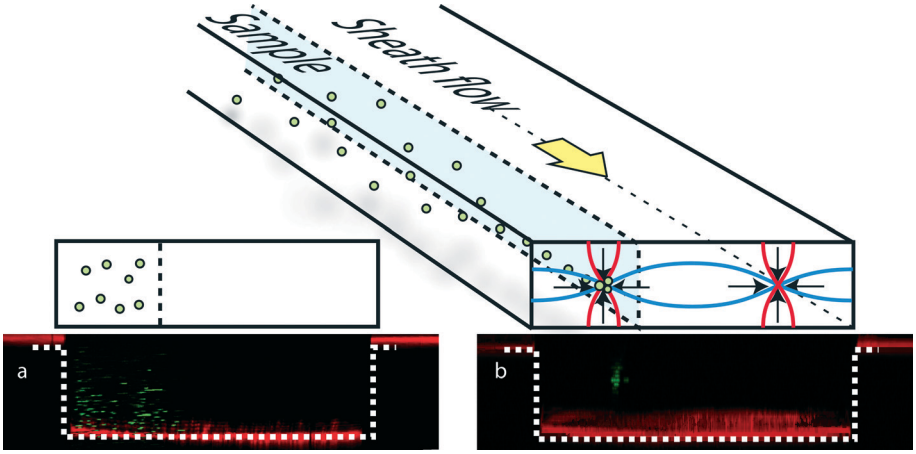

Fig. 4 a. A confocal image projection of the cross-section of the pre-focusing zone, showing unfocused FITC marked polystyrene beads at 300 μL min^{-1}. The red color (and the dashed line) indicates the chip boundary. b. A confocal image projection of the cross-section of the acoustic FACS micro-channel, showing two-dimensional acoustic pre-focusing of FITC marked polystyrene beads at a flow rate of 300 μL min^{-1}.

above 2 mL min^{-1}, the retention time in the pre-focusing zone was not sufficient at the given acoustic force to focus particles two-dimensionally into a well defined and confined stream line.

To illustrate the effect of the two acoustic actuation modes, Fig. 5a–d show an image sequence of the particle trajectories in the sorting zone. In Fig. 5b, the pre-focusing is inactive, in Fig. 5c pre-focusing has been activated and in Fig. 5d, both pre-focusing and sorting actuation have been activated in continuous mode. It can be noted that the retention time of the particles in the sorting zone is well within the time window to be translated into the channel centre before exiting the chip.

The retention time for a particle in the sorting zone is critical as this parameter sets the limit of the system throughput and the highest possible flow rate is desired in this respect. For optimal system performance, the input power and duration of the acoustic sorting burst signal should be matched to the retention time, see S1 of the ESI.† For this reason, the velocity of the particles in the two-dimensional focusing position was measured in the "sorting zone" for a varying set of flow rates. The measured velocity increased linearly with the flow rate and the relative standard deviation of the particle velocity distribution was less than 10% at a flow rate of 2 mL min^{-1}, see S2 of the ESI.†

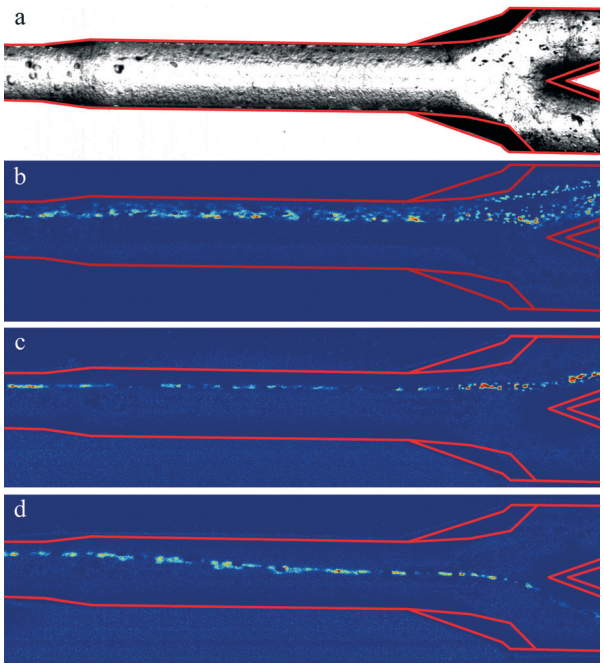

Fig. 5 a. A bright field image showing the sorting zone of the microfluidic chip. The walls of the chip are outlined in red. The direction of flow is from left to right. The lower outlet is the target outlet. b. Image of the sorting zone where particles are visualized using background subtraction. No actuation of the 2-D pre-focusing is employed, showing particles distributed across the entire sheet flow region along the topmost side wall. c. Pre-focusing zone is actuated, showing particles focused into a confined stream approximately 90 μm out from the topmost side wall. The sorting transducer is not activated. Particles are recovered in the waste outlet (top outlet). d. Pre-focusing and sorting zones are actuated simultaneously. Particles are recovered in the target outlet (lower outlet).

Characterization of switching time

To find the minimum acoustic burst time necessary for deflecting a particle sufficiently to be translated into the target outlet, a highly concentrated particle suspension with 10 μm polystyrene beads was injected into the chip. The 2 MHz transducer was actuated periodically with a 10% duty cycle, and the burst length was reduced until particles were no longer translated into the target outlet. The sorting zone and the two outlets of the chip were monitored by a high-speed camera, capturing images at approximately 6000 frames per second. The minimum acoustic burst time required to deflect particles sufficiently for capture in the target outlet was found to be 500 μs (1000 periods at 2 MHz). Fig. 6 shows a time-lapse sequence of an acoustic burst lasting 1 ms.

A video demonstrating 100 Hz periodic gating with a 10% gating duty cycle (1 ms) is available in S4 of the ESI.†

Sorting performance

The samples were injected into the chip at 200 μl min^{-1}. The acoustic burst time was set to 2.5, 4, or 8 ms. The number and times of triggering events were continuously sampled. As the system lacked the equivalent to a forward scatter signal, the total throughput in particles s^{-1} had to be estimated:

$$\text{throughput} = \frac{\text{triggering events s}^{-1}}{\text{starting purity}}$$

As the detector could not distinguish between positive events close to each other, the throughput was most likely underestimated. At least 10 000 particles were sorted per experiment. Experimental parameters are given in Table 1.

The sample flow rate was deliberately kept constant at 200 μL min^{-1} to reduce experimental variations due to sedimentation effects in syringes and sample inlet tubing. The obtained purity as a function of the acoustic actuation time of the sorting zone and throughput is seen in Fig. 7. The average recovery of target particles for all experiments was 93.2 ± 2.6%. The device did not show any sign of clogging during any experiment.

The relation between purity and throughput

The primary factor affecting the sort purity is the relation μ between the "acoustic actuation time" and the average time between events (throughput) in the channel

$$\mu = \frac{\text{Acoustic actuation time}}{\text{average time between events}}$$

The expected purity for an experiment is calculated by using a probability theory, assuming the system works ideally and a Poisson distributed event rate (see S3 of the ESI†):

$$\text{Minimum expected purity} = \frac{1}{1+\mu}$$

As the acoustic burst time is decreased, the probability of capturing more than one particle is reduced, thus increasing the purity. Reducing the particle concentration but maintaining the total flow rate will result in more space between the particles and does also decrease the probability of capturing false positives. Fig. 8 shows experimental data for the relation between purity and μ, together with a calculated (expected purity) line. Most data points fall below the theoretical value. This might be caused by trigger timing errors, an underestimated μ value (throughput or acoustic burst time), or a non-Poisson distributed sample (*e.g.* sample aggregation or sample flow variations). In theory, it should be hard to obtain sort purities above this theoretical line. To the best of our knowledge, this limitation applies to all

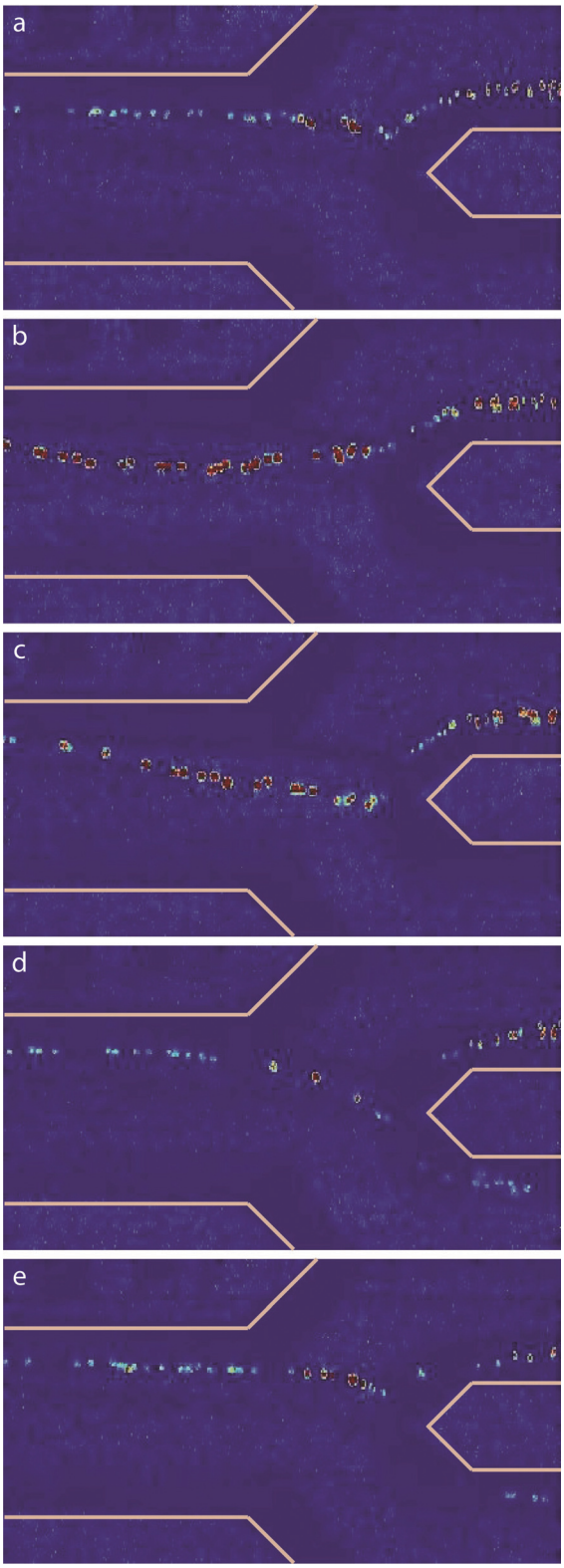

Fig. 6 a. t = 0 ms: the ultrasound is turned on. b. t = 1 ms: the ultrasound is turned off. Particles are deflected towards the center of the sorting zone, upstream of the flow splitter. c. t = 1.6 ms: the deflected particle stream is breaking off from the non-actuated particle segment, approaching the flow splitter towards the sorting outlet. d. t = 2.5 ms: deflected particles exit through the target outlet. e. t = 3.3 ms: particles are again exiting through the waste outlet. The last few particles that were deflected are still seen exiting the sorting outlet.

Table 1 Experimental parameters for each experiment

Acoustic actuation time (ms)/burst	4.6 MHz sine V_{pp} (continuous)	2.0 MHz sine V_{pp} (burst)	Sample flow rate (μL min^{-1})	Sheath flow rate (μL min^{-1})	Average particles s^{-1}
6	3	30	200	600	50, 100, 150
4	3	30	200	1100	50, 100, 150
2.5	4	40	200	1500	50, 100, 150

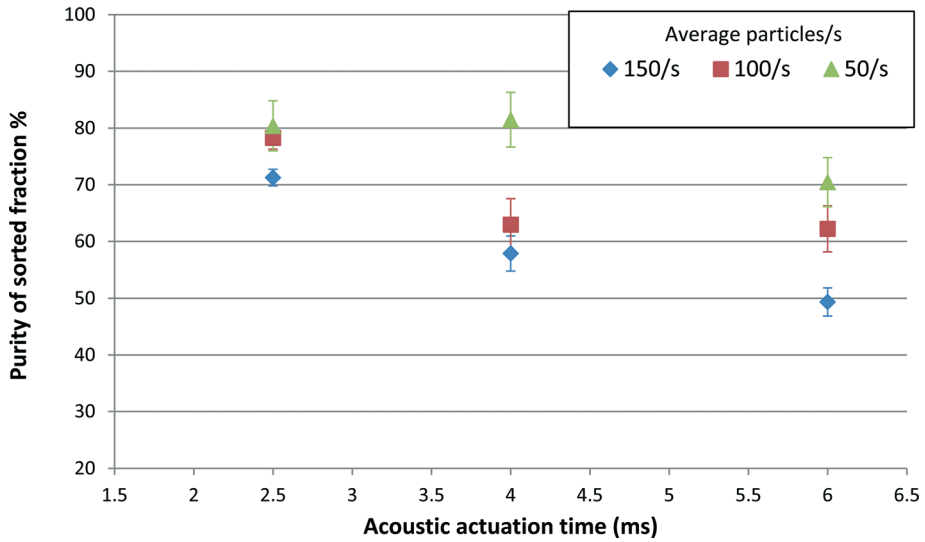

Fig. 7 Sorting performance for 34 experiments with different throughput and acoustic actuation time. The purity of the sample injected into the chip was 19.5%. Each data point is an average of either three or four experiments. The standard deviation is shown by the error bars.

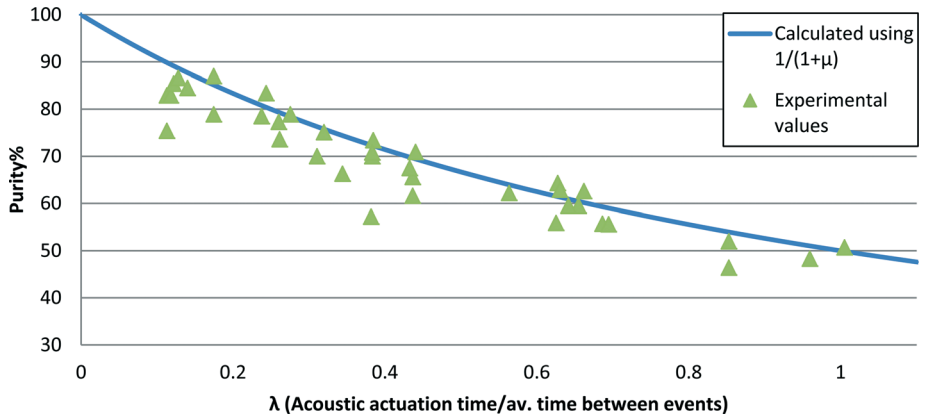

Fig. 8 Purity *vs.* μ for 36 experiments. The blue line shows the calculated expected minimum purity.

continuous flow based sorters that lack the equivalent to a "coincidence abort"[7] function.

Future improvements and outlook

Integration of a forward scatter signal detector (FSC) would allow the AFACS system to detect non-fluorescent particles in the sorting zone, giving it the ability to sort with a much higher purity by implementing the equivalent to a "sort mask" (coincidence abort function) when making a sorting decision.

Shortening of the "sorting zone" would allow a shorter acoustic actuation time, increasing performance of the system. Experiments showed that an acoustic actuation time of 500 μs was sufficient to deflect particles for recovery in the target outlet. However, due to the required 1:1 relation between particle retention time in the sorting zone and acoustic actuation time, using such a short acoustic burst would require a total flow rate of approximately 8 mL min^{-1}. The current limitation of the "pre-focusing zone" was, however, about 2 mL min^{-1} for the microchip used, but this could be alleviated by a longer "pre-focusing zone".

Since the acoustic force on a particle scales with volume, sorting of smaller particles would be less efficient in the present system. However, this can be addressed by suspending the

sample in a fluid with a higher density compared to the sheath fluid, allowing the ultrasound to act on the entire sample stream rather than the individual particles, similar to the method demonstrated by Johansson *et al.*[6]

By realizing a sorter in continuous flow, as opposed to two-phase flow[27,28] or aerosol-based techniques (drop in air), the option of integrating additional functionality (such as a second sorter) downstream of or parallel to the sorter becomes available. The acoustic two-dimensional focusing gives a large flexibility in terms of sample to sheath flow ratio, and a recent study has shown that acoustic focusing can be utilized to achieve sheath-less parallel flow cytometry.[11] As the smallest dimension at any point in the device is 150 μm and the deflection distance for a sort event is ~90 μm, the device may also be suitable for sorting of larger entities such as clusters of cells or ovum cells. The dimensions of the chip in combination with the high flow rates used in the experiments made the system very resistant to clogging, and no sample pretreatment (filtering) was needed.

When comparing the performance of the AFACS to other FACS systems, both the purity and the throughput must be taken into consideration. *E.g.* very high throughputs can be obtained by doing very low purity sorts.[29] The performance of a FACS system should not be measured as an enrichment number, as this parameter is sample-dependent. We have shown that the limiting factor for our system, and to the best of the authors' knowledge, for all continuous flow based FACS systems, is how long the sample stream is deflected during a sort event (denoted as t_sort in S3 of the ESI†). It is also shown that this variable links throughput and purity together, and we propose that the performance of a FACS system should be measured using this variable.

Conclusion

We have shown that acoustic standing wave forces can be used to achieve lab-on-a-chip integrated FACS sorting in a continuous flow. Although slower than most commercially available FACS systems, the benefits of a closed sample line and a continuous flow system with a possibility of integration with additional downstream microfluidic unit operations may outweigh the drawbacks of a reduced throughput.

References

1 J. F. Leary, in *Current Protocols in Cytometry*, John Wiley & Sons, Inc., 2001.
2 A. Y. Fu, C. Spence, A. Scherer, F. H. Arnold and S. R. Quake, *Nat. Biotechnol.*, 1999, **17**, 1109–1111.
3 S. Fiedler, S. G. Shirley, T. Schnelle and G. Fuhr, *Anal. Chem.*, 1998, **70**, 1909–1915.
4 M. M. Wang, E. Tu, D. E. Raymond, J. M. Yang, H. Zhang, N. Hagen, B. Dees, E. M. Mercer, A. H. Forster, I. Kariv, P. J. Marchand and W. F. Butler, *Nat. Biotechnol.*, 2005, **23**, 83–87.
5 S. H. Cho, C. H. Chen, F. S. Tsai, J. M. Godin and Y.-H. Lo, *Lab Chip*, 2010, **10**, 1567–1573.
6 L. Johansson, F. Nikolajeff, S. Johansson and S. Thorslund, *Anal. Chem.*, 2009, **81**, 5188–5196.
7 H. M. Shapiro, *Practical flow cytometry*, Wiley-Liss, Inc., 605 Third Avenue, New York, New York 10158-0012, USA; Chichester, England, 3rd edn, 1995.
8 *Flow Cytometry for Biotechnology*, ed. L. A. Sklar, Oxford University Press, 198 Madison Avenue, New York, NY 10016, USA, 2005.
9 L. P. Gorkov, *Sov. Phys. Dokl.*, 1962, **6**(9), 773–775.
10 A. Nilsson, F. Petersson, H. Jonsson and T. Laurell, *Lab Chip*, 2004, **4**, 131–135.
11 M. E. Piyasena, P. P. A. Suthanthiraraj, R. W. Applegate, A. M. Goumas, T. A. Woods, G. P. Lopez and S. W. Graves, *Anal. Chem.*, 2012, **84**, 1831–1839.
12 M. Nordin and T. Laurell, *Lab Chip*, 2012, **12**, 4610–4616.
13 F. Petersson, L. Aberg, A. M. Sward-Nilsson and T. Laurell, *Anal. Chem.*, 2007, **79**, 5117–5123.
14 P. Augustsson, C. Magnusson, M. Nordin, H. Lilja and T. Laurell, *Anal. Chem.*, 2012, **84**, 7954–7962.
15 T. Franke, S. Braunmuller, L. Schmid, A. Wixforth and D. A. Weitz, *Lab Chip*, 2010, **10**, 789–794.
16 X. Ding, S.-C. S. Lin, M. I. Lapsley, S. Li, X. Guo, C. Y. Chan, I. K. Chiang, L. Wang, J. P. McCoy and T. J. Huang, *Lab Chip*, 2012, **12**, 4228–4231.
17 M. A. Burguillos, C. Magnusson, M. Nordin, A. Lenshof, P. Augustsson, M. J. Hansson, E. Elmer, H. Lilja, P. Brundin, T. Laurell and T. Deierborg, *PLoS One*, 2013, 8.
18 J. Dykes, A. Lenshof, I. B. Astrand-Grundstrom, T. Laurell and S. Scheding, *PLoS One*, 2012, **7**, e30074.
19 C. Simonnet and A. Groisman, *Anal. Chem.*, 2006, **78**, 5653–5663.
20 S. Choi, S. Song, C. Choi and J.-K. Park, *Small*, 2008, **4**, 634–641.
21 A. J. Chung, D. R. Gossett and D. Di Carlo, *Small*, 2013, **9**, 685–690.
22 D. Holmes, H. Morgan and N. G. Green, *Biosens. Bioelectron.*, 2006, **21**, 1621–1630.
23 X. Mao, A. A. Nawaz, S.-C. S. Lin, M. I. Lapsley, Y. Zhao, J. P. McCoy, W. S. El-Deiry and T. J. Huang, *Biomicrofluidics*, 2012, 6.
24 M. Piagnerelli, K. Z. Boudjeltia, D. Brohee, A. Vereerstraeten, P. Piro, J. L. Vincent and M. Vanhaeverbeek, *J. Clin. Pathol.*, 2007, **60**, 549–554.
25 G. Goddard, J. C. Martin, S. W. Graves and G. Kaduchak, *Cytometry, Part A*, 2006, **69**, 66–74.
26 O. Manneberg, J. Svennebring, H. M. Hertz and M. Wiklund, *J. Micromech. Microeng.*, 2008, 18.
27 J.-C. Baret, O. J. Miller, V. Taly, M. Ryckelynck, A. El-Harrak, L. Frenz, C. Rick, M. L. Samuels, J. B. Hutchison, J. J. Agresti, D. R. Link, D. A. Weitz and A. D. Griffiths, *Lab Chip*, 2009, **9**, 1850–1858.
28 C. Lee, J. Lee, H. H. Kim, S.-Y. Teh, A. Lee, I.-Y. Chung, J. Y. Park and K. K. Shung, *Lab Chip*, 2012, **12**, 2736–2742.
29 A. Wolff, I. R. Perch-Nielsen, U. D. Larsen, P. Friis, G. Goranovic, C. R. Poulsen, J. P. Kutter and P. Telleman, *Lab Chip*, 2003, **3**, 22–27.

Lab on a Chip

PAPER

View Article Online
View Journal

Cite this: DOI: 10.1039/c4lc00982g

Two-dimensional acoustic particle focusing enables sheathless chip Coulter counter with planar electrode configuration

Carl Grenvall,*[a] Christian Antfolk,[a] Christer Zoffmann Bisgaard[b] and Thomas Laurell*[ac]

Received 22nd August 2014,
Accepted 29th September 2014

DOI: 10.1039/c4lc00982g

www.rsc.org/loc

The field of cytometry has grown in scope and importance ever since the early 20th century with leaps in technology introducing the Coulter counter and the flow cytometer. Cytometry methods have brought about a revolution for the medical and biotechnology industry by providing fast and accurate analysis of cell and particle suspensions. Recent developments in the field aim at improving current cytometers and to provide miniaturized low-cost cytometry systems for point-of-care clinical diagnostics or research. In an attempt to address the need for particle positioning which is important for both impedance and optically based cytometers we present a microfluidic system which precisely positions cells and particles, using acoustic forces and subsequently performs measurements using an integrated and simple planar electrode Coulter-type impedance cytometer without the need for sheath flows. Data is presented to show how the acoustic method improves the accuracy of the impedance cytometer when prefocusing is employed to particles and cells (diluted whole blood). Confocal imaging and simulations support the findings and provide the basis for further improvements. The acoustophoretic prefocusing technique opens a path towards small, low cost cytometers while also providing an easy way to improve current systems.

Introduction

In this paper acoustic forces are utilized to address the need for precise positioning of cells and particles in continuous flow to enable low cost chip integrated Coulter counters. When using Coulter type instruments the particle position in relation to the electrical field gradient in the measurement cell is important, and correspondingly, when using light or fluorescent techniques the particle need to be positioned in the focal plane of the light sources and detectors. High throughput cytometry first became available with the introduction of the Coulter principle.[1,2] Coulter cytometers count and size particles by measuring the variations in impedance or resistance that the particles cause when displacing a conductive fluid in an electric field. Typically, the electric field is generated across a narrow aperture to maximize the proportional fluid volume displacement. Early research improved the aperture, the flow control and the instruments that quantify the electric pulses caused by the particles.[3–5] The instruments have since been improved by computerization, but not vastly changed until recently, when microfabrication technologies introduced new possibilities in terms of aperture design and electrode configuration in planar microchip formats.[6]

Notes about how to position particles by the use of nozzles, flow chambers or sheath flow strategies were already included in early cytometer papers and patents. In particular, the ability to position particles using sheath flows is of importance in most cytometers regardless of the detection method, including impedance measurements as well as traditional microscopy or fluorescence flow cytometry, since this not only allows positioning but also prevents clogging, a frequent problem when using small apertures and nozzles.[7–9] The introduction of chip integrated microfluidic systems made it possible to design new kinds of coulter type instruments, where electrodes could be placed in parallel along or across a microfluidic channel. This type of non-axial electrode configuration was actually included in Coulters original patent but deemed difficult to implement due to thermal noise.[10] The transition to microfluidic systems also facilitated the development of continuous flow based microchip impedance spectroscopy (MIS), a method that allows cell counting and sizing combined with the ability to differentiate between cell types, by measuring impedance across cell membranes and cytosols in high frequency electric fields.[11,12] Current improvements in the impedance cytometry field can be attributed to improved control of fabrication steps on the micro scale. These include clever electrode configurations,

[a] Department of Biomedical Engineering, Lund University, Sweden. E-mail: carl.grenvall@bme.lth.se
[b] Foss Analytical A/S, FOSS, Hillerød, Denmark
[c] Department of Biomedical Engineering, Dongguk University, Seoul, Republic of Korea

aperture designs and particle positioning methods. Several novel electrode designs have recently been proposed. These include transverse, planar and liquid electrode systems.[13–15] Compared to transverse designs, which depend on precisely fitting top and bottom channel substrates to align the electrodes precisely to each other, the planar configurations are cheaper and easier to fabricate but suffer from sensitivity in the particle positioning during the measurement since the electrical field is non homogenous.[16–18] Hydrodynamic lamination of a non-conductive sheath flow around a conductive sample medium in one- or two-phase systems, to create a fluidic aperture rather than a microfabricated aperture, has also been presented. The technique, while promising in the sense that it is able to produce very narrow adjustable apertures, is sensitive to ion diffusion which causes erroneous measurements, and unstable flow, which requires a more complex fluidic solution.[19–21]

Microfluidic chip cytometry has created new possibilities for the cytometry research field, but also added new challenges since the materials and fabrication process of these chips do not easily yield the kind of macro scale hydrodynamic positioning methods, axisymmetric nozzles and fluid handling techniques, used in larger systems to improve throughput and avoid clogging.[22–26] Thus new ways of positioning the particles to comply with the planar configurations of chip based microfluidics were presented. These include systems utilizing externally induced electrokinetic, magnetic or optical forces as well as hydrodynamic forces and other ways to manipulate particles by accurate design of the flow channels themselves.[27–36] While able to position particles satisfactorily, these new techniques also have their weaknesses. In order to achieve precise positioning using multiple channel hydrodynamic focusing, the microfluidics systems often get more complex and expensive to produce, requiring an increased number of fabrication steps and several fluid pumps which makes them bulkier and harder to integrate into analytic instruments. High flow rate as in the case of sheet flow configurations may cause stress on cells and thus impact viability. While electric focusing techniques can be used in uncomplicated fluidic systems, they also make the systems more complex due to electrode interference between focusing and sensing electrodes which needs to be addressed with more or less intricate designs.[37,38]

Acoustophoresis, a method in which particle positions are manipulated using standing wave acoustic forces, is gentle to cells with reports of successful sample particle focusing, separation, sorting, fractionation, trapping, media switching and in-field cell culturing.[39–43] Acoustic forces on microparticles were first investigated in the late 19th century with improved understanding reported in the mid-20th century.[44–47] Recent reports on how acoustic forces act on microparticles in a microfluidic channel provide the basis on which the system reported herein was designed.[48] Typical acoustophoretic systems are designed to actuate the primary eigenmodes of the microfluidic channel such that an acoustic half wavelength standing wave is established and the corresponding pressure node is formed in the horizontal or vertical center plane of the channel either because of wall–wall (horizontal focusing) or top-bottom (vertical focusing) resonance. Designs with multiple nodes have also been presented, often in systems with complex biosuspensions in order to control the different types of cells and particles, or to add parallel functionality and increase throughput.[49,50] Recently several designs that actuate the channel in both planes simultaneously (2D-focusing) have been presented. This can be done either by using two acoustic actuation frequencies, one for each direction, or by designing the channel in such a way that a single frequency can be used to form standing waves in both directions.[51–54] Fundamental developments of sheathless 2D-focusing of particles in flow was described by Goddard *et al.*[55] who shortly after realized this in an excellent and unsurpassed work on fluorescence flow cytometry.[56] This development fuelled the commercial development of the Attune acoustic focusing flow cytometer (Life Technologies). The possibility of precise non-contact spatial localization of particles in flow using bulk acoustic standing waves suggests that acoustic 2D-focusing of particles also could be realized in sheathless chip integrated impedance cytometry.

In this paper we address some of the challenges of chip complexity in MIS systems, required to accomplish sufficient measurement accuracy, by combining a low cost planar electrode design with precise acoustophoretic particle positioning. Rather than striving to create a homogenous electrical field across the impedance measurement zone, we propose the use of a planar electrode configuration with a gradient electrical field and instead ensure that the particles/cells are acoustically aligned to the same location in the electrical field gradient, such that equally accurate impedance measurements can be accomplished as compared to measurements based on standard Coulter instrumentation.

A chip with a single glass channel was designed and fabricated to allow upstream acoustic 2-dimensional prefocusing of cells and particles, aligning these in a uniform position in the channel cross section prior to entering a downstream measurement aperture with two pairs of planar electrodes that allowed single particle differential impedance measurements to be carried out. We present theoretical and experimental data on polystyrene particles and cells (diluted whole blood) that support our claim that the system is able to count and size cells and particles using a standard glass microfabricated Coulter counter orifice with a planar electrode configuration. The acoustic Coulter counter chip is benchmarked against golden standard Coulter counter measurements showing equal or better performance. The work presented here is a continuation of our project in which we aim to develop a chip based low cost acoustophoretic cytometer for milk quality control.[57]

Materials and methods

Chip design and system setup

The microfluidic chip was designed to support a two dimensional (2D) acoustic focusing pressure node in the center of a

straight channel (width: 420 μm height: 150 μm) and was fabricated in glass by Micronit Microfluidics, the Netherlands. 2D prefocusing was accomplished by simultaneously exciting both the fundamental vertical as well as the horizontal resonance mode of the channel cross section using two piezoceramic transducers (PZ26, Ferroperm) actuated at 2 and 5.3 MHz respectively by a dual channel function generator (AFG 3022B, Tektronix). The system was configured with two transducers, enabling actuation of each resonance mode separately when investigating system performance with no ultrasound, only vertical (1DV), only horizontal (1DH) and 2D-prefocusing (Fig. 2a). The 5.3 MHz signal was amplified to a peak-to-peak amplitude of 12 V using an in-house designed RF amplifier while the corresponding 2 MHz signal was operated at 7 V_{pp} using only the signal generator. The transducers were glued to an aluminium block (10 × 10 × 20 mm), acting as a heat sink and, and was docked to the glass chip. Glycerol was applied as an acoustic coupling layer between the aluminium block and the glass chip.

The chip was placed in a holder (Fluidic Connect 4515, Micronit Microfluidics), providing fluidic and electronic access to the chip, using threaded PEEK connectors. The fluidic network, Teflon tubing with 0.3 mm inner diameter (TFE 58697-U, Supelco), connected the 1 ml sample syringe (BD Plastipak, Becton Dickinson) to the channel inlet and the channel outlet to an open waste container. Constant sample flow was generated using a syringe pump (Nemesys, Cetoni).

The mid-section of the microfluidic channel was narrowed to an aperture (width: 80 μm height: 35 μm) where planar electrodes was patterned across the flat bottom for the impedance measurements. A forked signal electrode was placed between three pairs of sensing electrodes, allowing for optional spatial electrode distances. In this paper the electrode pair closest to the signal electrode was used. Each electrode was 200 nm thick and 20 μm wide and placed with a center–center distance of 50 μm (30 μm of non-patterned glass between each electrode). The signal electrode fork was 80 μm wide center–center. The fluidic network was connected to ground and all cables were shielded in order to minimize external noise (predominantly 50 Hz). Signal generation and MIS signal detection was carried out using an impedance spectroscope (HF2IS, Zürich Instruments) operated in differential mode. Current signals from the sensing electrodes were amplified and converted to voltage using a trans-impedance current amplifier (HF2TA, Zürich Instruments) prior to data acquisition. Pulse data was recorded on a PC using pulse edge triggered software (LabOne, Zürich Instruments) in order to minimize raw data stream sizes and allow long term measurements (230 kSa s^{-1}, 40 μs TC). The data was exported to MATLAB (MATLAB, Mathworks) for further analysis. An overview of the experimental setup can be seen in Fig. 1.

The primary acoustic radiation force focuses particles into either acoustic pressure nodes or antinodes according to their acoustic contrast factor. The contrast factor depends on differences in the density and compressibility of the particles

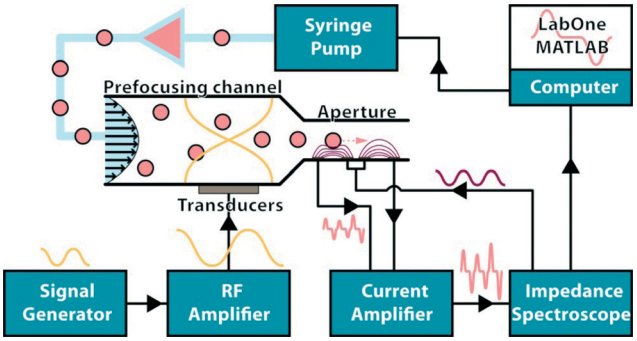

Fig. 1 Schematic of the experimental setup. A computer controlled syringe pump maintained a stable flow in the channel. The sample suspension was pumped into the chip where the particles/cells were acoustophoretically prefocused in a single flow velocity vector using a 2-dimensional acoustic standing wave field prior to entering the MIS aperture. MIS signal generation and readout was performed by an impedance spectroscope, followed by MathLab analysis.

and the surrounding medium.[58] Dense particles (*i.e.* cells) have positive contrast, and consequently focus into the nodes, when suspended in most commonly used flow media like water.

When isotropically etched glass is used as channel material the resulting channel walls will be rounded. This results in an acoustic field that is more complex as compared to straight wall geometries *cf.*[53] Although, the acoustic focusing performance of isotropically etched glass channel geometries operated in 1 dimension horizontal resonance mode have previously been investigated, a COMSOL (Multiphysics 4.3a, COMSOL) simulation of both the fundamental vertical and horizontal resonance mode was performed in this study (Fig. 3), and compared to the corresponding experimentally derived confocal data (Fig. 5).[59]

Impedance based flow cytometry

A planar electrode configuration allows all electrodes to be placed on a single substrate bonded directly to another substrate in which the flow channel is fabricated. This makes the manufacturing process less complicated (cheaper) but in turn strictly requires that all particles are passing through the same spatial position in the aperture cross section, commonly accomplished by a more complex fluidic set-up using a 2-dimensional sheet flow. In terms of accuracy, planar configurations are equal to transverse systems, but only when the particle positioning can be controlled, since the planar systems are more prone to erroneous readings due to varying particle positions (Fig. 2b). By applying an AC-field across a suspension, the passing particles will induce resistance changes in the suspension as they flow past the electrode pairs, giving rise to pulses from which particle sizes can be derived (Fig. 2c).[10] The MIS was operated at an amplitude of ~2 V and a frequency of ~1 MHz, at which it can be described as a Coulter counter, where the changes in suspension resistance is dominated by conductive fluid volume changes (particle size) rather than membrane capacitance or cytosol resistance contributions (Fig. 2d). The data generated by the MIS was analyzed using Matlab (Matlab 2012b, Mathworks).

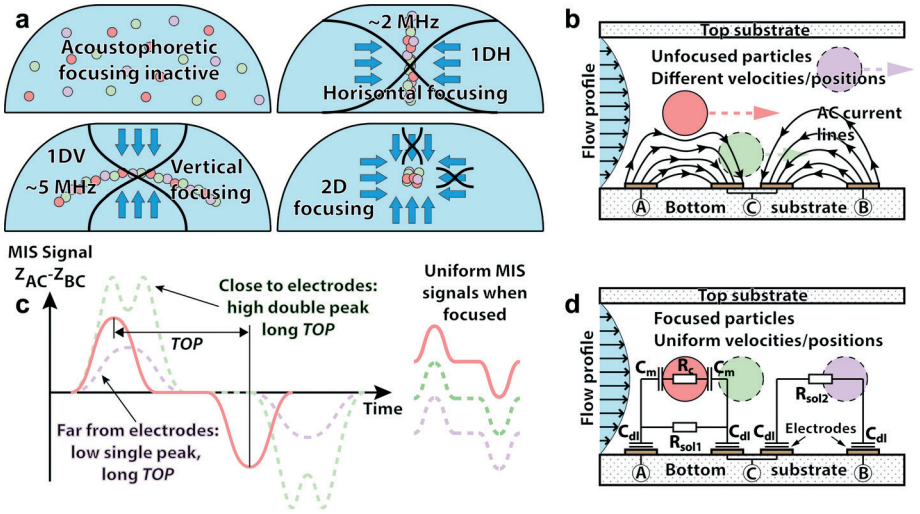

Fig. 2 Schematics of 2D acoustophoretic prealignment in MIS. Vertical and horizontal focusing is combined to create a 2D focusing node in an acoustophoretic system based on isotropically etched glass channels (a). MIS readout in planar electrode configurations is sensitive to particle positioning due to the heterogeneity of the electric field (b–c). By analyzing the pulse curve shape it is possible to determine approximately where in the channel a particle was travelling (c). At ~1 MHz measurement frequency, impedance signal variations are mainly caused by the displaced conductive fluid (R_{sol}) rather than the cell membrane conductivity (C_m) or cytosol resistance (R_c), thus making the system suited for particle size measurements (d).

The in-phase signal from the impedance analyzer was used in combination with a high-pass filter (fc = 5 Hz), eliminating the DC component. The peaks and valleys of the signal (corresponding to a particle traversing the electrodes) were identified and used in the subsequent signal analysis. Amplitude, time of passage between electrodes (TOP), and velocity for all events were calculated. For further understanding the MIS was also simulated. The flow-velocity profile for the channel geometry was calculated in COMSOL using the geometries in the experimental channel. The impedance signal was simulated using COMSOL, by modelling a particle passing through the channel at different positions (Fig. 3). All boundaries except the electrodes were set to be insulators and the ends of the flow-channel were set to be periodic continuity boundaries. A 1 V signal was applied to the middle electrode and the outer electrodes were set to 0 V. The current density on each of the ground electrodes was integrated across the electrode area to give the total current and the current values were subtracted to give the differential current signal. This value was used as the impedance signal.

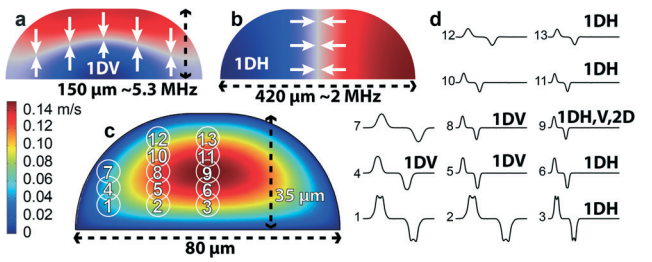

Fig. 3 Simulation results. COMSOL simulations of acoustic eigenmodes predicted the vertical and horizontal resonance modes at ~5.3 MHz and ~2.0 MHz respectively (a and b). Simulations of the impedance pulse shape show the effects of varying spatial particle positions in the channel cross section (c and d). Channel dimensions were 150 × 420 µm for the acoustic simulation and 80 × 35 µm for the impedance simulation.

Model particle suspensions and biofluids used in the experiments

Model particle samples consisted of polystyrene beads (Fluka, Sigma-Aldrich) suspended in saline (0.9% NaCl in Milli-Q water). A suspension containing 7 µm polystyrene (PS) beads was used for initial proof-of-principle experiments which included a set of runs in which different bead concentrations were analyzed in order to find optimal concentration conditions with respect to maximized throughput and minimized number of doublets. 7 µm PS beads were also used to evaluate system performance during runs with no ultrasound (0D), sidewall–sidewall standing wave ultrasound (1DH), top-bottom standing wave ultrasound (1DV) and simultaneous 1DH and 1DV ultrasound, resulting in two dimensional focusing (2D). A suspension with 3, 5 and 7 µm PS beads was used to evaluate the size measurement performance of the chip Coulter counter. Measurement performance on biofluid samples was evaluated by diluting whole blood 1 : 10 000 using normal saline spiked with 7 µm beads. Flow rate was set to 10 µl min^{-1} for the 7 µm bead samples and 5–7 µl min^{-1} for the bead mix and blood experiments, assuring laminar flows conditions. For comparison of the chip MIS operated in Coulter counter mode the suspensions were analyzed in a golden standard Coulter counter (Multisizer 3, Beckman Coulter).

Confocal imaging

For better understanding and confirmation of the acoustic focusing modes used to actuate the chip, *z*-mode confocal image reconstructions of the particle focusing were generated

(Fig. 5a–d). Green fluorescent 4.8 μm PS beads (Fluoro-Max G0500, Thermo Scientific) were run through the channel during 0D, 1DH, 1DV and 2D acoustophoretic actuation. For visualization of beads and channel boundaries fluorescent images were captured using a confocal microscope system (Fluoview 300 running on a BX51WI microscope, Olympus) with dual lasers (PS-Argon-Ion and PS-HeNe, Melles Griot).

Results and discussion

Simulation results of acoustic and impedance chip properties

The acoustic simulations showed that a 150 × 420 μm rounded wall geometry would allow 0D, 1DH, 1DV and 2D experiments to be carried out when actuating the chip at frequencies close to those previously examined (2 and 5 MHz) (Fig. 3a and b). The modeling predicted a vertical $\lambda/2$-resonance top to bottom of the channel at 5.3 MHz while the sidewall-sidewall, horizontally particle focusing standing wave, was predicted at 2.0 MHz. By simultaneous actuation of the channel using these two frequencies, a 2D focusing node in the center of the channel should form.

The impedance simulations were integral for understanding and analyzing experimental data. The results show that a particle travelling close to the electrodes (positions 1–3, Fig. 3d) induces a comparatively high amplitude signal with a double peak, while particles far away from the electrodes (positions 10–13) induce low single peak signals, analogous to the signal profiles reported by Morgan *et al.*[60] Estimating the particle size based on the peak height would in these cases result in particles to be interpreted as either too large or too small as compared to particles of the same size passing in other parts of the channel. Particles travelling in the slow flow rate domains (positions 1–3, 4, 7, 12, 13) display longer TOP compared to fast travelling particles in the center of the channel (6, 8–9, 11). By employing 2-dimensional acoustophoretic prefocusing, locating the particles in the center of the channel (position 9), the errors caused by spatial dependence of the particles during the impedance measurement are eliminated.

Initial suspension concentration experiments

The microchannel consisted of a 19 mm long prefocusing section in which particles could be simultaneously focused both laterally and vertically. When defining the design specification the cross section dimensions of the prefocusing channel were chosen according to the acoustic eigenmode simulations. The prefocusing channel was followed by a narrow aperture section (80 × 35 μm and 1.5 mm long) with electrodes patterned across the flat channel bottom to enable Coulter counter measurements (Fig. 4). The 2D-acoustic prefocusing confined the particles to a well-defined flow velocity vector in the channel center, as verified by experimental data showing a narrow velocity distribution and uniform impedance peak shapes, *i.e.* particles pass the electrode region in the same location of the channel cross section.[11,60]

The initial MIS experiments were carried out to determine the optimal particle concentrations for subsequent experiments. A low particle concentration results in high percentage of usable events (minimizing the risk for doublets – having multiple particles in the measurement zone simultaneously), but makes the analysis slow when counting large number of events. Conversely, a high particle concentration allows for rapid analysis but leads to an increase in number of unusable events. The concentration study showed that ~300 particles μl^{-1} is sufficient to achieve ≥90% usable events (Fig. 4c). Calculations of the probability of having multiple Poisson-distributed particles in a fluid volume equivalent to the measuring zone was carried out given varying concentrations and supported the experimental finds (Fig. 4c). At a concentration of 38 particles μl^{-1} the proportion of usable events was close to 99%. The subsequent experiments in this paper were performed at concentrations of 100–300 particles μl^{-1} since it allowed for a combination of relatively high usable event ratios and rapid analysis.

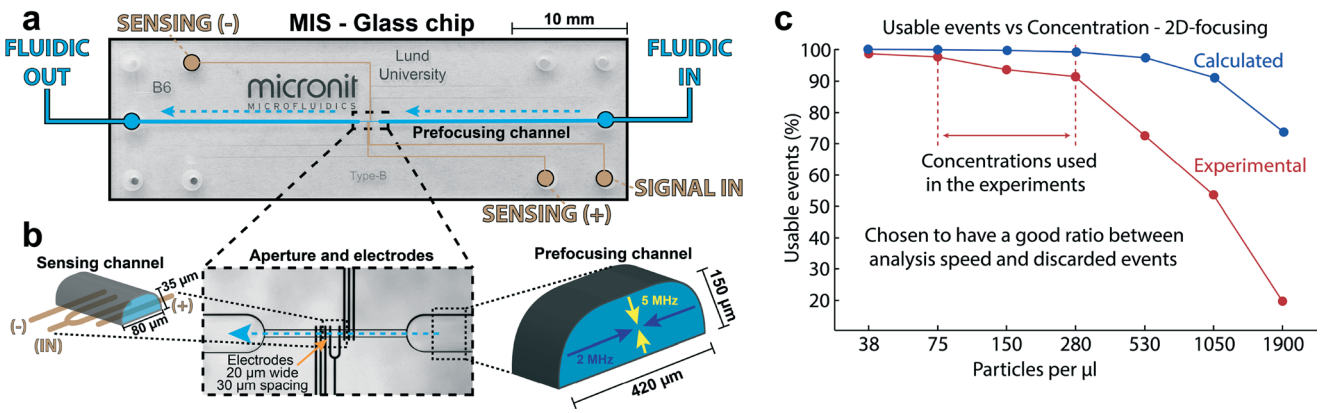

Fig. 4 Channel design and initial results. The 45 × 15 mm glass chip included a prefocusing channel (19 mm long) and a sensing channel (1.5 mm long) (a). The prefocusing channel (420 × 150 μm) was designed to focus particles in 2-dimensions (b-right). The sensing channel was 80 × 35 μm across which electrodes were patterned to perform measurements on cell-sized particles (1–20 μm in diameter) (b-left). Initial experiments and were carried out to determine optimal suspension concentrations and optimal concentrations were determined to be 100–300 particles μl^{-1}, also supported by calculating the probability of having two or more Poisson-distributed particles in the sensing channel simultaneously given varying suspension concentrations (c).

Impact of acoustophoretic prefocusing on MIS performance – no ultrasound

When a sample of 7 μm polystyrene particles was perfused through the channel without acoustophoretic prefocusing, particles were evenly distributed over the channel cross section. This distribution was also confirmed by confocal imaging (Fig. 5a) and resulted in large variations in pulse amplitudes and TOP data. A pulse amplitude *vs.* velocity (TOP-data) plot (*AV*-plot) illustrates the relationship between particle positions and the impedance signal they induced (Fig. 5i). The resulting *AV*-plot share the boomerang shape with the simulated data of 50 000 events (Fig. 5e), which was consistent throughout the experiments, with the fastest travelling beads at its vertex and with beads positioned either below or above the channel center visible along the boomerang sides. In accordance with simulations, beads that travel close to the electrodes have low velocities with high pulse amplitudes, thus positioned far from the vertex along the right side of the data distribution in the *AV*-plot while the equally slow travelling particles far from the electrodes at the channel top have lower pulse amplitudes and are visible in the left side of the data distribution of the *AV*-plot (Fig. 3d positions 3 and 13).

1-Dimensional horizontal focusing (sidewall–sidewall) – 1DH

When actuating the channel using the horizontal resonance, sidewall–sidewall, the confocal imaging confirmed that the beads were focused in a thin ribbon from top to bottom at the center of the channel (Fig. 5b), in agreement with the COMSOL simulations. In this case the peak amplitude (*V*) depends on the position in the vertical direction of the channel and the particle velocity measurement (TOP) in the laminar flow profile is reflected in the skewed parabolic shape of the measured data distribution (Fig. 5j). The deviation from a true parabolic shape is due to the fact that the vertical electrical field gradient is not linear. The same distribution is also seen in the corresponding COMSOL modelling (Fig. 5f).

1-Dimensional vertical focusing (top-bottom) – 1DV

Acoustic actuation of the channel with a top-bottom vertical standing wave focused particles into a curved horizontal sheet across the channel, as predicted from simulations and confirmed by confocal imaging (Fig. 5c). This is the first experimental verification of a curved shape of the ultrasonic $\lambda/2$ standing wave pressure nodal line in microfluidic channels with rounded side-walls. The curve phenomenon is an effect of the channel geometry which alters the resonance criteria close to the rounded walls. The combination of the curved particle sheet and the rounded wall geometry makes the *AV*-data points widely distributed under the parabolic shaped data boundary since it is not possible to directly translate a certain velocity to a point on either side of the vertical symmetry axis of the channel (contrary to the top-bottom regime of the straight 1DH particle ribbon) (Fig. 5g and k). The different shapes of the parabolic data boundaries between the simulated and experimental data is interpreted as being caused by slight deviations in the modelled

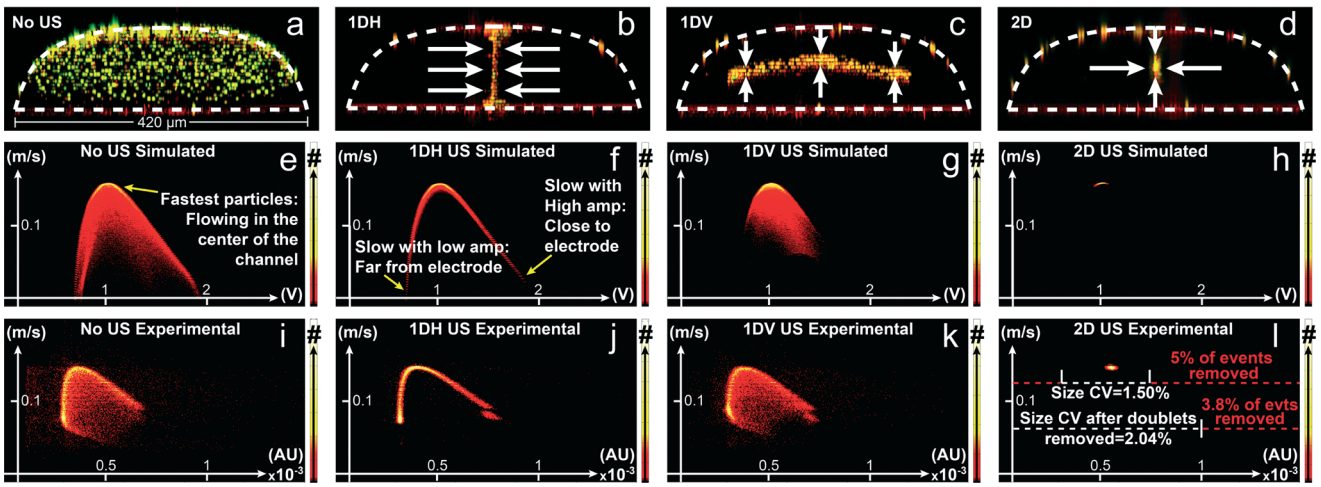

Fig. 5 Simulated (50×10^3 events) and experimental (30×10^3 events) MIS data for 7 μm beads during 0D (No US), 1DH, 1DV and 2D modes of operation as well as *z*-mode confocal imaging. In 0D mode beads are distributed across the channel cross section, with large variations in velocities and distance to the electrodes (a, e, i). In 1DH mode beads are aligned in a vertical ribbon (b) from top to bottom, yielding a parabolic-like shape (linked to the laminar flow profile) of the data distribution in the *AV*-plot (f, j). In 1DV mode beads are aligned in a curved sheet, where the curvature of the sheet results in a broad distribution of data points underneath the parabolic shaped delineation (c, g, k). In 2D focusing mode the beads are all focused in the center of the channel, travelling at the same velocity and distance from the electrodes, resulting in minimized variations in the data point distribution in the *AV*-plot, ideally only varying in amplitude due to size differences of the beads (d, h, l).For comparison to size sensitivity CV's in other systems two sets of thresholds were added, one removed pulses above 1.0×10^{-3} AU (doublets) and the other removed pulses outside the $0.25–0.75 \times 10^{-3}$ AU range (removing events outside the distinct event distribution at ~0.5×10^{-3} AU). The remaining 96.2 and 95.0% events had particle size CV's of 2.04 and 1.50% respectively.

electrical field gradient and the actual gradient in the microchannel.

2D ultrasound

When operating the system in the 2-dimensional acoustophoretic focusing mode the confocal imaging showed particles localized to the superimposed nodal point of the horizontal and vertical resonances (Fig. 5d). The impedance measurement data in the corresponding *AV*-plot were all confined to a point at the vertex of the parabolic distribution profile (Fig. 5l). All of the ~30 000 particles that were analyzed were clustered in the 2-D nodalpoint, agreeing well with the corresponding modelling data (Fig. 5h). For comparison with commercial instruments and previously presented systems using optical or impedance based cytometry a threshold was added (Fig. 5l) to remove doublets. The procedure removed 3.8% of the events, corresponding well with expected levels of unusable events (<10%) for the particle concentration interval used. The coefficient of variation (CV) for the remaining events (96.8%) was 2.04% (cube root of CV for pulse amplitudes). This value is on par or better than size CV's reported on similar size beads (6–7 μm) by other groups that use impedance or optically based cytometry in combination with either acoustic, inertial or electric forces to position particles. Reported CV's include 1.6% (inertial focusing of 6 μm particles combined with transverse electrode MIS)[60] and 1.8% (dielectric focusing of 6 μm particles combined with transverse electrode MIS)[18] for impedance size measurements and 2.56% (bulk acoustic wave focusing of 10 μm particles combined with fluorescent flow cytometer)[56] and 10.9% (surface acoustic wave focusing of 10 μm particles combined with fluorescent flow cytometer)[61] for fluorescence amplitude CV's. Groups often report CV's on events in a distinct amplitude distribution and the size CV of 2D focused particle events using this criterion was 1.50% with 95.0% events remaining (Fig. 5l), which is less than the stated CV (<2.0%) from the manufacturer (Sigma), measured using a Multisizer, the same golden standard commercial instrument that we benchmark our system against in the experiments described below. It should be noted that fluorescence cytometer measurements depend on particle size as well as fluorescent intensity which makes it difficult to compare particle focusing precision between the two using only amplitude CV's.[18,35,56]

Size discrimination

A mixture of 3, 5 and 7 μm PS beads passing through the channel was investigated. Derived data from experiments with no ultrasound indicated three partly overlapping populations and the corresponding amplitude and TOP measurements within each population also varied significantly (Fig. 6a–c). In contrast, with 2D acoustic focusing three distinct focal regions emerged in the *AV*-plot, (Fig. 6e) and the size histogram displayed fully separated size distributions (Fig. 6f). Particles were all travelling at similar velocities (Fig. 6d) and the different particle sizes induced pulse amplitudes corresponding to the three particle volumes. The samples were also analyzed using a Multisizer 3, showing comparable data to the MIS recorded data (Fig. 6h *vs.* b and f).

Blood spiked with 7 μm PS beads

A blood/bead suspension was run through the chip with 2D prefocusing either active or inactive until 20 000 events were recorded for each setting. Without prefocusing it was barely possible to differentiate between the bead and blood cell population (mainly erythrocytes), (Fig. 7a and b). However, when the prefocusing was activated the data showed a distinct difference between the two populations (Fig. 7e and f). The blood population showed slightly less conformity in amplitude data (size) while the velocities were consistently uniform for both populations. This is also reflected in the broader cell volume distribution in the RBC population as measured by the reference Coulter counter (Fig. 7h). Velocity histograms from the experiments with and without prefocusing show the significant improvement in velocity variations between prefocused and unfocused samples (Fig. 7c *vs.* d). The samples were also analyzed in a Multisizer 3 and the histograms

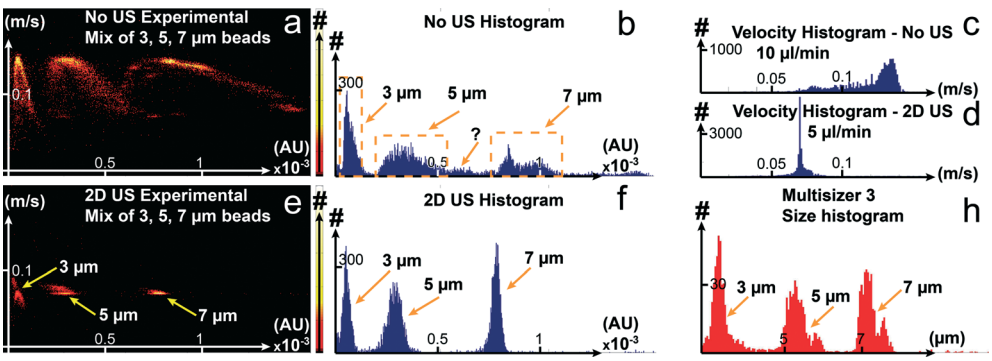

Fig. 6 *AV*-plots and histograms from 2D-prefocused and unfocused samples with a mixture of 3, 5, 7 μm PS beads (17×10^3 events). An *AV*-plot of the unfocused beads show data with wide distributions for each bead size (a) while the acoustically prefocused sample shows each population clearly focused in three distinct zones (e), also visible in the velocity histograms (c *vs.* d). The corresponding size histograms also demonstrates the importance of the 2D-prefocusing *cf.* (b) and (f) and the golden standard reference data obtained from the Multisizer 3 Coulter counter (h).

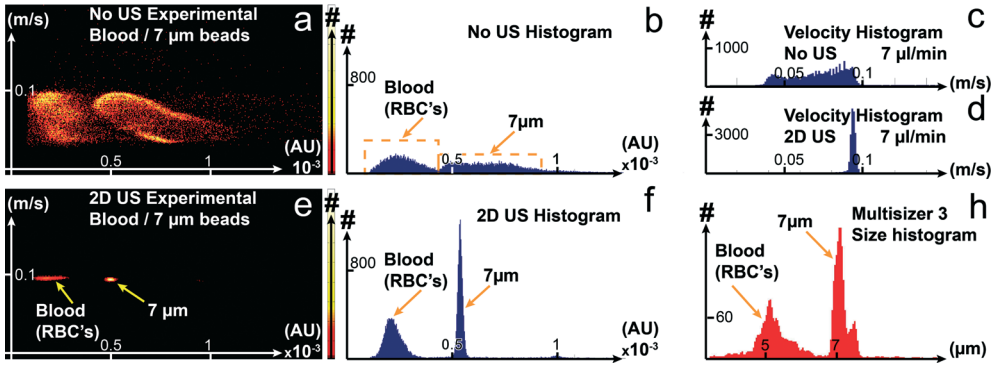

Fig. 7 Experimental data for a mixture of diluted whole blood and 7 μm beads. In the unfocused sample it is barely possible to distinguish two populations of particles with different sizes (volume difference between RBC's and 7 μm PS beads) and the histogram suggests that sizes overlap slightly (a and b). The difference in size between the RBC's and the PS beads become apparent with prefocusing activated (e and f). As seen with the pure bead samples the blood/bead mix also show significantly less variation in speed when they are focused (c, d). The prefocused blood/bead data (f) compares well with the benchtop Coulter counter (h).

were compared to histograms generated from the MIS experiments with prefocusing activated (Fig. 7f *vs.* h), showing good agreement with the golden standard instrument both in terms of particle size distribution and total number of particles in each population.

Conclusion

We have developed a microchip impedance spectroscopy (MIS) system with planar electrodes in a single sided configuration, which uses acoustophoretic prefocusing of cells and particles to circumvent the need for sheet flow alignment. Experimental results illustrate the importance of particle positioning in these systems, specifically in MIS systems that uses a planar electrode configuration. The MIS was able to analyze single and mixed size bead suspensions as well as diluted whole blood and data correlates well with golden standard Coulter counter measurements. The combination of acoustophoretic focusing and planar electrodes enables a simple route to fabricate chip integrated Coulter counters and impedance spectrometry systems by processing the microchannels in one glass layer and the measurement electrodes in a single lithography step on the covering glass slide. The design alleviates the need for elaborate channel designs with sheet flow functionality, intricate electrode configurations and more advanced flow control.

Acknowledgements

The authors would like to thank the following organizations and companies for their financial support: FOSS A/S, FORMAS Tvärlivs, VINNOVA IFFH CellCARE, Swedish Research Council (637-2013-444), Stiftelsen Olle Engkvist Byggmästare.

References

1 W. H. Coulter, Means for counting particles suspended in a fluid, *US Pat.*, 2656508, 1953.
2 A. Moldavan, *Science*, 1934, **80**, 188–189.
3 H. E. Kubitschek, *Nature*, 1958, **182**, 234–235.
4 C. F. T. Mattern, *J. Appl. Physiol.*, 1957, **10**, 56–70.
5 R. H. Berg, Peripherally locked and sealed orifice disk and method, *US Pat.*, 3266526, 1966.
6 W. R. Hogg, *US Pat.*, 3936739, 1976.
7 P. J. Crosland-Taylor, *Nature*, 1953, **171**, 37–38.
8 P. N. Dean, D. Pinkel and M. L. Mendelsohn, *Biophys. J.*, 1978, **23**, 7–13.
9 W. A. Bonner, H. R. Hulett, R. G. Sweet and L. A. Herzenberg, *Rev. Sci. Instrum.*, 1972, **43**, 404–409.
10 M. Koch, A. G. R. Evans and A. Brunnschweiler, *J. Micromech. Microeng.*, 1999, **9**, 159–161.
11 S. Gawad, L. Schild and P. H. Renaud, *Lab Chip*, 2001, **1**, 76–82.
12 D. Holmes and H. Morgan, *Anal. Chem.*, 2010, **82**, 1455–1461.
13 T. Sun and H. Morgan, *Microfluid. Nanofluid.*, 2010, **8**, 423–443.
14 L. I. Segerink, A. J. Sprenkels, J. G. Bomer, I. Vermes and A. van den Berg, *Lab Chip*, 2011, **11**, 1995–2001.
15 C. Bernabini, D. Holmes and H. Morgan, *Lab Chip*, 2011, **11**, 407–412.
16 K. C. Cheung, M. Di Berardino, G. Schade-Kampmann, M. Hebeisen, A. Pierzchalski, J. Bocsi, A. Mittag and A. Tárnok, *Cytometry, Part A*, 2010, 77, 648–666.
17 D. Barat, D. Spencer, G. Benazzi, M. C. Mowlem and H. Morgan, *Lab Chip*, 2012, **12**, 118–126.
18 G. Mernier, E. Duqi and P. Renaud, *Lab Chip*, 2012, **12**, 4344–4349.
19 M. Nasir, D. T. Price, L. C. Shriver-Lake and F. Ligler, *Lab Chip*, 2010, **10**, 2787–2795.
20 C. Bernabini, D. Holmes and H. Morgan, *Lab Chip*, 2011, **11**, 407–412.
21 M. Evander, A. J. Ricco, J. Morser, G. T. A. Kovacs, L. L. K. Leung and L. Giovangrandi, *Lab Chip*, 2013, **13**, 722–729.
22 T. M. Squires and S. R. Quake, *Rev. Mod. Phys.*, 2005, 77, 977–1026.

23 G. M. Whitesides, *Nature*, 2006, **442**, 368–373.
24 E. Verpoorte, *Lab Chip*, 2003, **3**, 42N–52N.
25 L. Y. Yeo, H.-C. Chang, P. P. Y. Chan and J. R. Friend, *Small*, 2011, **7**, 12–48.
26 D. A. Ateya, J. S. Erickson, P. B. Howell, L. R. Hilliard, J. P. Golden and F. S. Ligler, *Anal. Bioanal. Chem.*, 2008, **391**, 1485–1498.
27 A. Wolff, I. R. Perch-Nielsen, U. D. Larsen, P. Friis, G. Goranovic, C. R. Poulsen, J. P. Kutter and P. Telleman, *Lab Chip*, 2003, **3**, 22–27.
28 N. Demierre, T. Braschler, P. Linderholm, U. Seger, H. van Lintel and P. Renaud, *Lab Chip*, 2007, **7**, 355–365.
29 C. Simonnet and A. Groisman, *Appl. Phys. Lett.*, 2005, **87**, 114104.
30 N. Sundararajan, M. S. Pio, L. P. Lee and A. A. Berlin, *J. Microelectromech. Syst.*, 2004, **13**, 559–567.
31 D. P. Schrum, C. T. Culbertson, S. C. Jacobson and J. M. Ramsey, *Anal. Chem.*, 1999, **71**, 4173–4177.
32 D. Di Carlo, *Lab Chip*, 2009, **9**, 3038–3046.
33 G. Blankenstein and U. Darling Larsen, *Biosens. Bioelectron.*, 1998, **13**, 427–438.
34 A. Ashkin, *Phys. Rev. Lett.*, 1970, 24–27.
35 D. Spencer, G. Elliott and H. Morgan, *Lab Chip*, 2014, **14**, 3064–3073.
36 M. Shaker, L. Colella, F. Caselli, P. Bisegna and P. Renaud, *Lab Chip*, 2014, **14**, 2548–2555.
37 J. Voldman, *Annu. Rev. Biomed. Eng.*, 2006, **8**, 425–454.
38 R. Pethig, *Biomicrofluidics*, 2010, **4**, 022811.
39 J. J. Hawkes and W. T. Coakley, *Sens. Actuators, B*, 2001, **75**, 213–222.
40 A. Nilsson, F. Petersson, H. Jönsson and T. Laurell, *Lab Chip*, 2004, **4**, 131–135.
41 F. Petersson, A. Nilsson, C. Holm, H. Jonsson and T. Laurell, *Lab Chip*, 2005, **5**, 20–22.
42 J. Hultström, O. Manneberg, K. Dopf, H. M. Hertz, H. Brismar and M. Wiklund, *Ultrasound Med. Biol.*, 2007, **33**, 145–151.
43 M. A. Burguillos, C. Magnusson, M. Nordin, A. Lenshof, P. Augustsson, M. J. Hansson, E. Elmér, H. Lilja, P. Brundin, T. Laurell and T. Deierborg, *PLoS One*, 2013, **8**, e64233.
44 A. Kundt, *Philos. Mag.*, 1868, **35**, 41–48.
45 Lord Rayleigh, *Philos. Mag.*, 1902, **3**, 338–346.
46 L. V. King, *Proc. R. Soc. London, Ser. A*, 1934, **147**, 212–240.
47 L. P. Gorkov, *Sov. Phys. Dokl.*, 1962, **6**, 773–775.
48 R. Barnkob, P. Augustsson, T. Laurell and H. Bruus, *Lab Chip*, 2010, **10**, 563–570.
49 C. Grenvall, P. Augustsson, J. R. Folkenberg and T. Laurell, *Anal. Chem.*, 2009, **81**, 6195–6200.
50 M. E. Piyasena, P. P. Austin Suthanthiraraj, R. W. Applegate, A. M. Goumas, T. A. Woods, G. P. López and S. W. Graves, *Anal. Chem.*, 2012, **84**, 1831–1839.
51 O. Manneberg, S. Melker Hagsäter, J. Svennebring, H. M. Hertz, J. P. Kutter, H. Bruus and M. Wiklund, *Ultrasonics*, 2009, **49**, 112–119.
52 P. Augustsson, C. Magnusson, M. Nordin, H. Lilja and T. Laurell, Microfluidic, Label-Free Enrichment of Prostate Cancer Cells in Blood Based on Acoustophoresis, *Anal. Chem.*, 2012, **84**(18), 7954–7962, DOI: 10.1021/ac301723s.
53 M. Nordin and T. Laurell, *Lab Chip*, 2012, **12**, 4610–4616.
54 O. Jakobsson, C. Grenvall, M. Nordin, M. Evander and T. Laurell, *Lab Chip*, 2014, **14**, 1943–1950.
55 G. Goddard, J. C. Martin, S. W. Graves and G. Kaduchak, *Cytometry, Part A*, 2006, **69**, 66–74.
56 G. R. Goddard, C. K. Sanders, J. C. Martin, G. Kaduchak and S. W. Graves, *Anal. Chem.*, 2007, **79**, 8740–8746.
57 C. Grenvall, J. R. Folkenberg, P. Augustsson and T. Laurell, *Cytometry, Part A*, 2012, **81**, 1076–1083.
58 H. Bruus, *Lab Chip*, 2012, **12**, 1014–1021.
59 M. Evander, A. Lenshof, T. Laurell and J. Nilsson, *Anal. Chem.*, 2008, **80**, 5178–5185.
60 D. Spencer and H. Morgan, *Lab Chip*, 2011, **11**, 1234–1239.
61 Y. Chen, A. A. Nawaz, Y. Zhao, P.-H. Huang, J. P. McCoy, S. J. Levine, L. Wang and T. J. Huang, *Lab Chip*, 2014, **14**, 916–923.

Concurrent isolation of lymphocytes and granulocytes using improved free flow acoustophoresis with cell prefocusing and multiple target outlets

Carl Grenvall, Cecilia Magnusson, Hans Lilja and Thomas Laurell
Lund University

Abstract
This paper presents how microchip based free flow acoustophoresis in combination with two-dimensional cell pre-alignment enables concurrent multiple target outlet fractionation of leukocytes into subpopulations (lymphocytes, monocytes and granulocytes). Significantly increased accuracy in size based sorting of microbeads as compared to previously presented multiple outlet systems is also reported. Fluorescence microscopy illustrates the importance of two-dimensional prefocusing where a sample mixture of 3, 7 and 10 micrometer beads are separated into well confined particle streams and collected in their respective target outlets when prefocusing is active. With prefocusing inactive the particles are more dispersed displaying poor separation performance. Confocal image data was used as a means to verify the two-dimensional prefocusing of particles. Flow cytometry data show concurrent isolation of leukocyte subpopulations with high purity (95.2 ± 0.6% and 98.5 ± 0.7%) and recovery (86.5 ± 10.9% and 68.4 ± 10.6%) for lymphocytes and granulocytes in their corresponding outlets with a relatively low purity and high recovery of monocytes (25.2% ± 5.4% and 83.1 ± 4.3%) in the third target outlet with no subpopulation bias. These data demonstrate an unprecedented separation of leukocyte subpopulations at flow rates and cell concentrations previously not reported in acoustofluidic systems. Two-dimensional prefocusing free flow acoustophoresis with multiple target outlets is a viable alternative to current methods for particle sorting and cell isolation, requiring a minimum of sample preparation and lowering analysis time and cost.

Introduction
This paper presents a method to fractionate leukocytes or other complex particle- or biosuspensions into pure subpopulations by combining acoustophoresis with two-dimensional acoustic prefocusing in a chip with multiple target outlets. Recent years demonstrate an increased activity in the lab-on-a-chip (LOC) field of research aimed at integrating miniaturized analytical tools for biotechnical applications to decrease cost or allow handheld devices in point-of-care (POC) diagnostics [1–4] The development of rapid and precise low cost methods for fractionation and analysis of blood, which is of vital interest for clinics as well as researchers, is one of the areas that benefit from this technology. Among the possible applications for such improved methods is the purification of leukocytes into subpopulations that may be used to analyze interleukin signaling between different subpopulations during immune responses, and help to distinguish between virus and bacterial infections as well as detect leukemia [5–8]. Traditionally the preparation and fractionation of blood requires several steps of pipetting, centrifugation and labelling, all of which are time consuming, expensive and require trained personnel. The methods also risk introducing unwanted artifacts into the samples and may affect cell viability or phenotype profile [9–14]. Several groups have presented novel cell handling methods either based on preprocessed samples that are analyzed on chip, or chips that process samples for subsequent analysis off-chip [3,15–19]. However, much remain to be done, especially when it comes to strategies for handling small volumes and performing label free or simultaneous fractionation into multiple subpopulations. We propose to solve these challenges by using free flow acoustophoresis (FFA), which is an attractive alternative to other techniques since the separation is based on the intrinsic acoustic properties of particles or cells, and does not require any excessive pretreatment of the sample. Furthermore, FFA is a gentle method, able to handle a wide range of sample volumes with high throughput and can fractionate cells into several subpopulations simultaneously [20–24].

Free Flow Acoustophoresis

Petersson et al. [20] demonstrated continuous FFA size separation of particles mixtures in the range of 2-10 µm, as well as blood component fractionation. More recently, size dependent cell cycle analysis using acoustic sorting was also reported [25]. In FFA, the particle stream is normally laminated at the side wall of a flow channel that supports a $\lambda/2$ standing wave. The acoustic force then causes the particles to migrate to the standing wave pressure node in the channel center. The migration speed for individual particles is highly dependent on particle volume and will result in a lateral distribution of particles across the channel according to their size. The laminar flow regime in the channel then allows fractions of this distribution, each containing particles with similar sizes, to be extracted through different channel outlets.

A key limiting factor in conventional FFA separation systems, as well as in many other microchip separation or detection methods, is the initial spatial distribution of particles as they enter the separation channel[26–28]. The main reason for this is that the acoustic force field and the flow speed vary laterally and vertically across the channel. The variation causes particles to experience different amounts of acoustic force depending on their initial position in the channel, which in turn decreases separation precision. The acoustic profile directly affects the forces acting on the particles while the inherent parabolic flow profile of the microchannel will affect particle retention times in the channel, indirectly affecting the amount of acoustic force a particle is exposed to. Both phenomena lead to "field dispersion" in which particles with the same size will end up in different outlets due to varying initial positions in the channel. Even though clever channel design can alleviate some of the particle alignment problems, it often has drawbacks in terms of complex and expensive designs, decreased flow speeds, brittle structures, increased risk of clogging in small inlets [29,30].

In order to overcome the problems with sample dispersion and to facilitate an integration of FFA in lab-on-a-chip devices together with miniaturized analysis tools, this paper presents, for the first time a multiple (5) target outlet FFA chip with an integrated two-dimensional prefocusing zone. The method confines the particles to a distinct position in a prefocusing channel, yielding uniform flow velocities and acoustic exposure for the particles in the separation channel, without the aforementioned drawbacks of having to design intricate channel structures. Two-dimensional continuous flow focusing (2D) has previously been reported to improve performance in systems that are dependent on precise alignment of particles. These include single target outlet systems for acoustically activated cell sorting and circulating tumor cell extraction from blood as well as fluorescent and impedance based cytometers [31–35].

The presented multi outlet FFA system demonstrates an unprecedented performance in separating micro particles and leukocyte subpopulations with respect to purity, recovery and throughput. Confocal images confirm that the 2D-prefocusing method confines particles laterally as well as vertically before separation. Size sorting is performed and visualized using fluorescent polystyrene beads. Sorted monodisperse polystyrene beads of different sizes are counted in a golden standard Coulter counter to compare the system with earlier work. As final proof of concept a, benchtop flow cytometer is used to confirm successful isolation of sorted blood components (WBC fractionation).

Materials and Methods

Theory – Microfluidics

The laminar flow profile is an important concept to account for when designing microfluidic systems. A 150x150 µm square channel with water as suspension media, corresponding to the prefocusing channel presented here, allows for flow speeds in excess of 18 ml/min before turbulent flow occurs, which is several magnitudes higher than the ~0.01 ml/min flow rates used here. Once laminar flow is established it is also important to make sure that all particles flow in the same two dimensional position in the cross

section of the separation channel to minimise sample dispersion. Early FFA systems suffered from this problem which resulted in "peak broadening", i.e. particles with the same size ended up in different outlets. This was due to the fact that they were positioned away from each other when they entered the sorting channel, and thus experienced non-uniform acoustic field retention times; ending up laterally spread across channel even after "size sorting" and consequently left the channel through different outlets because of the laminar flow. By laminating the sample into a narrower stream before entering the separation section, sorting performance can be increased. Recent papers eliminate the need for elaborate pre-alignment fluidics and increase sample throughput by adding a 2D-acoustic pre-focusing zone prior to separation [31,32,36]. The chip presented here expands this method by combining 2D-prefocusing with a free-flow acoustophoresis channel with multiple outlets to allow concurrent cell fractionation into several subpopulations (Fig. 1).

Theory – Acoustic force

The use of acoustic standing wave forces in suspended particle manipulation has been well researched and in the past decade a significant effort has been put into the implementation of acoustic particle manipulation in microchip formats with integrated microfluidics [23,37,38]. Acoustophoresis utilize the primary acoustic radiation force F_{rad} (Eq. 1) to focus particles into predetermined locations, the acoustic nodes or antinodes, in microfluidic channels. Depending on their density and compressibility, in comparison to the suspending media, particles will travel towards either the nodes or antinodes. The determining factor for this translation is the acoustic contrast factor Φ (Eq. 2). Denser particles, like cells, tend to have a positive contrast factor in commonly used flow media including water, and focus into the acoustic pressure nodes. Less dense particles, like lipid vesicles, have a negative contrast factor and focus into the pressure antinodes. The primary acoustic radiation force scales linearly with an increased contrast factor, Φ, and the particle volume, a^3. Studies have shown that acoustophoresis along with other acoustic force based particle manipulation techniques in microfluidic systems are gentle to cells and may consequently be used for biofluid preconditioning with maintained cell viability [24,39–41].

$$F_{\mathrm{rad}} = 4\pi a^3 \Phi k_y E_{\mathrm{ac}} \sin(2k_y y) e_y \quad \text{(2) Primary acoustic radiation force}$$

where

$$\Phi = \frac{\kappa_{\mathrm{o}} - \kappa_{\mathrm{p}}}{3\kappa_{\mathrm{o}}} + \frac{\rho_{\mathrm{p}} - \rho_o}{2\rho_{\mathrm{p}} + \rho_o} \quad \text{(3) Acoustic contrast factor}$$

and a (≈ 10 µm) is the particle radius, Φ is the acoustic contrast factor, $k_y = 2\pi / \lambda$ is the wave vector, E_{ac} (≈ 100 J/m^3) is the acoustic energy density, y is the distance from the wall, κ_{p} (≈ 2.5 × 10^{-10} Pa^{-1}) is the isothermal compressibility of the particle, κ_{o} (≈ 5 × 10^{-10} Pa^{-1}) is the isothermal compressibility of the fluid, ρ_{p} (≈ 1030 kg/m^3) is the density of the particle (cell) and ρ_{o} (≈ 1000 kg/m^3) is the density of the fluid.

The FFA chip presented in this work translates particles towards the center node. Since F_{rad} scales linearly with volume, even small differences in particle radius will result in large variations in the magnitude of the acoustic force which they are subject to. These varying force magnitudes move the particles towards the center node with varying velocities with the result that they end up in different positions along the channel cross section, which allow them to flow into different target outlets according to the laminar flow regime (Fig. 1).

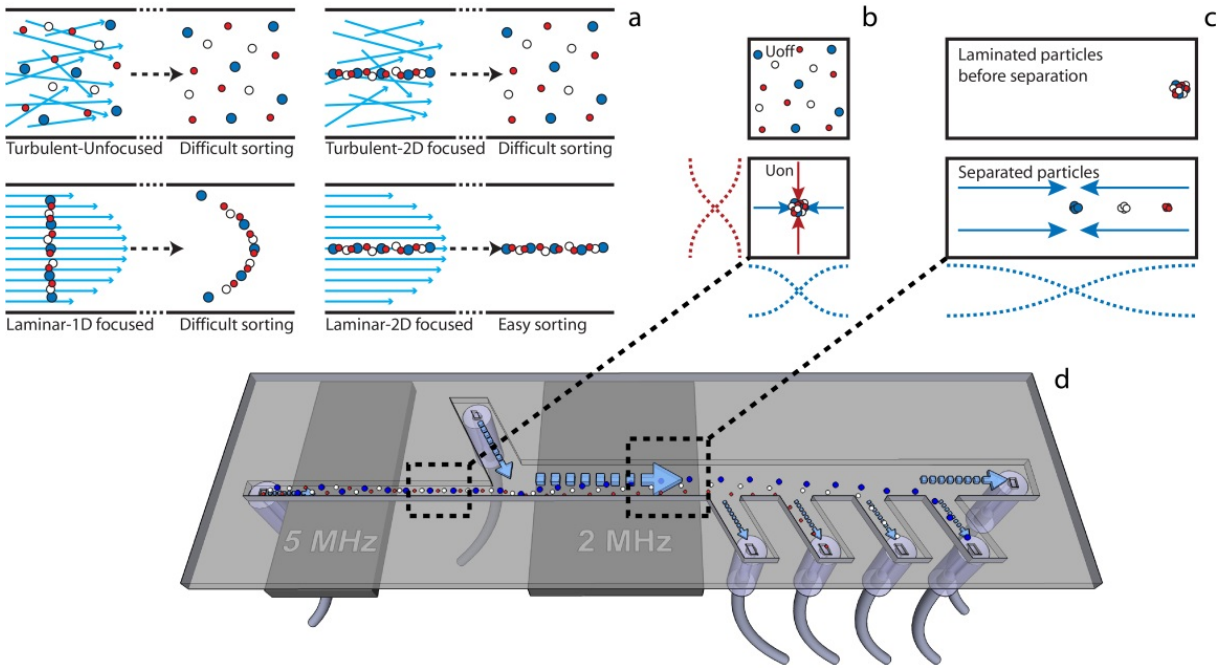

Fig 1, Microfluidic and acoustic theory schematic explaining 2D-prefocused FFA.A laminar system with prefocused particles is needed to perform precise sorting since particle retention times in the acoustic field will vary otherwise (a). By inducing standing waves in both directions of a square channel it is possible to prefocus particles prior to sorting (b, side view of the channel). The prefocused particles will encounter uniform initial acoustic forces and be translated towards the center pressure node according to their size and acoustic contrast factor(c).The separated particles then exit the sorting section of the chip (d, middle section) and are sorted into different target outlets according to their cross sectional position in the laminar flow profile (d, rightmost section of chip).

Chip design and fabrication

The microfluidic channel was designed to allow acoustic prefocusing and FFA separation at 5 and 2 MHz standing wave ultrasound respectively. The wet etching and glass bonding methods used to produce the microfluidic chip has previously been described [41]. However, in this work [110] silicon was used in order to achieve the aspect ratio needed for the prefocusing channel (1:1 etching ratio compared to the normal 1:2 ratio when using [100] silicon).

Acoustic setup

The standing ultrasonic waves were induced using piezoceramic transducers. A 0.4 mm thick transducer (PZ26, Ferroperm), attached underneath the 150x150 µm channel section with glue (Super Glue, Loctite) and actuated with a 4.82 MHz, ~5 V signal, was used for 2D-prefocusing. A 1 mm thick transducer, attached underneath the 375x150 µm channel section and actuated with a 1.93 MHz, ~19 V signal, was used for 1D lateral separation (Fig. 2). Each transducer was actuated using continuous sine wave signals from a signal generator (AFG 3022B, Tektronix) that were amplified using in-house assembled amplifiers (LT1012, Linear Technology). Chip temperature was controlled at ~33C^{o} using a Peltier cooling system (Peltier-Controller TC0806, CoolTronic), attached to the back-side of the piezoceramic transducers in order to maintain optimal acoustic actuation conditions regardless of ambient temperature and possible heating by thermal conduction from the transducers. Temperature readings for the cooling system were performed by a Pt1000 element attached to the 2 MHz transducer. A thermal compound (NT-H1, Noctua) was used to improve thermal conductivity between the transducers and the Peltier element.

Microfluidic setup

Fluidic access to the chip was enabled using silicon tubing as previously described [20]. The fluidic network, Teflon tubing with 0.3 mm inner diameter (TFE 58697-U, Supelco), connected the 1 ml sample syringe (Gastight 1001, Hamilton) and the 5 ml sheath fluid syringe (Gastight 1005, Hamilton) to the channel inlets and the four first channel outlets to four separate 1 ml collection syringes (BD Plastipak, Becton Dickinson) while the fifth outlet flowed into an open container. Six microfluidic pumps (Nemesys), each individually operated using a computer, was used to maintain stable flows. During cell experiments sample inlet flow was set to 8 µl/min while sheath inlet flow was set to 60 µl/min, resulting in a 1:10 ratio which helps to laminate the prefocused cells close to the channel wall in order to allow for maximum separation distance between original lateral particle position and the acoustic node in the middle of the channel. Sorting outlets flows were set to 12, 9 5 and 7 µl/min respectively in the first four outlets, leaving 35 µl/min flowing into the last outlet. For polystyrene bead experiments a seventh pump was connected to the last outlet. Inlet flows in these experiments were 10 and 120 µl/min for sample and sheath flow respectively, while each of the first four target outlets was set to a flow of 15 µl/min and the fifth to 70 µl/min. These settings split the half of the channel containing the particles into five equally large fractions which can be analyzed individually. A schematic of the complete system can be seen in fig 2.

Confocal microscopy setup

In order to evaluate the 2D focusing the acoustophoresis channel was perfused with a suspension of 4.8 µm green fluorescent polystyrene beads (Fluoro-Max G0500, Thermo Scientific) in MQ-water and observed using a confocal microscope system (Fluoview 300 running on a BX51WI microscope, Olympus). A combination of two lasers (PS-Argon-Ion and PS-HeNe, Melles Griot) was used to show bead positions and channel geometry simultaneously. Images was constructed from a 25-step 250 µm total scan in the z-direction and captured with the acoustic prefocusing turned off, operating at half amplitude (2 V) and at optimal amplitude (4 V) for subsequent size sorting. The same microscope, using a wide-spectrum mercury-vapor lamp instead of lasers, was used for capturing images of sorting performance with 2D-prefocusing on and off (Fig. 3).

Polystyrene bead separation

A mixture of polystyrene beads (Fluka, Sigma-Aldrich) suspended in water was used as a model system for initial experiments to evaluate channel performance. The bead mix contained beads of three different sizes, 3 (colored red), 7 (white) and 10 (blue) µm respectively, chosen to allow for reasonably large variations in the resulting acoustic forces while staying close to the cell size regime that were expected to be analyzed in the chip. The concentration was 0.15% by volume for the 3 µm beads and 0.65% and 0.6% respectively for the 7 and 10 µm beads. MQ-water was used as suspending media with 0.01% detergent (Tween 20, Bio-Rad) added to the suspension. Samples from each of the five target outlets were then analyzed using a Coulter counter (Multisizer 3, Beckman Coulter).

Blood component separation

In order to evaluate the system on a biological sample with clinical implications a population of white blood cells (WBC) was separated in the chip. The WBC subpopulations range from ~8 µm in diameter (small lymphocytes, T-cells) to ~11 µm (smaller granulocytes like neutrophils and eosinophils) and even ~14 µm and above for the largest subpopulations (large lymphocytes, monocytes and larger granulocytes like basophils and macrophages). Experiments were aimed at isolating pure populations of lymphocytes in outlet 2 and granulocytes in outlet 4 simultaneously, with maximum recovery while also recovering most of the monocytes in outlet 3. Outlet 1 and 5 was used as waste/buffer outlets.

Cells were prepared as follows: Blood was acquired from healthy donors at Skåne University Hospital, Lund, Sweden. The red blood cells were lysed by isotonic lysis (BD FACS™ Lysing Solution). The

WBCs were fixed by 2% paraformaldehyde for 10 minutes on ice and stained with 4 different antibodies: CD45-APC, CD3-PE, CD14-PE-Cy7 and CD66b-FITC (BD biosciences), for 20 minutes at room temperature. The WBCs were diluted 1:5 in a FACS buffer (1xPBS, 1% fetal bovine serum and 2 mM EDTA) before the acoustic separation. Outlet samples were collected in loops and analyzed using a FACS Canto II, (BD biosciences).

FACS analysis procedure: Sixty µl of each outlet fraction was analyzed by flow cytometry. The different WBCs were characterized as follows; Lymphocytes (T-cells) $CD45^+$ $CD3^+$ $CD14^-$ and $CD66b^-$, Monocytes $CD45^+$ $CD3^-$ $CD14^+$ and $CD66b^-$, and Granulocytes $CD45^+$ $CD3^-$ $CD14^+$ and $CD66b^+$.

Results and Discussion

Simulations and finished chip

Simulations indicated that 4.98 MHz acoustic actuation of a 150 x 150 µm quadratic channel would result in 2D prefocusing (Fig. 2a). Corresponding simulations in a 375 x 150 µm quadratic channel showed that 1.99 MHz acoustic actuation would allow FFA sorting (Fig. 2c). As shown in figure 2a the 2D-mode is really a superposition of two eigenmodes (vertical and lateral) at 4.98 MHz, which combine to focus particles in the center of the channel cross section. The finished chip with glued transducers and fluidic access tubing was placed on an aluminium heat sink to allow cooling with a Peltier element that was placed next to the chip on the heatsink. Temperature readings for the Peltier system were acquired using a Pt1000 sensor attached to the 2 MHz transducer. Initial focusing experiments in the finished chip resulted in acoustic focusing at 4.82 and 1.93 MHz respectively in the prefocusing and sorting channels (Fig. 2b).

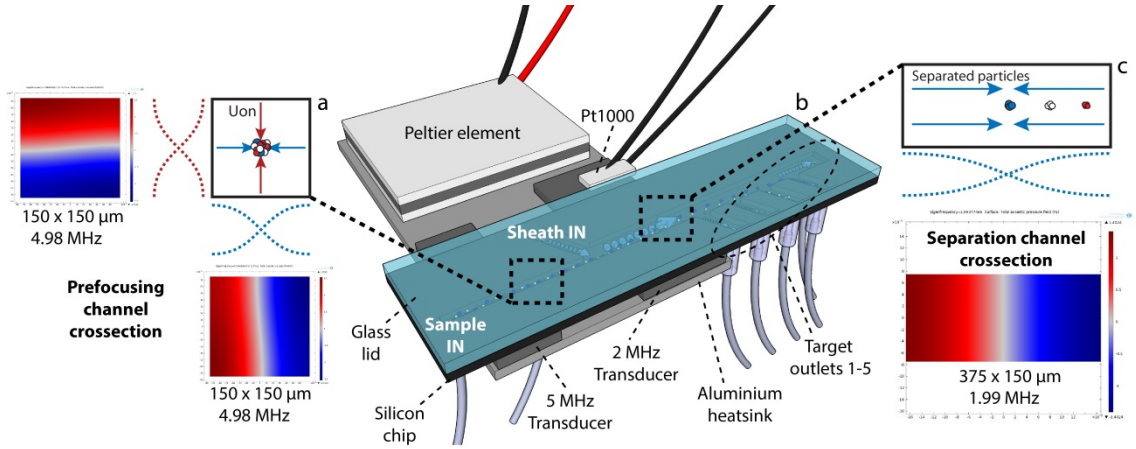

Fig 2, Schematic of the finished chip and results of acoustic simulations. Acoustic resonance in the prefocusing channel was indicated at 4.98 MHZ according to simulations but the finished chip focused particles in two dimensions at 4.82 MHz actuation, suggesting a slight mismatch between models and the finished channel, possibly due to "over etching" (a). These findings were consistent with results in the separation channel which focused particles at 1.93 MHz rather than the simulated 1.99(c).The finished chip had transducers and fluidic access glued to it and was then placed on an aluminium heatsink which was actively cooled with a Peltier system in order to maintain optimal acoustic temperature conditions(b).

2D prefocusing

Experiments with fluorescent polystyrene beads were performed to verify successful 2D-prefocusing using confocal microscopy. With the acoustic focusing inactive, beads were spread out across the channel cross section (Fig. 3a). However, with the acoustic actuation set to 2 V the beads started to focus into the center of the channel and at 4 V they were confined to a narrow center section less than 15 µm in diameter (microscope focal depth limitations prevented more detailed measurements), confirming

successful 2D-prefocusing (Fig. 3b and c). Once it was established that particles could be prefocused, the channel was infused with a mix of 3, 7 and 10 µm beads to investigate lateral dispersion in the separation channel with prefocusing active and inactive. Top view images of the channel with 2D-prefocusing active confirmed that particle positions varied less than 10µm laterally when entering the separation channel (Fig. 3d and e). When 2D focusing was active three bands, corresponding to the three bead size populations, were clearly visible in the separation channel while particles were more dispersed and not as precisely separated when 2D was inactive (Fig. 3f and g). It was possible to distinguish one bead population being separated into each target outlet with 2D active (Fig. 3h-j). With 2D inactive it was hard to distinguish any clear separation between subpopulations when going into the target outlets which illustrates why normal FFA does not produce as good results as 2D FFA (Fig 3k-m).

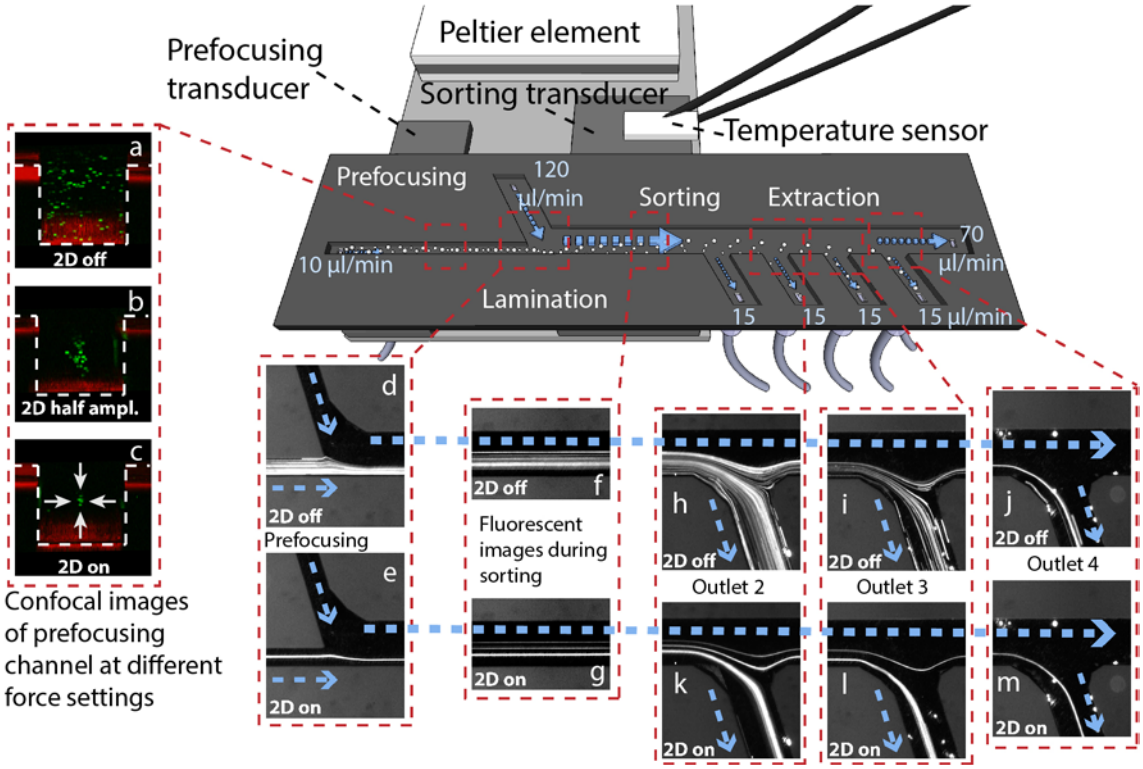

Fig 3, Confocal and normal microscope images of 2D-prefocusing and separation of polystyrene beads. With 2D-prefocusing activated it was possible to position particles in a very well defined area of the channel cross section using 4.82 MHz ultrasound (c vs. a and b). The particles were then laminated along the side of the separation channel (e and d). By using 1.93 MHz ultrasound, the prefocused beads were then separated into three very well defined streamlines in the separation channel while the unfocused beads were more dispersed (g vs. f). The particles were then sorted into different target outlets according to their positions in the flow profile, prefocused beads going into distinct outlets according to size while unfocused beads were spread out across the outlets (k-m vs. h-j).

Separation efficiency – Beads

Results from separations of suspensions with 3, 7 and 10 µm size polystyrene beads showed that modest size based separation was possible when 2D-prefocusing was inactive but improved significant when prefocusing was activated. 3 µm beads were targeted to outlet 2 and results were that 13.7, **55.9**, 23.5, 6.3, and 0.7% of those beads went into outlets 1-5 respectively. 7 µm beads were targeted to outlet 3 and

results were that 1.4, 3.3, **91.4**, 3.7, and 0.2% of those beads were collected in outlets 1-5 respectively. 10 µm beads were targeted to outlet 4 and results were that 1.5, 1.0, 5.6, **91.7**, and 0.2% of those beads were collected in outlets 1-5 respectively (Fig. 4a). These values correspond well with previous findings using similar non-prefocused systems [20]. When prefocusing was active there was a significant improvement in separation efficiency. 2D-prefocused 3 µm beads were again targeted to outlet 2 and results were that 3.8, **87.5**, 4.8, 3.6, and 0.3% of those beads were collected in outlets 1-5 respectively. 7 µm beads were targeted to outlet 3 and results were that 0.6, 1.0, **96.2**, 2.1, and 0.1% of those beads were collected in 1-5 respectively. 10 µm beads were targeted to outlet 4 and results were that 0.4, 0.2, 0.9, **98.5**, and 0.0% of those beads were collected in outlets 1-5 respectively (Fig. 4b). These results indicate that separation of particles in the chip becomes easier as size increases. Contributing factors might be that acoustic forces will decrease with decreased particle size (volume) according to theory, resulting in less efficient prefocusing on the 3 µm beads compared to the 7 or 10 µm beads, which them leads to less precise separation as well. Separation data as well as images for the larger beads suggest that it is not the acoustics that limit the separation efficiency at this point but rather the small flow instabilities, the rare occurrence of gas bubbles in the channel, possible sample carry over and residue in the fluidic system. All these parameters will impact system performance notably as separation efficiency goes above 95%, as in the case for 7 and 10 µm beads.

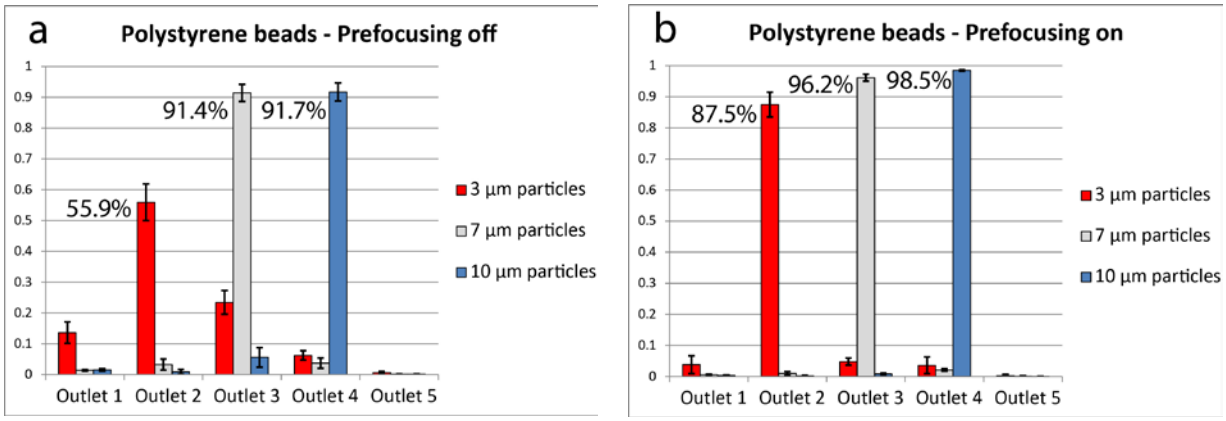

Fig 4, Separation efficiency of polystyrene beads with and without prefocusing. The unfocused beads were more dispersed as they entered the separation channel, which prevented precise separation (a). However, when prefocusing was activated the beads was possible to sort with high purity (b). Notably, the prefocusing also allowed very high sorting purities of 3 µm beads, not feasible in previously presented systems.

Separation efficiency – Leukocytes

Analogous to the polystyrene bead experiments, experiments on cells also showed large improvements in separation efficiency for the prefocused system as compared to experiments with prefocusing inactive. Leukocyte subpopulations overlap in size as well as density due to different nucleus composition which make them hard to separate using acoustic forces but 2D-prefocusing combined with multiple outlets should improve performance sufficiently to facilitate analysis of clinical samples, for example to analyze extremely large cells from each subpopulation or to "wash" samples in order to concentrate some chosen subpopulation. With this in mind the cell data is presented as purity and recovery rates instead of fractions in each outlet as in the case of the polystyrene beads. The number of cells in the diluted fraction in outlet 5 during the 2D-prefocused experiments was so low that the concentration fell below the FACS instrumentation analysis threshold (<72 gated events in 30 seconds). Thus data were reported only for outlets 1-4. Sample concentrations throughout these runs were measured at ~1M cells/ml using the same flow cytometer that was used for sorted cell analysis. Sample and sheath inlet flows were set to 8 and 60

µl/min respectively. The outlet flows for target outlets 1-4 were set to 12, 9 5 and 7 µl/min respectively, leaving the 5th waste outlet to free flow at 35 µl/min.

For the experiments without prefocusing the lymphocytes were targeted to outlet 2 and the result was a fraction with 56.5% (S.D. 15.0%) purity and 51.0% (S.D. 7.3%) recovery (number of lymphocytes going into target outlet compared to total number of lymphocytes going into outlets 1-4). The Monocyte fraction was targeted to outlet 3 and had a 12.1% (S.D. 4.0%) purity and recovery rate of 40.9% (S.D. 15.9%). Granulocytes were targeted to outlet 4 with a purity of 86.0% (S.D. 4.5%) and a recovery rate of 47.5% (S.D. 16.7%). These values are rather low and suggest that leukocyte fractionation is hard when using conventional FFA without prefocusing (Fig. 5a).

With prefocusing activated the lymphocytes were again targeted to outlet 2 and the result was a clean fraction with 95.1% (S.D. 0.6%) purity and 86.5% (S.D. 10.9%) recovery. The Monocyte fraction targeted to outlet 3 had a 25.2% (S.D. 5.4%) purity and recovery rate of 83.1% (S.D. 4.3%), again better than the non-prefocused sample. Granulocytes were collected in outlet 4 with a very high purity of 98.5% (S.D. 0.7%) and a recovery rate of 68.4% (S.D. 10.6%) ,which again show the benefits of prefocusing. Notably, the lymphocyte/granulocyte ratio was 57:1 in outlet 2 and 1:158 in outlet 4 (Fig. 5b). This huge difference in subpopulation ratios is only possible by introducing multiple outlets that allow some outlets to act as buffer outlets where the cells that overlap in acoustic properties are allowed to flow out. A 90% recovery with 25% purity for the monocytes would also not be possible without multiple outlets combined with 2D-prefocusing which allows extraction of this “center” fraction of the sample. All outlet fractions were also collected to compare subpopulation ratios in the original sample to the fractionated cells. The data show that the prefocused separation does not change the subpopulation ratios while the non-prefocused samples have a higher ratio of lymphocytes, most probably due to lost monocytes and granulocytes in the fifth waste outlet (Fig. 5c).

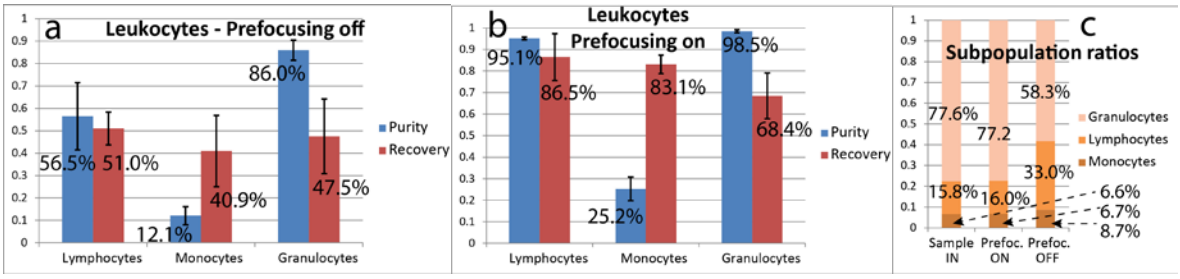

Fig 5, Fractionation efficiency of leukocytes into subpopulations of lymphocytes, monocytes and granulocytes. The unfocused samples were not possible to sort with high purities even with multiple outlets due to their overlapping sizes(a). However, when prefocusing was activated it was possible to fractionate the leukocytes into subpopulations with high purity with the help of the novel additional buffer outlets on the chip (b). It should be noted that the monocyte purity is lowered by lymphocytes and granulocytes spilling over into that outlet. A comparison between ratios of subpopulations in sorted samples their respective original samples showed that the prefocused acoustophoretic sorting of leukocytes does not alter inter-subpopulations ratios, while unfocused samples are altered in ratio, most probably due to granulocytes spilling over into the “waste” outlet. (c).

Conclusion

The results show that the acoustofluidic FFA system with prefocusing is able to simultaneously fractionate leukocytes into subpopulations with high purity (95-99% for lymphocytes and granulocytes) and recovery (>90% for lymphocytes and monocytes). The system also sorts different sized particles into multiple outlets with increased accuracy compared to previously presented systems. Images from experiments where prefocusing is switched on and off illustrated well confined particle streams going into

target outlets with prefocusing active and more dispersed particles with prefocusing inactive. These images in combination with confocal image data also confirmed that particles could be 2D focused prior to entering the separation channel. Future research will be aimed at integrating the method onto a Lab-On-a-Chip device with label-free sample preparation and downstream sample analysis. These findings show the potential of microchip acoustophoresis in clinical applications to purify or sort cells or beads with a minimum of sample preparation, thus minimizing the risk of introducing artifacts as well as lowering the cost and time consumed for each sample.

References

1. G. M. Whitesides, *Nature*, 2006, **442**, 368–73.

2. D. Mark, S. Haeberle, G. Roth, F. von Stetten, and R. Zengerle, *Chem. Soc. Rev.*, 2010, **39**, 1153–82.

3. L. Y. Yeo, H.-C. Chang, P. P. Y. Chan, and J. R. Friend, *Small*, 2011, **7**, 12–48.

4. V. Gubala, L. F. Harris, A. J. Ricco, M. X. Tan, and D. E. Williams, *Anal. Chem.*, 2012, **84**, 487–515.

5. B. R. Manetti, P. Parronchi, M. G. Giudizi, M. Piccinni, E. Maggi, G. Trinchieri, and P. Sergio, 1993, **177**.

6. P. C. Heinrich, I. Behrmann, S. Haan, H. M. Hermanns, G. Müller-Newen, and F. Schaper, *Biochem. J.*, 2003, **374**, 1–20.

7. L. Zhou, R. Somasundaram, R. F. Nederhof, G. Dijkstra, K. N. Faber, M. P. Peppelenbosch, and G. M. Fuhler, *Clin. Vaccine Immunol.*, 2012, **19**, 1065–74.

8. a van de Stolpe and P. T. van der Saag, *J. Mol. Med. (Berl).*, 1996, **74**, 13–33.

9. U. Dharmasiri, M. a Witek, A. a Adams, and S. a Soper, *Annu. Rev. Anal. Chem. (Palo Alto. Calif).*, 2010, **3**, 409–31.

10. Z. T. F. Yu, K. M. Aw Yong, and J. Fu, *Small*, 2014, **10**, 1687–703.

11. S. Nagrath, L. V Sequist, S. Maheswaran, D. W. Bell, D. Irimia, L. Ulkus, M. R. Smith, E. L. Kwak, S. Digumarthy, A. Muzikansky, P. Ryan, U. J. Balis, R. G. Tompkins, D. a Haber, and M. Toner, *Nature*, 2007, **450**, 1235–9.

12. A. Bøyum, *Scand. J. Immunol.*, 1976, **Suppl 5**, 9–15.

13. S. Fukuda and G. W. Schmid-scho, *J. Leukoc. Biol.*, 2002, **72**, 133–139.

14. D. Stibenz and C. Bührer, *Scand. J. Immunol.*, 1994, **39**, 59–63.

15. J. Yang, Y. Huang, X. B. Wang, F. F. Becker, and P. R. Gascoyne, *Biophys. J.*, 2000, **78**, 2680–9.

16. J. Voldman, *Annu. Rev. Biomed. Eng.*, 2006, **8**, 425–54.

17. N. Pamme and A. Manz, *Anal. Chem.*, 2004, **76**, 7250–6.

18. C. G. Hebert, A. Terray, and S. J. Hart, *Anal. Chem.*, 2011, **83**, 5666–72.

19. F. Petersson, A. Nilsson, C. Holm, H. Jonsson, and T. Laurell, *Lab Chip*, 2005, **5**, 20–2.

20. F. Petersson, L. Aberg, A.-M. Swärd-Nilsson, and T. Laurell, *Anal. Chem.*, 2007, **79**, 5117–23.

21. C. Grenvall, J. R. Folkenberg, P. Augustsson, and T. Laurell, *Cytom. Part A J. Int. Soc. Anal. Cytol.*, 2012, **81**, 1076–83.

22. M. E. Piyasena, P. P. Austin Suthanthiraraj, R. W. Applegate, A. M. Goumas, T. a Woods, G. P. López, and S. W. Graves, *Anal. Chem.*, 2012, **84**, 1831–9.

23. J. J. Hawkes and W. T. Coakley, *Sensors Actuators B Chem.*, 2001, **75**, 213–222.

24. J. Hultström, O. Manneberg, K. Dopf, H. M. Hertz, H. Brismar, and M. Wiklund, *Ultrasound Med. Biol.*, 2007, **33**, 145–51.

25. P. Thévoz, J. D. Adams, H. Shea, H. Bruus, and H. T. Soh, *Anal. Chem.*, 2010, **82**, 3094–8.

26. P. M. Goodwin, W. P. Ambrose, J. C. Martin, and R. a Keller, *Cytometry*, 1995, **21**, 133–44.

27. D. Spencer and H. Morgan, *Lab Chip*, 2011, **11**, 1234–9.

28. T. M. Squires and S. R. Quake, *Rev. Mod. Phys.*, 2005, **77**.

29. R. Yang, D. L. Feeback, and W. Wang, *Sensors Actuators A Phys.*, 2005, **118**, 259–267.

30. A. Wolff, I. R. Perch-Nielsen, U. D. Larsen, P. Friis, G. Goranovic, C. R. Poulsen, J. P. Kutter, and P. Telleman, *Lab Chip*, 2003, **3**, 22–7.

31. O. Jakobsson, C. Grenvall, M. Nordin, M. Evander, and T. Laurell, *Lab Chip*, 2014, **14**, 1943–50.

32. P. Augustsson, C. Magnusson, M. Nordin, H. Lilja, and T. Laurell, *Anal. Chem.*, 2012, **84**, 7954–62.

33. G. R. Goddard, C. K. Sanders, J. C. Martin, G. Kaduchak, and S. W. Graves, *Anal. Chem.*, 2007, **79**, 8740–6.

34. Y. Chen, A. A. Nawaz, Y. Zhao, P.-H. Huang, J. P. McCoy, S. J. Levine, L. Wang, and T. J. Huang, *Lab Chip*, 2014, **14**, 916–23.

35. C. Grenvall, C. Antfolk, C. Zoffmann Bisgaard, and T. Laurell, *Lab Chip*, 2014.

36. C. Grenvall, M. Carlsson, P. Augustsson, F. Petersson, and T. Laurell, in *Eleventh International Conference on Miniaturized Systems for Chemistry and Life Sciences*, 2007, vol. 2, pp. 1813–1815.

37. A. Nilsson, F. Petersson, H. Jönsson, and T. Laurell, *Lab Chip*, 2004, **4**, 131–5.

38. R. Barnkob, P. Augustsson, T. Laurell, and H. Bruus, *Lab Chip*, 2010, **10**, 563–70.

39. M. a Burguillos, C. Magnusson, M. Nordin, A. Lenshof, P. Augustsson, M. J. Hansson, E. Elmér, H. Lilja, P. Brundin, T. Laurell, and T. Deierborg, *PLoS One*, 2013, **8**, e64233.

40. J. Dykes, A. Lenshof, I.-B. Åstrand-Grundström, T. Laurell, and S. Scheding, *PLoS One*, 2011, **6**, e23074.

41. C. Grenvall, P. Augustsson, J. R. Folkenberg, and T. Laurell, *Anal. Chem.*, 2009, **81**, 6195–6200.